1-1-2011

Optoacoustic imaging of gold nanorod based photothermal therapy

Mehrnaz Tabibi
Ryerson University

OPTOACOUSTIC IMAGING OF GOLD NANOROD BASED PHOTOTHERMAL THERAPY

By

Mehrnaz Tabibi

B.Sc. Amir-Kabir University of Technology

(Tehran Polytechnic) 1993

Tehran, Iran

A thesis

presented to Ryerson University

in partial fulfillment of the

requirements for the degree of

Master of Science

in the Program of

Biomedical Physics

Toronto, Ontario, Canada, 2011

Author's Declaration

I hereby declare that I am the sole author of this thesis.

I authorize Ryerson University to lend this thesis to other institutions or individuals for the purpose of scholarly research.

_____

Mehrnaz Tabibi

I further authorize Ryerson University to reproduce this thesis by photocopying or by other means, in total or in part, at the request of other institutions or individuals for the purpose of scholarly research.

_____

Mehrnaz Tabibi

Abstract

Mehrnaz Tabibi.

OPTOACOUSTIC IMAGING OF GOLD NANOROD BASED PHOTOTHERMAL THERAPY

M. Sc. Biomedical Physics Ryerson University,

Toronto, 2011

Gold Nanorod Photothermal Therapy (GNR-PTT) is a minimally invasive technique and an alternative to surgery for destroying tumors while sparing normal tissues. Gold Nanorods (GNRs) with strong extinction peaks in the near infra-red (NIR) spectrum is a good candidate to convert light into thermal energy to destroy tumors.

Opto-acoustic imaging (OAI) is a non-invasive method that detects time-resolved acoustic waves created by short pulses of NIR in tissue. It leads to a pressure rise in the irradiated volume. The question of whether OAI is a suitable candidate for temperature monitoring of GNR-PTT in the NIR spectrum was examined.

In this thesis, for the first time, GNRs in a gel phantom was used to monitor the temperature during PTT with different laser powers and GNR concentrations. The imaging was performed by a commercial device IMAGIO, Seno, TX. The results show changes of the OA signal follow to temperature changes. The concentration of GNR and the power have a significant role in producing good results.

Acknowledgements

Completing my thesis work, which was like a mountain surpassed with exultation, but I know there are much higher and repugnant mountains for soaring.

It is a pleasure to thank the many people who made this thesis possible.

I would like to express my deep and sincere gratitude to my supervisor, Dr. Michael Christopher Kolios. With his enthusiasm, his inspiration, and his great efforts to explain things clearly and simply, he helped me to enjoy Physics. His passion and dedication to the field of Medical Physics is inspiring, motivating and contagious. His wide knowledge, detailed and constructive comments and personal guidance have provided a good basis for the present thesis.

It is difficult to overstate my gratitude to my other supervisor, Dr. Joseph Carl Kumaradas. I appreciate all his contributions of his understanding, support, time, marvelous ideas, compassionate company, and tactics for teaching using strong fundamentals; logical way of storm thinking, and creating a methodology by organizing and classifying decisions. His ideals and concepts have had a remarkable influence on my entire career in the field of biomedical physics research. I would have been lost without him.

I owe my most sincere appreciation to my committee member, Dr. Yuan Xu, for his valuable advice, brilliant suggestions and friendly help. His vast knowledge in optoacoustic imaging, and extensive discussions around my work and interesting explorations in signal analyzing and image processing, have been very helpful for this study. He dedicated tremendous amounts of time to guiding me. I acknowledge him for his warm reception and answering my questions so often.

Special words of appreciation go to my other committee member, Dr. William Mike Whelan, from University of Princess Edward Island, who often participated through on line methods. A significant portion of my knowledge in optics comes from my scientific discussions with him. He kept an eye on the progress on my work and provided me with invaluable ideas and suggestions regarding the optics and provided a lot of feedbacks to correct my final thesis.

This work would not have been possible without the technical support provided by Arthur Worthington with his knowledge in ultrasound, technical issues, and tool making. He has always been available for me to learn how to make a gel phantom, use lasers, and set up experiments. This thesis could not have been initiated nor finalized without his sincere collaboration.

Many thanks to Dr. Sankar Narasimhan, who guided me through my experiments. He was an ongoing help and guided me in solving the optoacoustic imaging problems and also getting Gold Nanorods spectrums and TEM imaging.

Particular thanks and gratitude go to Dr. Ana Pejović – Milić for her passion, excitement and enthusiasm about physics motivated me to come to this field.

I would like to express my sincere gratitude to the program administrator, Mary Neelands, who always helped me in numerous ways. Her support and understanding helped me to get energy, and to overcome all the difficulties of my life which I have faced.

I would like to thank all of the people of physics department at Ryerson University, faculty, administrative staff, Tess Sy and Sally Noce, and technical staff, Leonardo Zambito, Matthew Forest, and Graham Pearson, who made on-line connections and solved IT problems.

The last two and half years was one of my worst years of my life, I experienced the most excruciation time of my life. Losing my father and facing an atrocious living period, which made my life insufferable. But by having some precious friends of graduate schools, like Nazanin Nayebi, Hisham

Assi, Omar Falou, Elena Renzhiglova, Helen Moise, Shahrad Jabbary Aslany, Yevgeniy Davletshin , Devesh Bekah, Jason Zalev, Ozkan Doganay , Benjamin Lee, Radoslaw Sadowski, Amin Jaffari Sojahrood, Angelina Protic and specially mention Mira Sibai, Golafsoun Ameri, Siavash Rahimian, who provided a stimulating and fun environment; in which to learn. This made me maintain hope and not to give up. I would like to take the opportunity to thank those people.

Finally, in the last and the most, I owe my loving gratitude to my beloved father, Mohammad Sadegh Tabibi, whose golden hearth was filled with kindness and endearment. Although, I have lost my tranquility after losing him, his memory always remains with me. He taught me perseverance, hope and kindness. It is really hard to how to thank him who dedicated all of his life for us. I would like to heartily appreciate my mother, Maliheh Ahmadi, who has supported me in all my life, in spite of all her crisis years and taught me sacrifice and amnesty and to resist against all tough problems. Thanks my sister, Mozhgan Tabibi, for always accompanying me and supporting me in different ways. My special gratitude is due to my concept of hope in my life, my son, Takin Tadayon, for his magnificent understating, and who kindly accepted my situation and against all his problems made my life smoother and optimistic.

Dedication

To my beloved Father,

who taught me perseverance, hope and kindness.

To my lovely mother,

who taught me sacrifice and amnesty.

To my precious son,

who always dedicates me hope.

Table of Contents

List of Figures

List of Tables

Nomenclature

T	tissue temperature (K)
C	specific heat capacity (J/kg/ K)
k	thermal conductivity (W/m/K)
ω_b	blood perfusion rate (kg/m^{3}s)
C_b	blood specific heat capacity (J/kg K)
T_b	blood temperature (310.15 K)
Q_S	heat source or external heat term (W/m^3)
c_s	speed of sound in the substance (m/s)
ΔV	changed in volume by the thermal expansion (m^3)
V	the initial laser-irradiated volume at room temperature (m^3)
ρ	density of the medium (kg/m^3)
C_P	heat capacity at constant pressure (J/kg/K)
C_V	heat capacity at the constant volume (J/kg/K)
β	thermal coefficient of volume expansion (K $^{-1}$)
E_a	the absorbed energy density (J/m^3)

y	distance of the OA signal to the transducer between transducer and OA laser (mm)
$H(y)$	laser fluence (W/m^2)
τ_p	duration of laser pulse (s)
δ	optical absorption depth (mm)
μ_a	optical absorption coefficient of the substance (m^{-1})
$\mathcal{E}$	extinction coefficient($L\ mol^{-1}\ cm^{-1}$)
A	optical absorbance (unitless)
γ	thermodynamic coefficient of isothermal compressibility (bar^{-1})
Γ	parameter (Dimensionless)
P	optoacoustic signal (Pa)
ΔP	pressure change in optoacousitc signal (Pa)
τ	fast-time (time of transducer detection since the sound wave is generated) (ns)
t	slow-time (time after starting the experiment) (s)
T_r	Transmission coefficient of light (unitless)
c	concentration of gold nanorod in solution ($mol\ L^{-1}$)

Chapter 1

Introduction

1.1 Cancer

Cancer is a term used for a group of diseases in which abnormal cells divide without control and are able to invade the surrounding and distant healthy tissues. Cancer cells can spread from its origin to other parts of the body area through the blood and lymph systems. This spread, called metastasis can result in death [1].

Chemotherapy, radiation therapy, immunotherapy, hormone therapy and removal or destruction of the tumor by surgery or ablation, or a combination of these approaches are typical cancer treatments [2, 3]. The most direct therapeutic intervention for cancer is surgery. Removing all cancerous cells is the goal of cancer surgery. Choosing surgery depends on factors such as type, size, and location of the tumor. Cancer surgery is not suitable for the treatment of smaller and poorly visible tumors that are deeply embedded in crucial organs.

New treatment methods like high intensity focused ultrasound (HIFU), Laser Interstitial thermal therapy (LITT) and radio frequency (RF) ablation are alternative choices for cancer surgery [2-4].

1.2 Thermal Therapy

Many sources of energy, including laser, microwave, and ultrasound are being investigated for tissue heating. Each has advantages and disadvantages. HIFU is a non- invasive

method that can raise tissue temperatures up to 100 ºC. Long duration treatment and non-specificity are disadvantages of HIFU. Although RF ablation and microwaves are both non-invasive methods of thermal therapy, they are restricted to being close to the tissue.

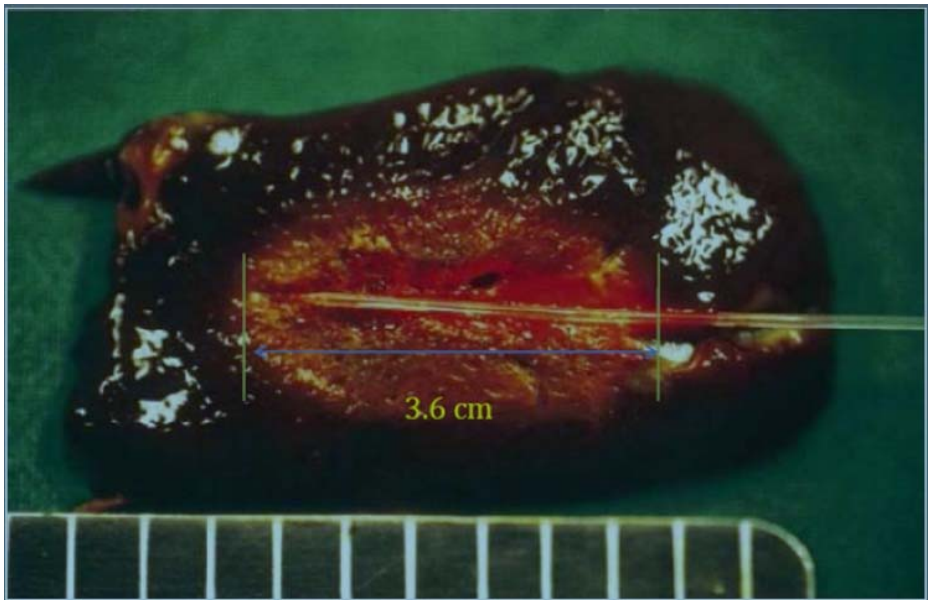

Figure 1.1 LITT in ex-vivo porcine liver. The lesion was created using 6W laser for 6 minutes. Lesion with this size cannot be created in-vivo because the cooling effect of blood perfusion. [Adapted from Heisterkamp et al.]

Thermal therapy dates back to 1700 BC when the glowing tip of a fire drill was used for breast cancer therapy [5, 6]. It targets small localized solid tumors to destroy them by coagulation. Because of the poor blood supply to the tumors, their heat tolerance compared to normal tissue is reduced, leading to their destruction. Hyperthermia causes irreversible cell damage by fluidizing cell membranes and denaturing proteins [6, 7].

Thermal therapy in the temperature range from 41-47 ºC has had limited success. Cell death is the result of coagulative necrosis which happens after heating of tissue above 55ºC for two minutes [8-11]. Temperatures greater than 55ºC, particularly 60 -100 ºC or even more, led to

significant tissue ablation and a successful result. The goal of thermal therapy is to ablate the tumor plus proper distance of margin in the surrounding to normal tissue [4].

Clinical trials have shown thermal therapy is a suitable treatment for head, neck, sarcoma, melanoma, lung, prostate, brain, breast, bladder, cervix, and liver [12].

The usage of light as a therapy modality has been known for more than three thousand years ago, when ancient Egyptian, Indian and Chinese civilizations applied it to treat various diseases, like psoriasis, rickets vitiligo and skin cancer. More than 100 years ago, researchers also observed combination of light and certain chemicals could induce cell death [13].

Ophthalmologists in 1963 reported using lasers in surgery. In 1965 tumor eradication was reported by laser, and then was followed by much attention in late 1960s. There are two ways for transmitting laser light: 1- external: exposing light on the tumors in the air by optical fiber tip, 2- interstitial: distributing into a restricted area by inserting the unconcealed end of the fiber into the center of the target tumor. The second method is called interstitial laser hyperthermia [6].

Monochromaticity, collimation and coherence identify laser light characteristics. These three make a high precised and minimal power loss of a high intensity narrow beam, which transmits almost deep down into the target tissue [6].

Photothermal therapy has been demonstrated using near infrared (NIR) radiant energy and metal nanoparticles. The nanoparticles efficiently absorb radiant energy and convert it to heat, leading to temperature increases up to 50°C or more [12, 14, 15].

Penetration depth of the laser irradiation in tissue is one of the crucial concerns in imaging and therapy. The absorption coefficient of the various tissues is one of the factors which decrease the penetration depth and it depends on the wavelength. High power laser output up to tens to hundreds of watts has to be used to efficiently induce the tumor ablation [18, 19].

1.3 Gold Nanorod Thermal Therapy

Photothermal therapy alone does not distinguish between cancer and normal cells. Nonselectivity is the major disadvantage of laser therapy. Both normal and tumor cells in the path of laser light are damaged. The use of optical photo-absorbers are taken up by a tumor, is one solution for overcoming this problem. It causes normal tissues to not drastically absorb Near Infra Red (NIR) wavelengths, and minimizes the damage. Photo-absorbers are able to generate optical resonance in the region in the tumor. They absorb light and it guides to transitions of electrons from the ground level to the excited level. The electronic excitation energy consequently relaxes through non-radiative decay processes channels. This leads to an increase in the kinetic energy and creates overheating of the local environment around the light probe, in the tumor lesion. The temperature creates tissue coagulation and cell death [18].

In recent years, development of nanotechnology has afforded a variety of nanostructures with unique optical properties that are valuable in biology and biomedical applications [20].

Introducing photo-thermal agents in the form of anisotropic gold nanoparticles is one approach. Plasmon-resonant gold nanoparticles are appealing in several respects: (a) their intrinsic toxicity is low; (b) their optical resonances can be optimized for specific NIR frequencies by a function of size and shape of the particle; (c) their small size (<100 nm) enable

transport through vessels and adsorption by diseased cells and tissues; and (d) their plasmon enhanced properties enable them to serve as contrast agents for biological imaging[18, 21].

Strong absorption cross section and highly efficient light to heat conversions are the basis of photothermal agents. These factors decrease the amount of energy and ensure effective laser therapy at relatively lower energies rendering the therapy method minimally invasive. At present, gold nanospheres, gold nanorods, gold nanoshells, gold nanocages, and carbon nanotubes are the principal nanostructures that have been used in photo thermal therapeutics. Gold nano- particles strongly absorb light due to their surface plasmon resonance (SPR) oscillations in the visible and NIR regions. They have distinctive specifications: easily prepared, capable of functionalization and tunable optical properties [18] .

In pre-clinical investigations of photothermal therapy, increasing the temperature as much as 30°C higher than initial temperature was produced using near infrared laser light tuned to matching photoasborbers causing irreversible tumor damage [15-17].

Gold nanoparticles are hydrophobic. After injecting the nanoparticles in the blood, they are exposed to plasma proteins. The reticulo-endothelial system removes them rapidly from blood circulation. However, coating the nanoparticles with hydrophobic polymer chains such as polyethylene glycol can improve the blood circulation time notably and it can restrain the immunogenic responses.[6, 17]

Gold nanoparticles can have desirable chemical properties; they are chemically stable and inherently biocompatible, and they do not interact with other existing components in a tissue microenvironment. In the past, gold nanoparticles (GNP) have been used for long term treatment of rheumatoid arthritis with doses of up to 1.2-1.8g/year for 10 years. Such lengthened treatment

time with gold salts lead to the creation of gold crystals and their deposition in macrophages [6, 17]. This is known a chrysiasis. It has no pathological effects and is considered to be merely cosmetic. In addition, chrysiasis only develops after passing the threshold of at least 20mg/kg gold content or after directing a few grams intravenously. Therefore, the long term exposure to GNP does not seem to have detrimental effect [18].

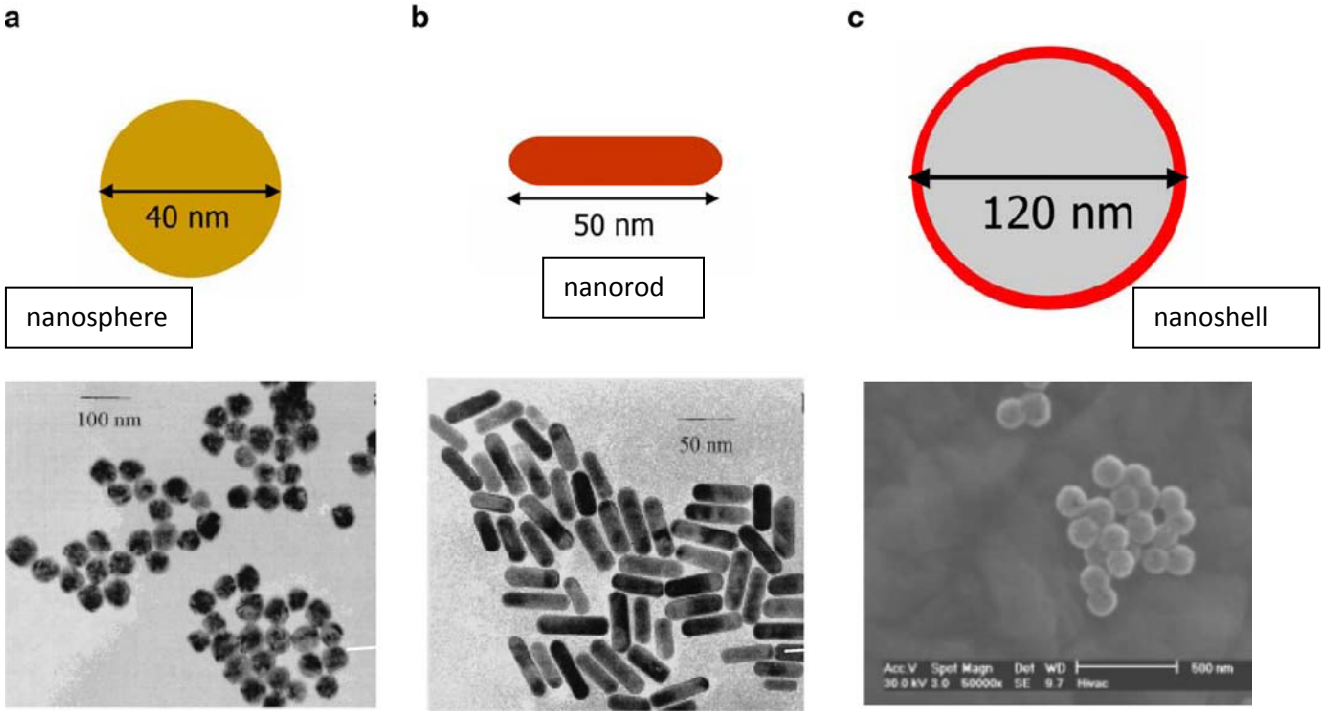

Figure 1.2 Plasmonic gold nanostructures commonly used for PTT –adapted from El-Sayed et al [3]

Preclinical studies with gold nanoshells in mice have shown potential therapeutic effects with biocompatibility and there is no cytotoxicity associated with the particles [14, 17]. El-Syed, calculated the expected absorption and scattering properties of different types of gold nanoparticles. By reviewing the optical properties of different shapes and sizes of gold nano-particles, Gold NanoRods (GNRs) supply the strongest light absorption for their size [22].

The relation between the aspect ratio of gold nano-rods and their peak absorption is presented in Fig.1.3. By increasing aspect ratio, gold nanorods absorb light at longer wavelengths.

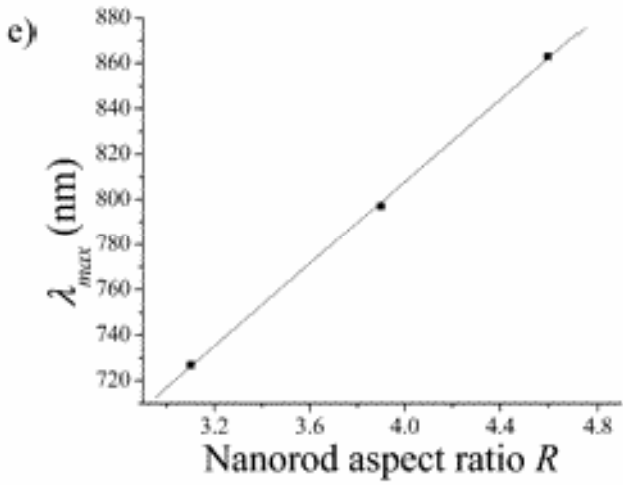

Figure 1.3 The relation between the aspect ratio of GNR and their peak absorption wave length copied from El-Sayed 2006

1.4 Monitoring Gold nanorod Thermal Therapy

As it was already mentioned irradiating with laser light creates SPR of nanoparticles and it generates heat. The SPR increases the temperature of hot electron of the nanostructures to reach thousands of Kelvins on the time scale of about 100 ps [18]. The temperature pattern is able to reach tens of degrees Celsius. During photothermal therapy, it is desirable to monitor, noninvasively, the tissue temperature for safety and efficacy. The ideal spatial resolution for the control over temperature distribution has to be on the order of a millimeter, and temperature resolution should be less than 1 ºC. There are various techniques for monitoring the temperature during photothermal therapy [22].

Each monitoring technique has advantages and disadvantages [23]. Although infrared thermography is a real-time method with 0.1ºC accuracy, it is limited to surface temperature measurement only [12]. Ultrasound (US) is an inexpensive method; it can be applied for real time measurements at depth, however, the accuracy of temperature monitoring is poor and the temperature range is limited to 5 ºC. The other technique is Magnetic Resonance Imaging (MRI). High resolution and accuracy are its advantages. Disadvantages are the complexity of the technique implementation, and expense [12].

1.5 Optoacoustic Monitoring

Optoacoustic imaging is a novel technique to measure temperature by tracking the temperature- induced changes in the optoacoustic signal amplitude [24, 25]. To create a strong optoacoustic signal two conditions should be met: thermal confinement and stress confinement. To achieve thermal confinement, the laser pulse duration, τ_p, should be smaller than the thermal dissipation duration, τ_{th}, (in other words the heat diffusion is minimal during the excitation pulse). To achieve stress confinement, the time for the stress to travel through the absorbing structure should be smaller than, τ_p.

After fulfilling both conditions, the pressure rise *P(z)* due to the thermoelastic expansion produces an optoacoustic (OA) signal.

Optoacoustic pressure generation was discovered by Alexander Graham Bell in the end of the 19th century [12]. First he reported the observation of sound generation by light in 1880. He showed that thin discs emitted sound when exposed to a beam of sunlight that was rapidly interrupted with a rotating slotted disk. The absorbed energy from the sunlight is transformed

into kinetic energy of the sample. This results in local heating with expansion of the absorbing material, produces a pressure wave, or sound.

The optoacoustic technique has been recently applied in biomedical imaging. Some of the applications are breast tumor imaging, real time blood oxygen monitoring, brain functional and structural imaging, and tumor angiogenesis [7, 26]. Also OA imaging can be a suitable candidate to monitor the temperature of tissue during thermal therapy. This technique is real time in clinical applications such as ophthalmologic laser surgery and photothermal therapy [27, 32].

The GNR may be the best preference for thermal therapy not only due to the preferential heating that can be achieved but the fact that using OA imaging can be used for a temperature monitoring. GNR absorption is very sensitive to the aspect ratio (length/width). Additionally, their peak absorption can be tuned in the NIR by adjusting the aspect ratio for these nanoaparticles.

1.6 Hypothesis

The objective of this research is to explore the potential of using optoacoustic imaging for monitoring the temperature variation during a photo thermal procedure. Also this research attempts to verify that optoacoustic imaging is a reliable technique for detecting and imaging tissue mimicking gel phantoms with GNRs.

Therefore the hypothesis is that optoacoustics can be used to detect heating caused by gold nanorod photothermal therapy.

Chapter 2

Theory

2.1 Optoacoustic (OA) Generation

Optoacoustic imaging is a method that relies on absorbtion of electromagnetic energy and consequent acoustic wave generation. By irradiation a medium with a 5 to 10 nanosecond pulse an instant rapid heating around 0.01 -1°C is produced; it causes an expansion or a strain in the substance (around 10^{-5}) resulting in a broad band acoustic wave. The wave detected by a transducer exhibits a pressure rise, ΔP, in the irradiated volume and is represented by a voltage increase as shown in Fig 2.1.

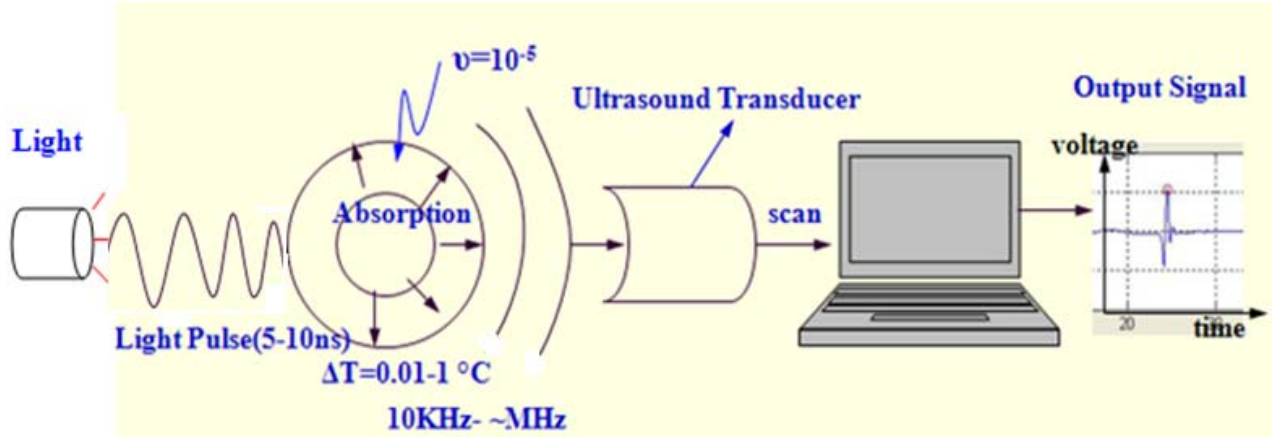

Figure 2.1 Schematic representation of the generation of optoacoustic signals by detection of ultrasound transducer of hit light pulse to the tissue.

An optoacoustic signal is produced by the transient heating of a restricted volume using light energy. This condition is referred to as "stress confinement" and for providing this condition, it is necessary that a laser pulse irradiates the object in a very short time to achieve stress confinement. The duration of the laser pulse should be much less than the amount of time that acoustic energy needs to propagate out of the area of absorption [28].

In a planar medium, there is represented as the

$$\tau_p \ll \frac{\delta}{c_s} \tag{1}$$

where the duration of the laser pulse,τ_p, the speed of sound in the medium, c_s, and the optical absorption depth, δ, as described by [28].

Generally three categories of tissue properties can effect the generation of an optoacoustic wave.

2.1.1 Optical property (Pure absorption)

According to the Beer Lambert Law [29-31], there is a logarithmic dependence between the transmission (or transmissivity) of light, $T_r = \frac{I}{I_0}$ (2)

through a substance or product of the absorption coefficient of the substance, μ_a, and the distance the light travels through the material, ℓ. The absorption coefficient can be related to:

$$\mu_a = \varepsilon c \tag{3}$$

as a product concentration, c, by extinction coefficient, ε.

$$\frac{I}{I_0} = 10^{-\mu_a \ell} = 10^{-\varepsilon \ell c} \quad (4)$$

I is the intensity after depth ℓ and I_0 is the initial intensity of light. When large absorption values are measured, dilution is required to achieve accurate results.

Therefore,

$$A = -\log_{10}\left(\frac{I}{I_0}\right) \quad (5)$$

Also, absorbance becomes linear with the concentration (or number density of absorbers)

$$A = \varepsilon \ell c \quad (6)$$

$$I = I_0 e^{-\mu_a y} \quad (7)$$

$$H(y) = H_0 e^{(-\mu_a y)} \quad (8)$$

$H\,(y)$ is the fluence at depth y and H_0 is the fluence at the surface.

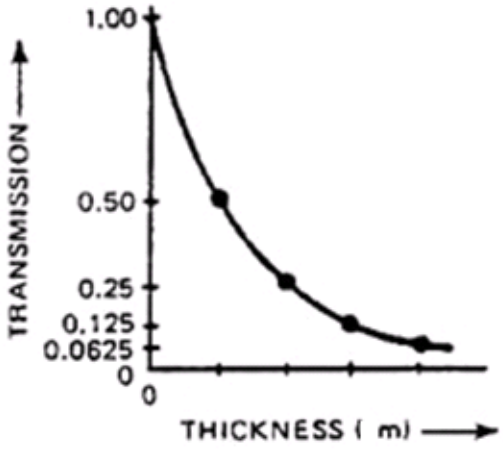

Figure 2-2 Transmission as a function of thickness[29].

Therefore, the attenuation of light has a direct relation to the concentration of GNRs. By diluting, the concentration of GNR, the absorption of the medium in will decrease [29-31].

Details about the GNR used in this work can be found in the chapter 3.

2.1.2 Heat Generation

The general formula for heat generation is:

$$\rho C \frac{\partial T}{\partial t} = \nabla . k \nabla T + Q_s \quad (9)$$

which ρ and C in order are the density and specific heat capacity of the medium. k is the thermal conductivity and Q_S is the external heat source.

There are two lasers utilized in this work. One is used to heat the phantom and another is used for optoacoustic imaging. The second item in equation (9) is the external heat source Q_s:

$$Q_s = H\mu_a \quad (10)$$

Q_s in photothermal therapy is dependent on the laser fluence, H, which characterizes the light distribution in tissue, and the tissue absorption coefficient, μ_a [27, 28] which in the presence of gold nanorods increases tissue heating.

In this thesis Q_s is the combination of both lasers heating and imaging.

Given the incident radiant exposure, $H(y)$ μ_a, the energy density can be expressed as a function of depth with the following equation .

$$Q(y) = \mu_a H_0 e^{(-\mu_a y)} \quad (11)$$

This energy will be converted to heat. H_0 , is the laser fluence on the surface incedience.

Gold nanorods generally behave as photoabsorbers in photothermal therapy. In clinical studies they are injected either directly into the tumor or intravenously. Because of the small size of nanoparticles (10-100nm), the incident nanosecond laser irradiation does not meet the principal requirements of stress and thermal confinement. In its place, there will be an instantaneous heating between nanoparticles and the immediate surrounding tissue. Therefore the nanoparticles act as a local heat source that their temperature decrease quickly and transfer to the surrounding tissue which increase the thermal expansion of tissue and leads to generate a strong optoacoustic signal without the existence of any photoabsorbers.

2.1.3 Mechanical

The pressure wave can be described as:

$$P(y) = \Gamma Q_s(y) \tag{12}$$

$$P(y) = \Gamma \mu_a H(y) \tag{13}$$

The Grüneisen parameter (Γ) is related to thermo-dynamical and mechanical properties of thre medium. Both the absorption coefficient of light (μ_a) and laser fluence (H) depend on the medium. Therefore the initial pressure distribution, P_0, following the laser pulse is directly proportional to the energy density function as follows:

$$P_0 = \Gamma \mu_a H_0 e^{(-\mu_a . y)} \tag{14}$$

Γ represents the fraction of absorbed light energy converted to mechanical (acoustic) energy.

Generation of optoacoustic waves is the result of the optical and mechanical properties of the medium. By considering the relationship between different parameters as shown in the

following equations, it can be shown that an induced temperature change yields a change in volume and leads to pressure variation, ΔP. So pressure, P, in any time or depth will be:

$$P = P_0 + \Delta P \tag{15}$$

$$\Delta P(y) = \frac{1}{\gamma}\frac{\Delta V}{V} \tag{16}$$

$$\beta = \frac{1}{V}\frac{\Delta V}{\Delta T} \tag{17}$$

$$\Gamma = \frac{\beta c_s^2}{C_P} \tag{18}$$

$$\Gamma = \frac{\beta}{\gamma \rho C_p} \tag{19}$$

$$\Delta T = \frac{E_a(y)}{\rho C_V} \tag{20}$$

Therefore equations (15-19) can be combined to produce (20).

$$\Delta P(y) = \frac{1}{\gamma}\frac{\Delta V}{V} = \frac{1}{\gamma}\beta\Delta T = \frac{1}{\gamma}\frac{\beta E_a(y)}{\rho C_V} = \frac{\beta c_s^2}{C_P}\mu_a H(y) = \Delta\Gamma\mu_a H(y) \tag{21}$$

which γ is the thermodynamic coefficient of isothermal compressibility. c_s is the speed of sound in the medium, ΔV is increased volume by the thermal expansion, V is the initial volume before laser irradiation at room temperature, ρ is density of the medium and C_P, C_V, β , E_a are heat capacity at constant pressure, the heat capacity at the constant volume, thermal coefficient of volume expansion and the absorbed energy density.

The Grüneisen parameter is a dimensionless, temperature dependent factor proportional to the fraction of thermal energy converted into mechanical stress.

For an increase in temperature from 20 °C to 30°C, the volume expansion coefficient of water changes from 0.2×10^{-3} $(K)^{-1}$ to 0.3×10^{-3} $(K)^{-1}$ and the speed of sound from 1481 m/s to 1507m/s [17]. This causes a 50% rise in optoacoustic signal for a 10°C increasing of temperature (an almost 5% per Celsius degree variation in signal amplitude).

As a result, the Grüneisen parameter, Γ, and thus optoacoustic signal is directly related to temperature in water based tissues[32].

$$\Gamma = a + bT \tag{22}$$

$$\Delta\Gamma = a + b\Delta T \tag{23}$$

$$\Delta\Gamma = \frac{\Delta P}{\mu_a H} = a + b\Delta T \tag{24}$$

$$\Delta P = a(\mu_a H) + b\Delta T(\mu_a H) \tag{25}$$

a and b are constants and T is the water temperature.

Eq. 23 proves a basis for monitoring temperature using optoacoustic pressure signals during the photothermal therapy.

Therefore the temperature variation is proportional to changes of OA pressure and Grüneisen parameter during photothermal therapy [24, 33].

Also, it can be written, if P is the initial pressure and P' is the pressure after OA laser illumination.

$$P = \Gamma\mu_a H_0 e^{-\mu_a y} \tag{26}$$

$$P' = \Gamma'\mu_a H_0 e^{-\mu_a y} \tag{27}$$

By dividing two equations 26 and 27:

$$\frac{P'}{P} = \frac{\Gamma'}{\Gamma} \tag{28}$$

$$\frac{P'-P}{P} = \frac{\Gamma'-\Gamma}{\Gamma} \tag{29}$$

$$\Delta P = P' - P \tag{30}$$

$$\Delta\Gamma = \Gamma' - \Gamma \tag{31}$$

$$\frac{\Delta P}{P} = \frac{\Delta\Gamma}{\Gamma} \tag{32}$$

$$\frac{\Delta P}{P} = \frac{\mathrm{a+b\,\Delta T}}{\mathrm{a+bT}} \tag{33}$$

$$\frac{a+b}{a+bT} = k \tag{34}$$

$$\Delta T = k\frac{\Delta P}{P} = k\frac{\Delta\Gamma}{\Gamma} \tag{35}$$

$$\Delta T = k\frac{\Delta P}{P} = k\frac{\Delta\Gamma}{\Gamma} \tag{36}$$

k is a constant that depends on the tissue which can be experimentally determined. ΔT and $\Delta\Gamma$, are the temperature rise and changes of Grüneisen parameter during temperature variation.

The optical absorption coefficient, μ_a, depends on the material being irradiated. It is that depth at which the optical energy delivered into the medium is attenuated. In an entirely absorbing medium the depth will be $\delta = 1/\mu_a$, although in a medium with combination of absorbing and scattering, the depth will be $\delta = 1/\mu_{eff}$.

Chapter 3

Materials and Methods

3.1 Overview of experiments

Experiments were carried out with 4 different (GNRs) dilutions located in the middle layer of gel phantoms. Each phantom was exposed with 4 to 5 different thermal laser powers (table 3.1). The experiment setup is discussed in section 3.2. GNR gel phantom construction is discussed in section 3.3.

Power (W) / Dilution Factor	2	2.5	3	3.5	4	5	8	10	12
2x	_	_	♣	_	_	♣	♣	♣	_
4x	♣	♣	♣	♣	♣	_	_	_	_
5x	_	_	_	_	_	♣	♣	♣	♣
6x	_	♣	♣	♣	♣	♣	_	_	_

♣ = experiment _ = no experiment

Table 3.1 Overview of the phantom gel heating experiments

3.2 Experimental Setup

The optoacoustic imaging system, IMAGIO, (Seno Medical Instruments Inc. San Antonio, TX, USA), (Fig.3.1), creates and detects sound pressure waves generated by stimulating the sample with pulsed laser energy to obtain images of structures inside the sample.

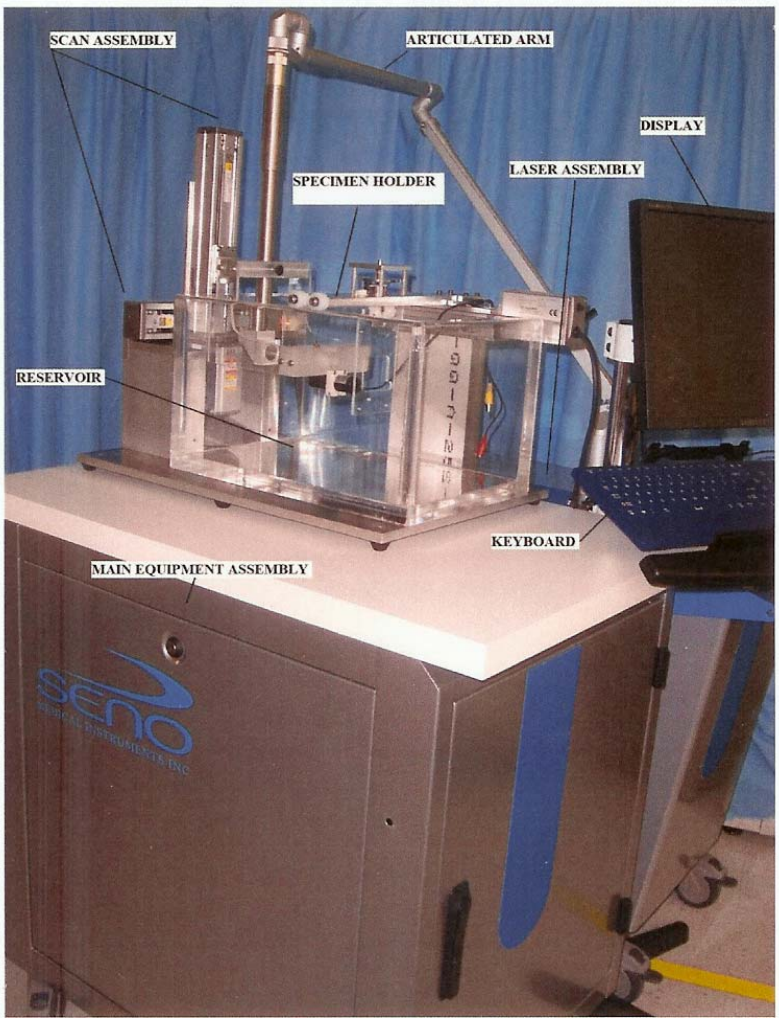

Figure 3.1 A view of IMAGIO, optoacoustic device used in all experiments

The main components of the system are a probe containing at least one ultra wide band ultrasound transducer with signal detection circuitry, an electronics unit containing data processing and image construction circuitry, a user control interface and a pulsed laser illumination source containing a laser source with a light delivery device (the articulated arm in (Fig.3.1)).

The phantom was placed in the examination reservoir near the probe in a manner that enables laser light to be applied to the GNR gel phantom. The space between the external layer GNR gel phantom and the detector elements require a coupling medium like water to fill the void so that ultrasonic waves can reach the ultrasound detector (Fig.3.1) [34].

The IMAGIO reservoir was filled with a sufficient amount of degassed water to cover the upper surfaces of the phantom; the location of the IMAGIO laser and the transducer are 5 cm below the top of IMAGIO reservoir (Fig.3.2), (Fig.3.5) [34]. The phantom mold was attached to a frame which was attached a phantom holder. The phantom was positioned between the laser light probe and the ultrasound transducer of the IMAGIO. The three coordinate axes of the device are shown in the (Fig.3.2).

The heating laser was a Diomed 60 (Cambridge Research Panel, Cambridge, UK). The laser was coupled to the phantom through a 1000 μm core, standard hard cladding multimode, low OH fiber (BFL37-1000-Custom, THORLABS, Newton, NJ, USA), which was situated over the phantom perpendicularly. The distance between the top layer of the phantom and fiber tip was around 25 mm, and the focal point of the heating laser was focused in the middle of the width of the phantom as shown in (Fig.3.3) and (Fig. 3.4).

AS fluoroptic thermometer (Luxtron Corporation, Santa Clara, CA, USA, model 3100), was embedded perpendicularly from the center of the top surface and inserted half way through the GNR gel phantom (Fig.3.4).

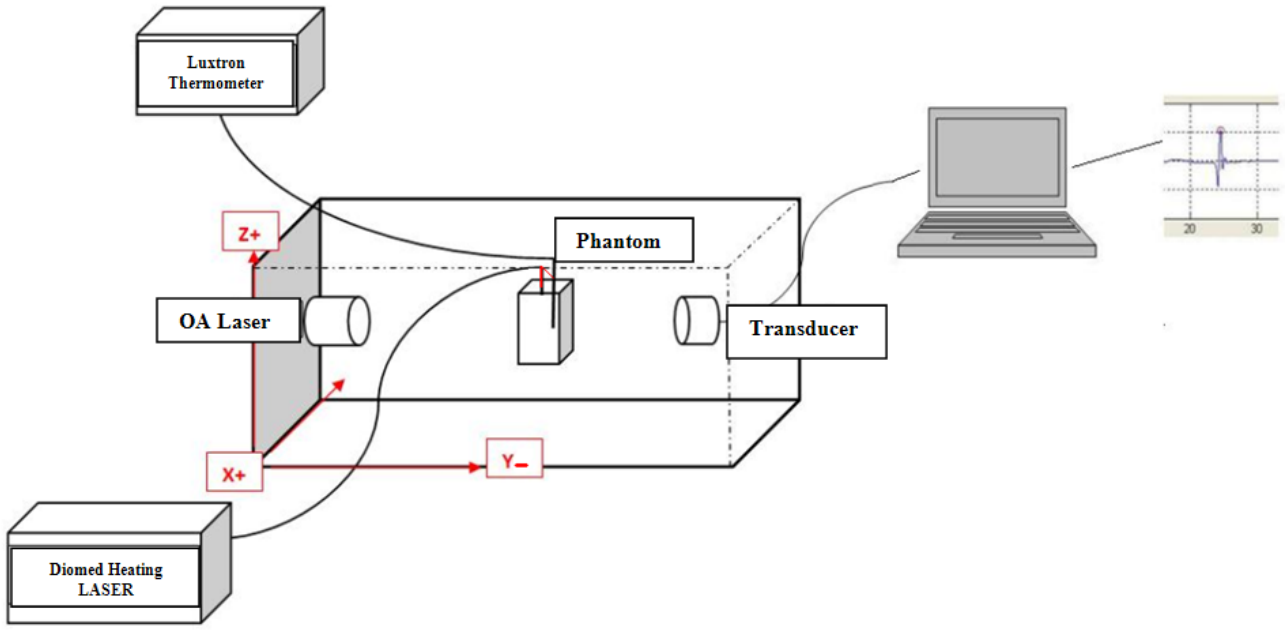

Figure 3 .2 Experiment setup

The focal point of the transducer array was determined to be around 25 mm ± 2.5 mm from the transducer surface. The middle layer of the phantom was placed at the transducer focus. The front surface of the middle layer of the phantom that contained GNRs, was 15 mm away from the transducer. This distance was measured manually by a ruler.

Averaging the received RF signals is one of the factors that increase the signal to noise ratio (SNR). Averaging is done by collecting several RF lines resulting from a number of laser pulses and averaging the RF lines in the time domain. The number of averages were 8,16 and 64 (table 4.1).

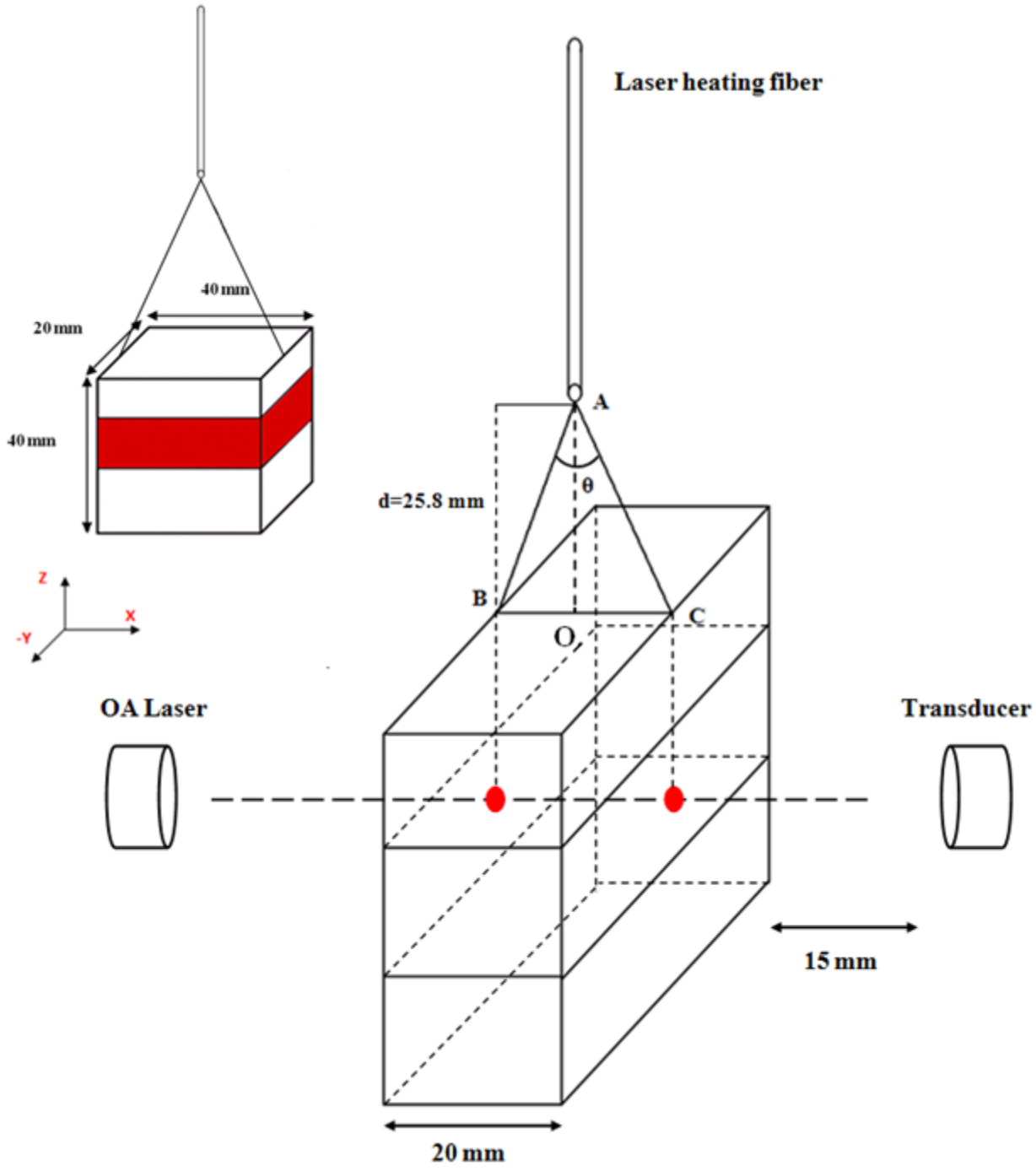

Figure 3.3 Photo thermal fiber adjustment

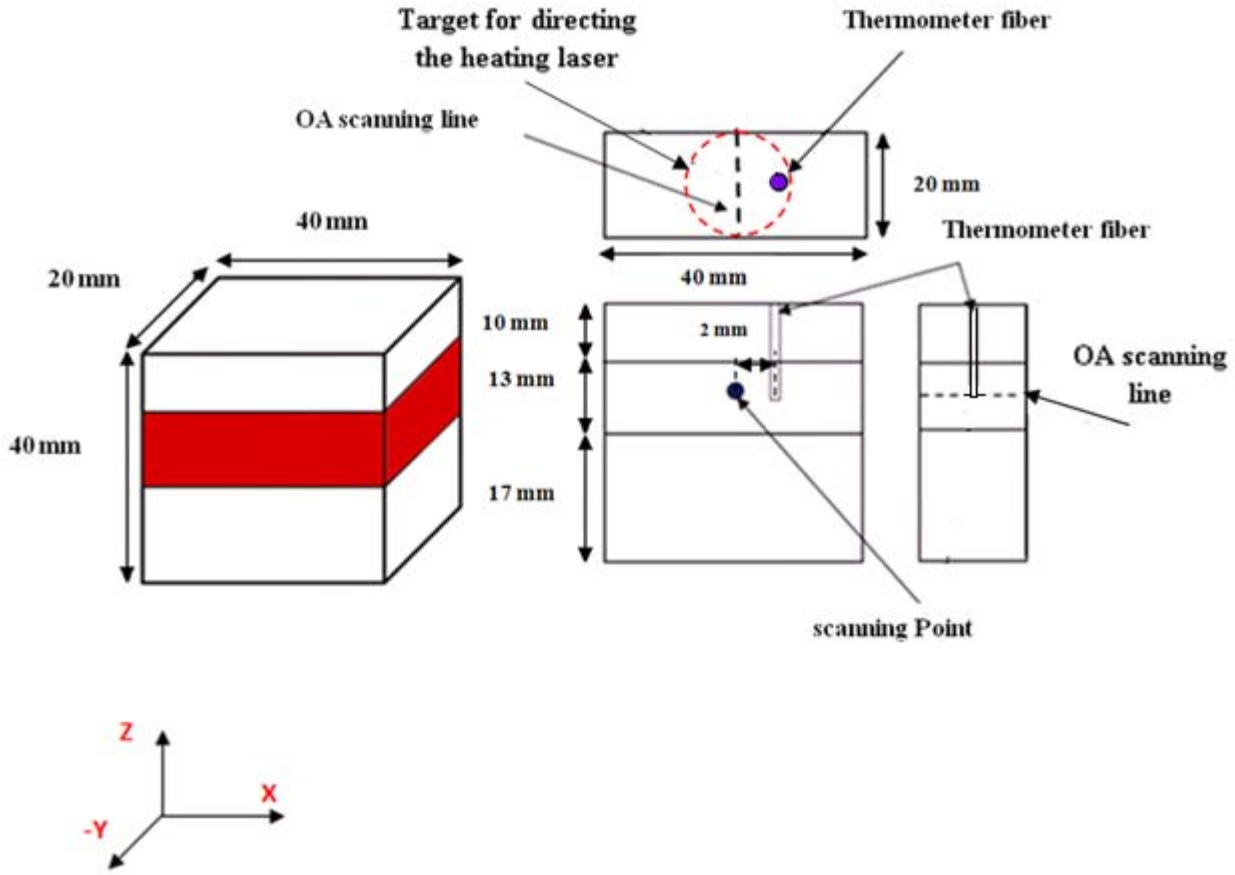

Figure 3 .4 Three layers phantom and its 3 views

The illumination wavelength used for the IMAGIO optoacoustic laser was adjusted according the peak point of the spectrum of GNR absorbance. The greatest absorbance is close to 765 nm, so the laser pulse of the IMAGIO device was adjusted to 765 nm (Fig.3.6).

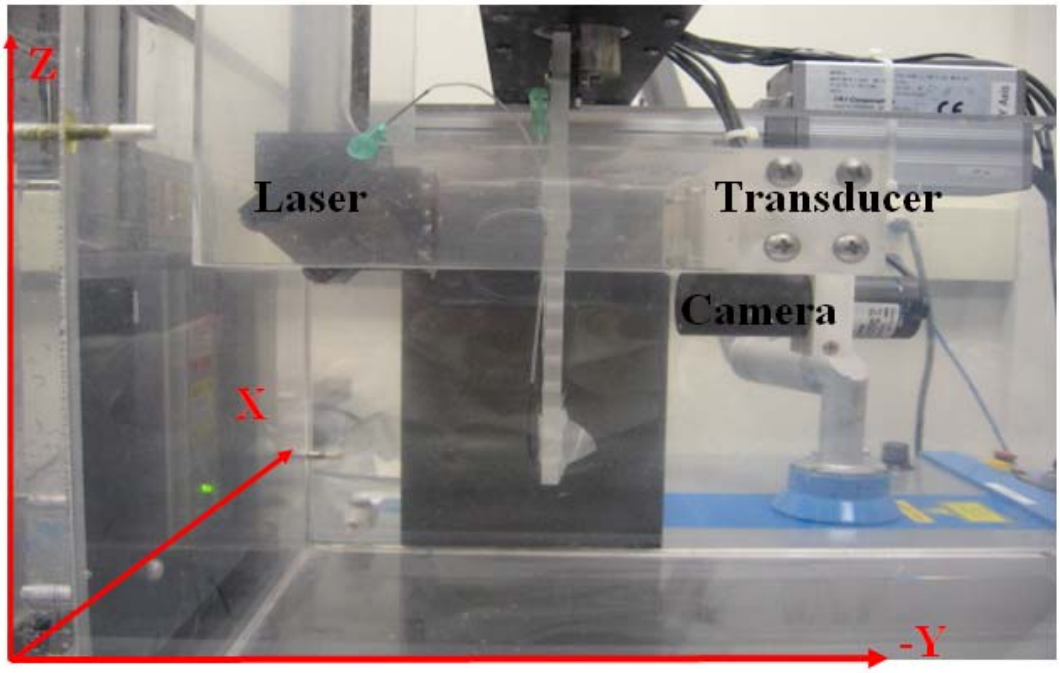

Figure 3.5 Side view photograph of the IMAGIO device and its components

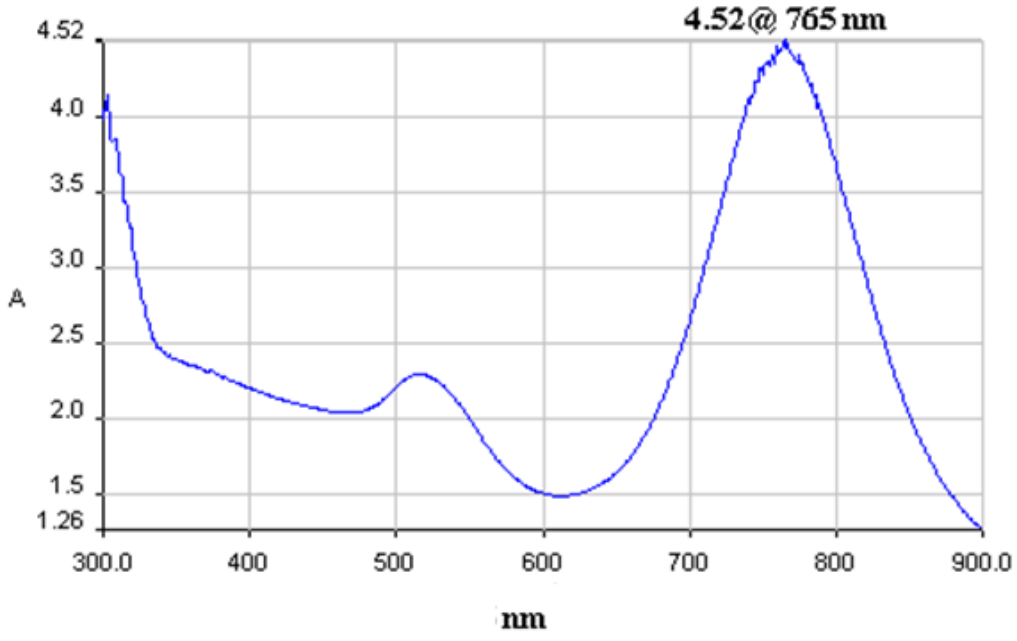

Figure 3.6 Absorbance vs. wavelength of experimental GNR(30 ×10)nm used in thesis experiments, measured by spectrometer

3.3 A tissue-mimicking Phantom preparation

A 40×40×20 mm^3 three layer (porcine skin gel- porcine skin gel with diluted GNR porcine skin gel) phantom was prepared (table 3-2).

Type	Ingredients	Composition by (Weight)	Manufacturer
pure gel	gelatin from porcine skin*	8.82%	Sigma
	degassed water	88.24%	-
	Formaldehyde **	2.94%	Sigma
gold nanorod gel	gelatin from porcine skin	8.82%	Sigma
	degassed water	$\left(\frac{X-1}{X}\right)$ ×88.24%***	-
	gold nano-rod solution	$\left(\frac{1}{X}\right)$ × 88.24%***	Warren Chan lab
	Formaldehyde	2.94%	Sigma

Table 3.2 Ingredients for making a GNR gel phantom

*Gelatin from porcine skin Lot# 119k0062 -Type A –G2500 –Bloom gel strength ~300 gr

**Formaldehyde 37wt. %, solution in water –histological grade

***X= Gold Nano-Rod fluid dilutions ratio

3.3.1 Layered Phantom geometry

The tissue mimicking gel phantom can be thought of as simplified layers of body tissues in three layers: two external layers and one internal. The upper layer of the gel is the external layer that may contain skin and similar tissues, and the middle layer mimicked a tumor with GNR were injected to enhance the imaging contrast and thermal therapy efficiency and the bottom layer was 3external layer (Fig.3.7).

3.3.2 Gel preparation

Porcine skin gelatin powder was added gradually to water which was warmed by a heater (Rose scientific Ltd, USA, model IKA C-MAG HS-7 S1) up to 90ºC as measured by a thermocouple (DATA LOGGER, OMEGAETTE HH306). The solution was stirred gently until the solution appearance changed to clear while ensuring the bubbles were not generated.

Then the container of liquid gel was put on magnetic stirrer (Cole-Parmer, UK, 300Ma) until the temperature of the liquid gel dropped to 42ºC. Formaldehyde was added to the liquid, and after the temperature dropped to 40ºC, the liquid was poured into a brick shape mold. The mold was kept in a fridge while GNR gel layer was made.

The procedure for making gel layer with GNR was identical with the first step except the water was replaced by a mixture of GNR and water and it was poured over the first layer into the brick shape mold. The third layer, a pure gel layer, was made similar to the first layer and was poured over the second layer. The three layered phantom was kept in the fridge until the entire phantom solidified.

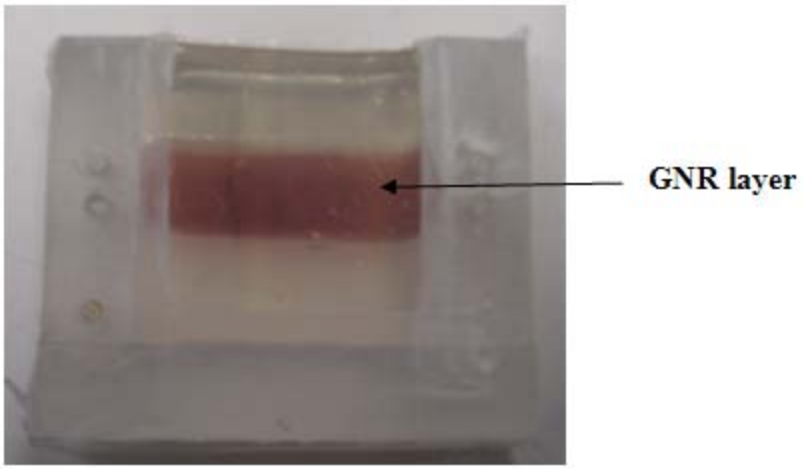

Figure 3.7 Picture of front view of three layer phantom

3.4 Data acquisition

3.4.1 Temporal Scanning at a specific point during photothermal therapy

The GNR layer was made to examine how GNR could be used for imaging (by enhancing contrast) and therapy (to increase the light absorption). The spatial location at which RF data were acquired as a function of time was in the center of the phantom in the X direction, which was located 1.5 – 2 mm farther of the tip of the sensor of fluoroptic thermometer (Fig. 3.4). The location chosen could not be closer to the thermometer for two reasons: light from the OA laser could be scattered by the fluoroptic sensor; and the sensor could produce an artifact if the scan point was too close to the sensor. RF data was acquisition in three phases: the preheat phase, the heating phase (when the laser was turned on); and the cooling phase (when the heating

laser was turned off) and RF data acquisition was continued for a pre-determined time or until the ambient temperature was reached.

3.4.2 Imaging before and after thermal therapy

The IMAGIO device scans in the X-Z plane to produce an image. For each location in the in the XZ plane, a line scan in the Z direction was performed in discrete spatial time steps while RF data were collected along the Y direction (Fig.3.2). Images were collected before and after heating.

The location of acquisition of single RF lines is at the center of phantom in the X direction. The duration of imaging depends on the area and step size. Another factor that affects the duration is the number of averages for the RF data. The number of averages can enhance the quality of the image by increasing the signal to noise ratio (SNR).

3.5 Data processing

After the experiment, all of the OA data sets were stored to a PC for further analysis. Images of the phantom were made in the preheat phase and after cooling. The A-scan or RF data were used to create data graphs to study the variation of the OA signal during thermal therapy for different powers and GNRs concentration (table 3.1). Also all of the temperature data acquired by Luxtron thermometer were stored for further analysis.

The Optoacoustic signal, P (τ, t) , can be calculated as a function of space and slow-time.

$$\mathrm{P}\ (y, t)=\mathrm{P}\ (\tau = \frac{y}{c}\ , \mathrm{t}) \qquad (37)$$

which τ is time difference between when the sound wave is generated and the detected called the fast-time, t is the duration time after starting the experiment called the slow-time, and y is the distance of the OA signal to the transducer along the horizontal line between transducer and OA laser.

In order to detect the envelope of the OA signal, the absolute values of the Hilbert transform $\mathcal{H}\{\}$ of the P (y,t) was determined, $P_{\mathcal{H}}(y,t)=\|\mathcal{H}\{\text{P }(y,t)\}\|$ [35].

Figure (3.8) shows the OA pressure signal P (y,t) (in mv) at 0.467 min, time at t_1. (Fig.3.9), (Fig.3.10) and (Fig.3.11) show $P_{\mathcal{H}}(y,t)$ for t_1 =0.467 min after starting the experiment, t_2 =3.8 min after starting the experiment, and t3 =4.75 min after starting the experiment, respectively, for illustrating the signal processing performed. The purple dashed lines show the boundary of the phantom.

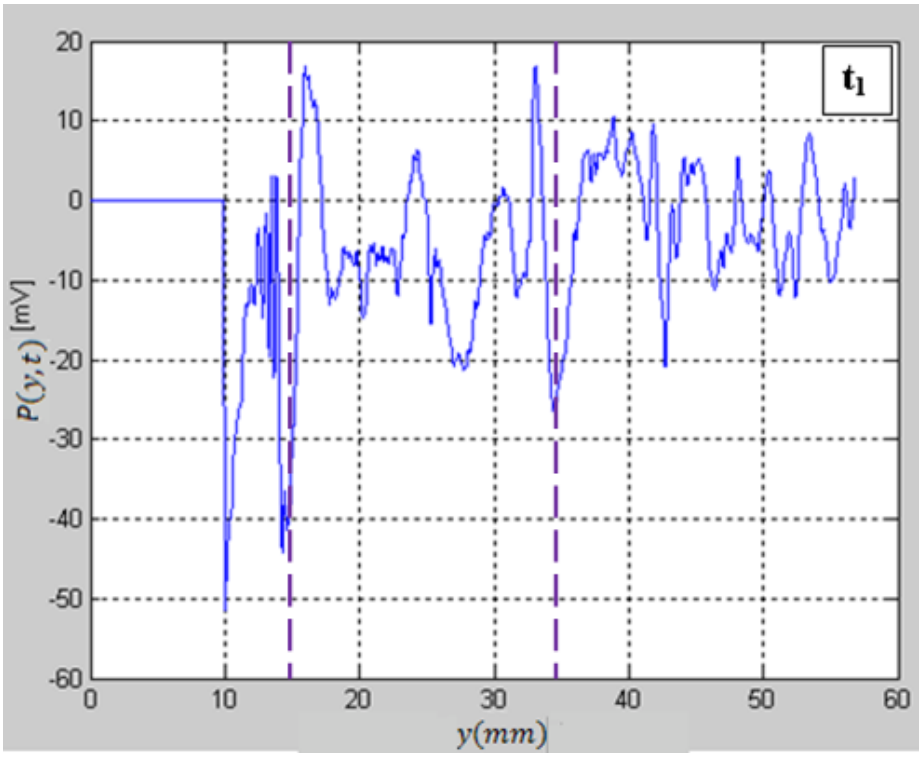

Figure 3.8 RF line of OA signal at t1=28 seconds (0.467 min) after starting of experiment for 2X-GNR phantom heated with a 10W laser exposure.

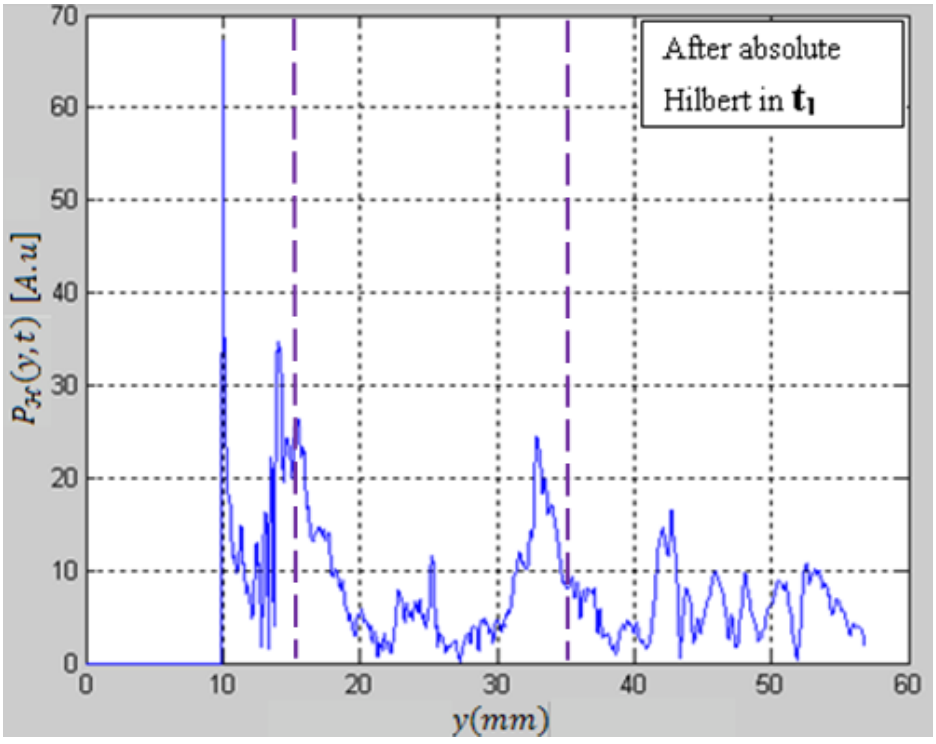

Figure 3.9 Hilbert transform of the RF line (A-scan) of the OA signal at t1=28 seconds (0.467 min) after starting of experiment for 2X-GNR phantom heated with a 10W laser exposure.

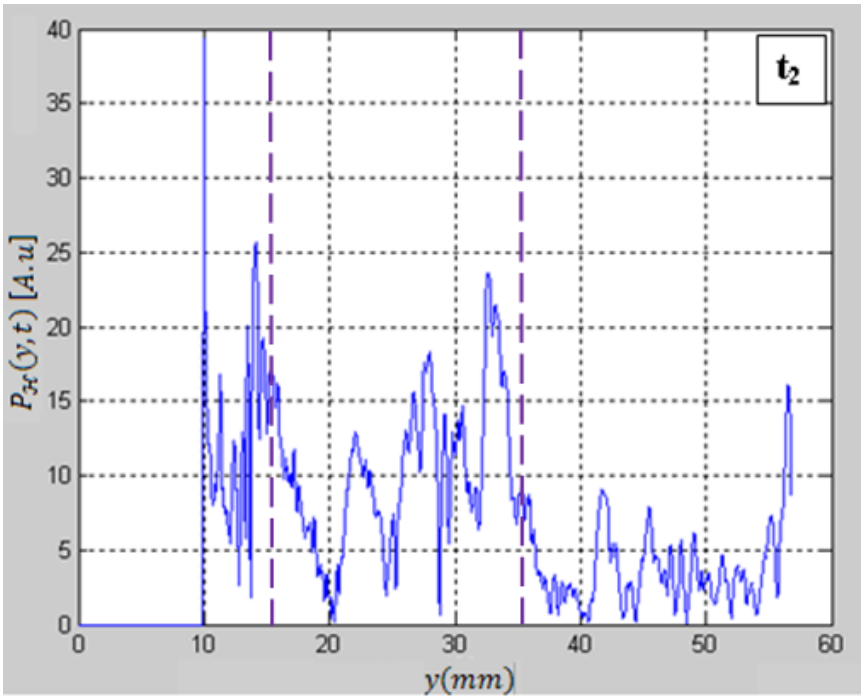

Figure 3.10 Hilbert transform of the RF line (A-scan) of the OA signal at t2=228 second (3.8 min)after starting of experiment in heating phase for 2X-GNR phantom heated with a 10W laser exposure.

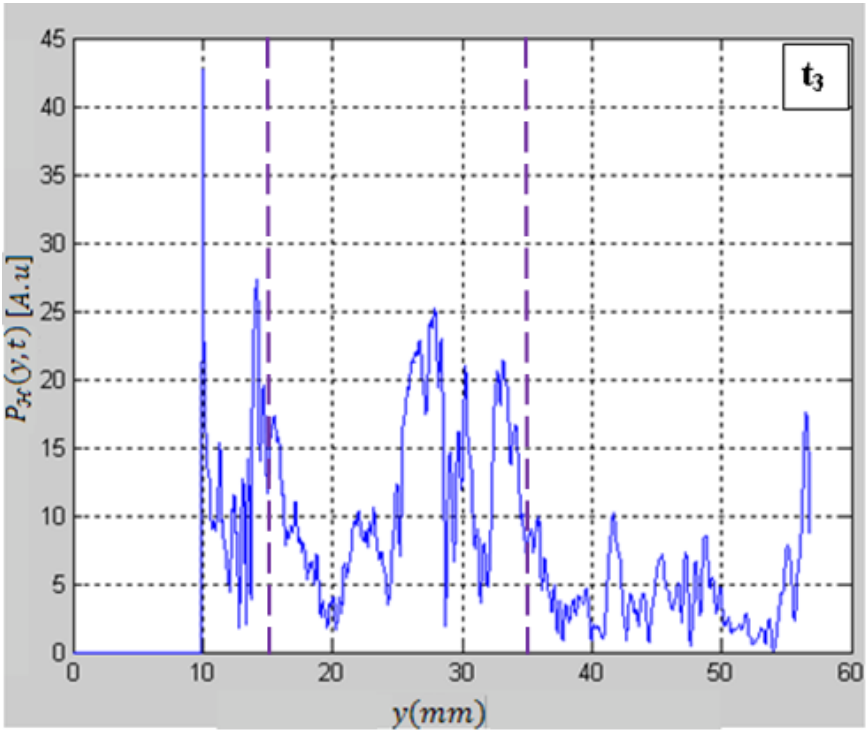

Figure 3.11 Hilbert transform of the RF line (A-scan) of the OA signal at t3=285second (4.75 min) after starting of experiment in heating phase phase for 2X-GNR phantom heated with a 10W laser exposure.

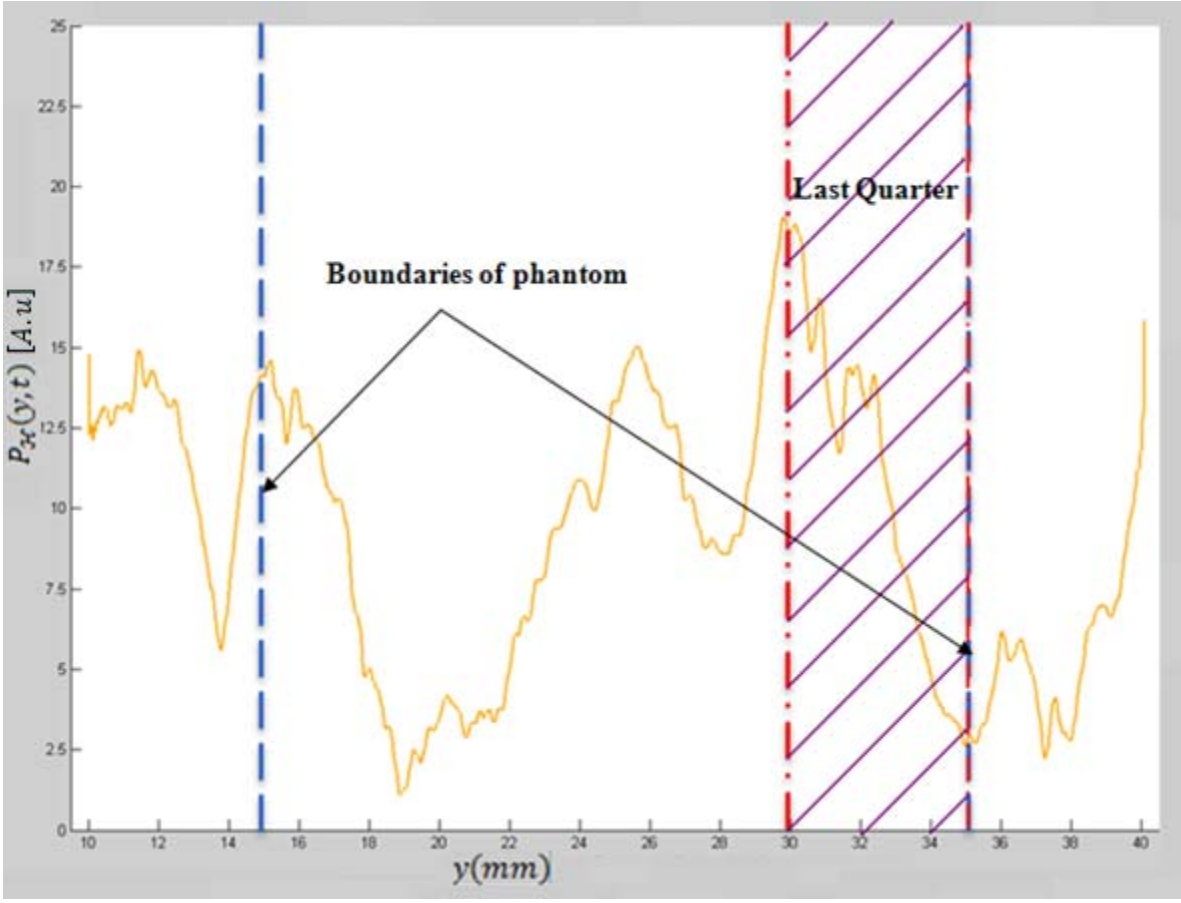

Figure-3.12 one RF line and area of integration and boundaries of phantom at t=228 seconds (3.8 min) after starting of experiment in heating phase for 2X-GNR phantom heated with a 10W laser exposure.

The last quarter of the RF signals collected during the experiments was analyzed. This represented the phantom region closest to the OA laser (Fig.3.12). This region had the highest optical illumination and should, therefore, produce the strongest optoacoustic signal provided the optical absorption in the GNR phantom was uniform.

The OA signal was integrated in this region to determine the area under the $I_{OA}(t)$ RF line between two distances of y_i *and* y_f.

$$I_{OA}(t) = \int_{y_i}^{y_f} P_{\mathcal{H}}(y,t)\, dy \tag{38}$$

Where the distances, y_i and y_f are measured from the transducer.

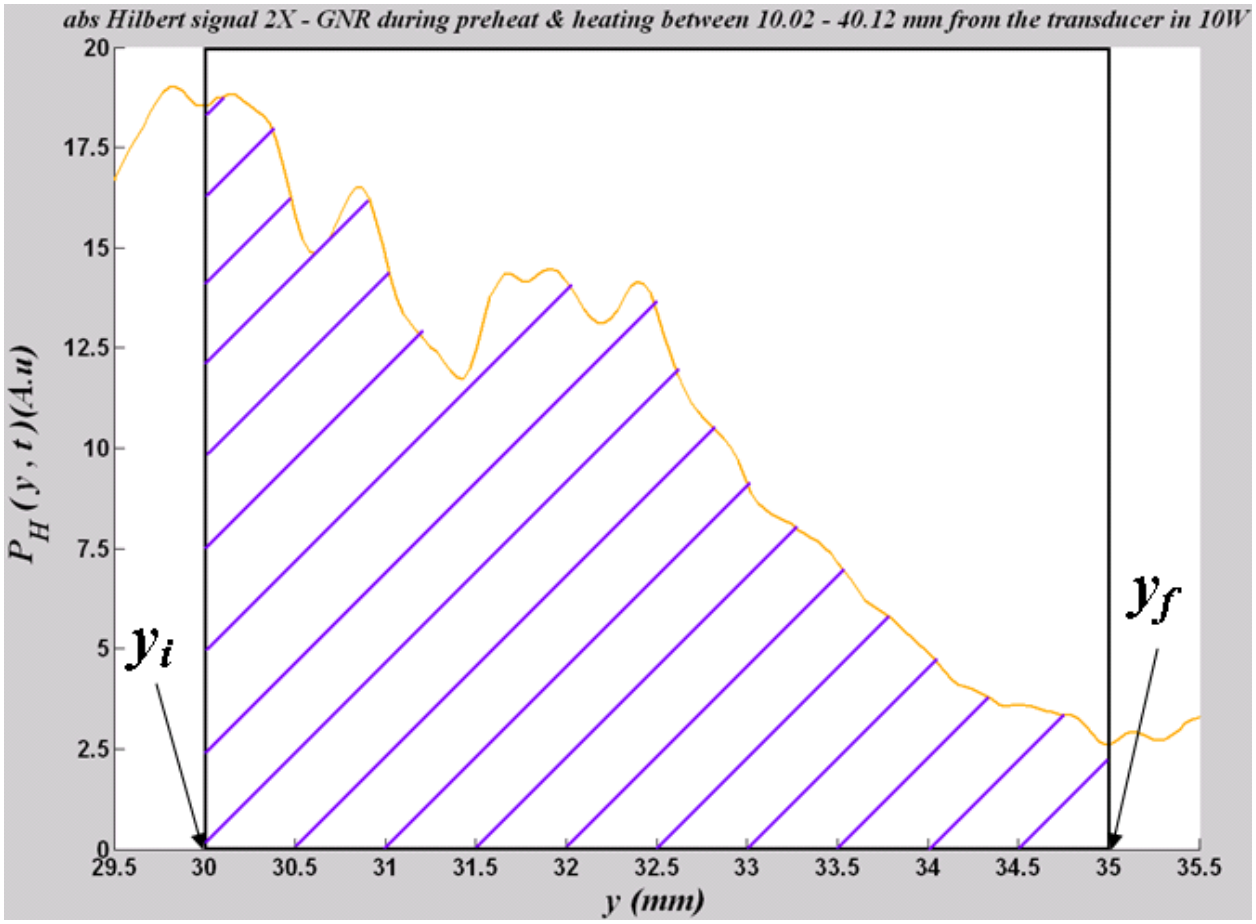

Figure 3.13 Integration area of RF line

To calculate the signal strength, for each RF line I_{OA} was calculated for different time points I_{OA} was then plotted as a function of time to investigate the temporal changes in the OA signal.

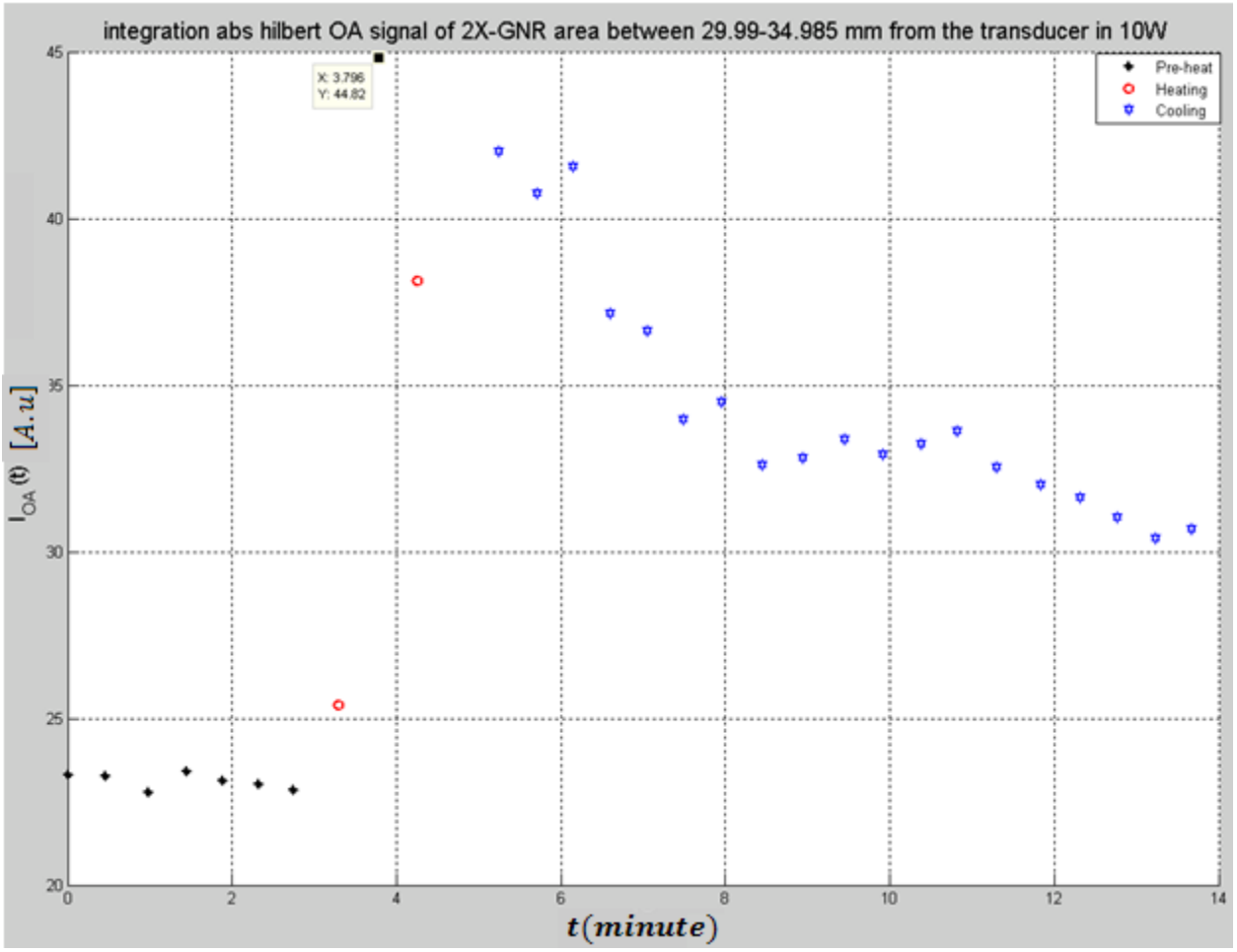

Figure 3.14 Integration of Hilbert OA signal vs. time

This was repeated RF lines collected as a function of time to produce graph of I_{OA} vs. t (Fig.3.14).

The data sampling of temperature vs. time was greater than the data sampling of I_{OA} vs. time since:

1- Temperatures were measured before OA measurement started and ended after OA measurements ended (Fig.3.15).
2- The time interval between temperature measurements data was shorter than that between OA signal measurements.

The two sets data of I_{OA} (*t*) and *T (t)* have time as a common axis. To relate I_{OA} (*t*) and *T(t)* and provide a common time axis, the I_{OA} data were interpolated to match the I_{OA} (*t*) time-points to produce I_{OA} (*T*) graph (Fig. 3.16).

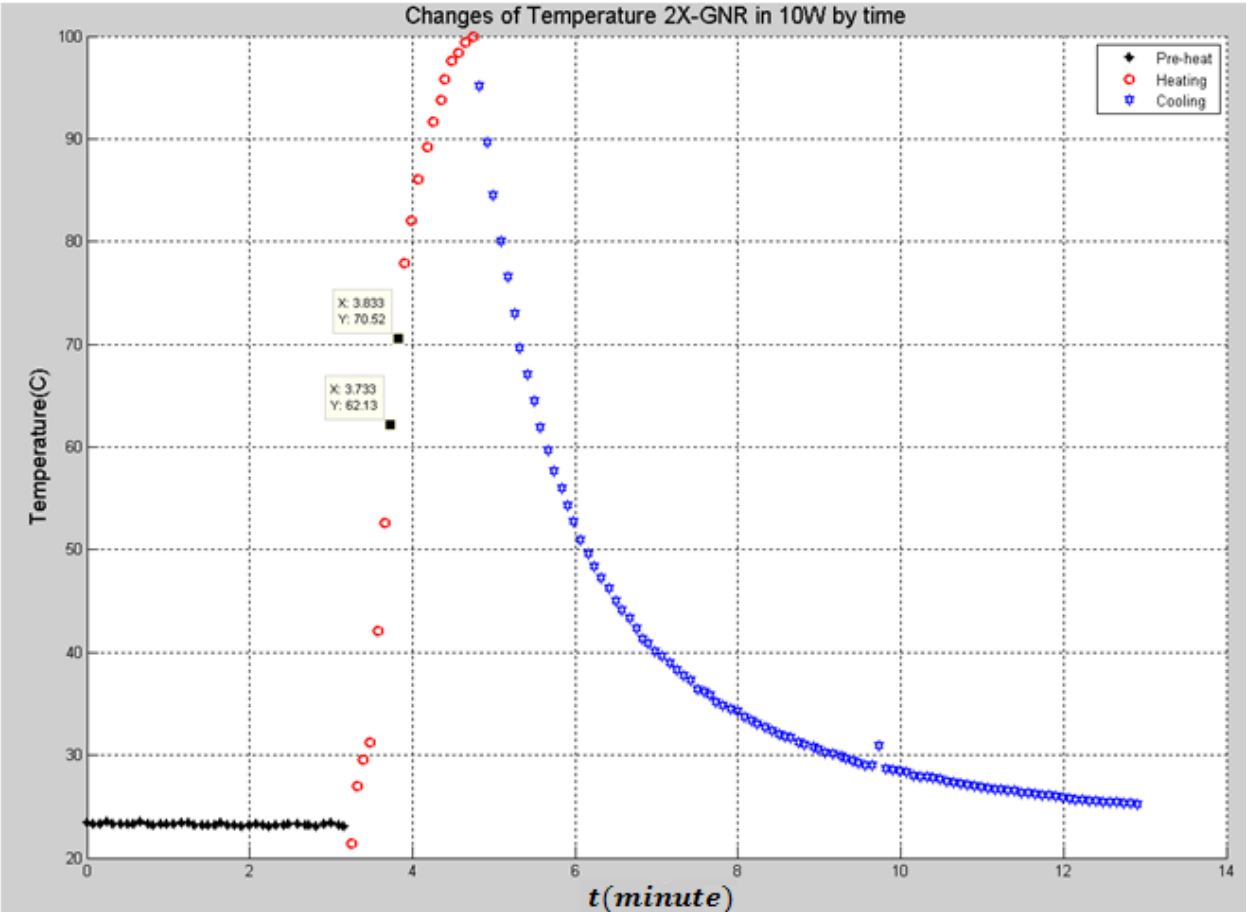

Figure 3.15 Variation of Temperature with time for a laser exposure of almost 2 minutes

Fig.3.3 and Fig.3.4 show the location of fluoroptic thermometer and the location that the RF data were collected. It is noted that the temperature was not measured at the same location as the OA pressure signal during the experiments. Therefore, in T-t graph the X axis does not represent the temperature of the last quarter of phantom. This is an important point as the signal of analysis region is location 13 mm away from where these temperatures were measured.

Therefore, the temperatures were measured, cannot be directly related the OA data. However qualitative changes in the temperature are expected to be symmetric about the center of the phantom.

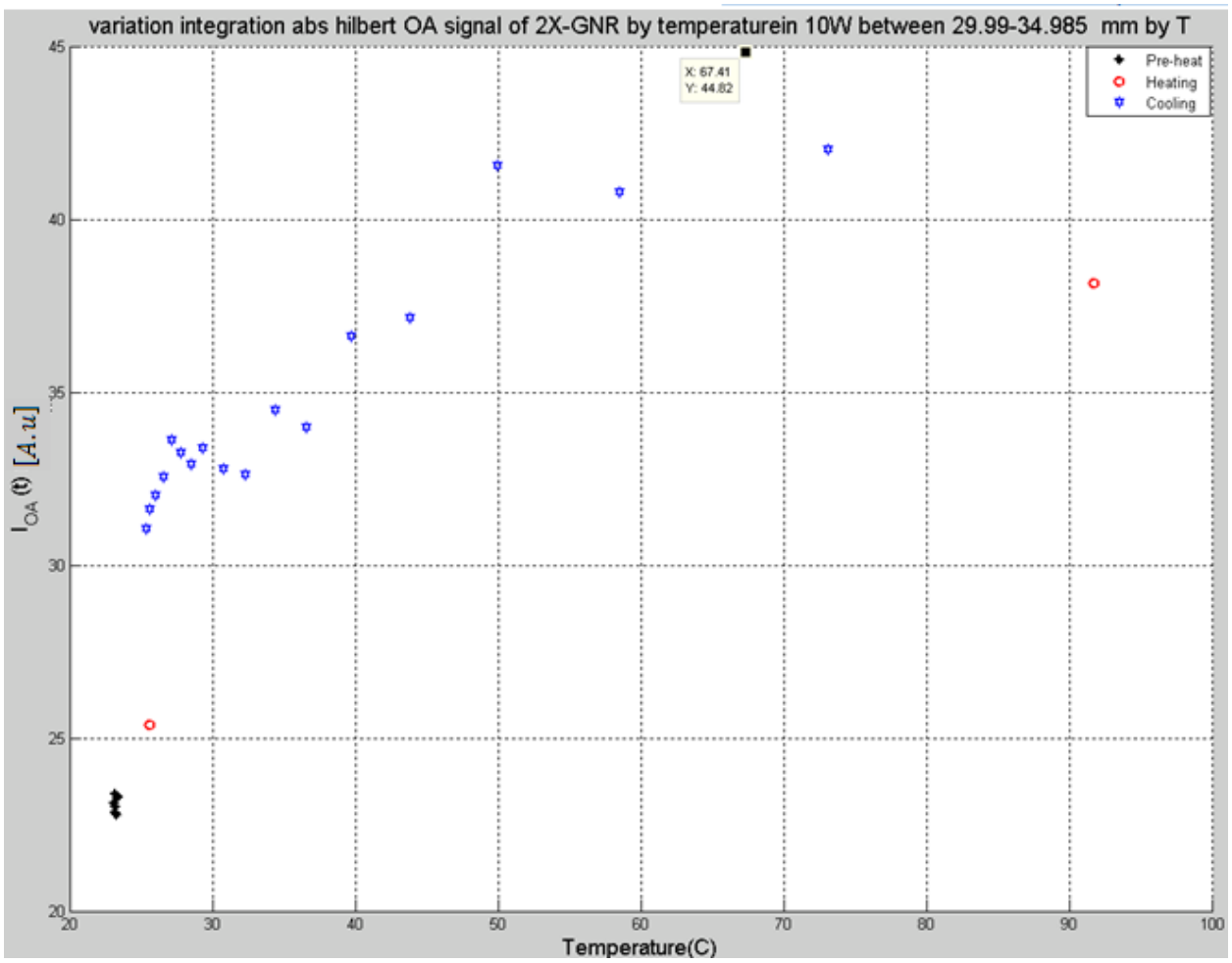

Figure 3.16 Variation of OA signal with temperature changes

3.6 Ranking Method

After visual inspection of the eighteen sets of results, some items were checked to rank the results. Ranking was based on the linearity of the $I_{OA}(T)$ graphs. It means, after turning the laser on, the temperature increases and this increase corresponds to an ascending hypothetical line on the $I_{OA}(T)$ graph. Also the temperature decrease corresponds t a hypothetical descending line. If these two ascending and descending lines of one set of experiments are corresponds to each other, set of experiment places at the first rank of linearity. If these lines are a little away due to each other, that set gets the next rank. Ranking is based on the amount of the distance of the two lines due to each other. Therefore the Table 4.1 was made based on this assumption of linearity.

Chapter 4

Results

Eighteen sets of experiments were carried out using four series of different dilutions of GNRs exposed to four different powers for each set of dilution, as described in the methods section.

In all eighteen cases of temperature variation versus time, a common trend was observed.

Ranking of experiments was based on the linearity of the $I_{OA} - T$ diagrams. According to these criteria a consistency table was made (Table 4.1).

As was mentioned in section 3.4.1 before and after laser heating, two images were taken of the region of interest (ROI). The image shows an OA image of the ROI of the phantom of the phantom before laser heating. (Fig.4.1) shows image of the ROI before heating on the phantom which will be explained in next chapter.

The data of experiments in different powers and dilutions according to table 3.1 for the three stages of preheat, heating and cooling, will be presented in (Fig.4.2) to (Fig.4.19) as ***a)*** a change of temperature with time, $T(t)$, ***b)*** a change of integrerated OA signal with time, $I_{OA}(t)$, ***c)*** the change of OA signal with temperature, $I_{OA}(T)$.

In all of the eighteen set of the figures (Fig.4.2) to (Fig.4.19) in part ***(a)***, all the temperatures measured by the fluoroptic thermometer, which it's sensor was 2 mm away of

scanning point. It is necessary to mention that this temperature is different by the analyzing area which is loated in the last quarter region of the phantom.

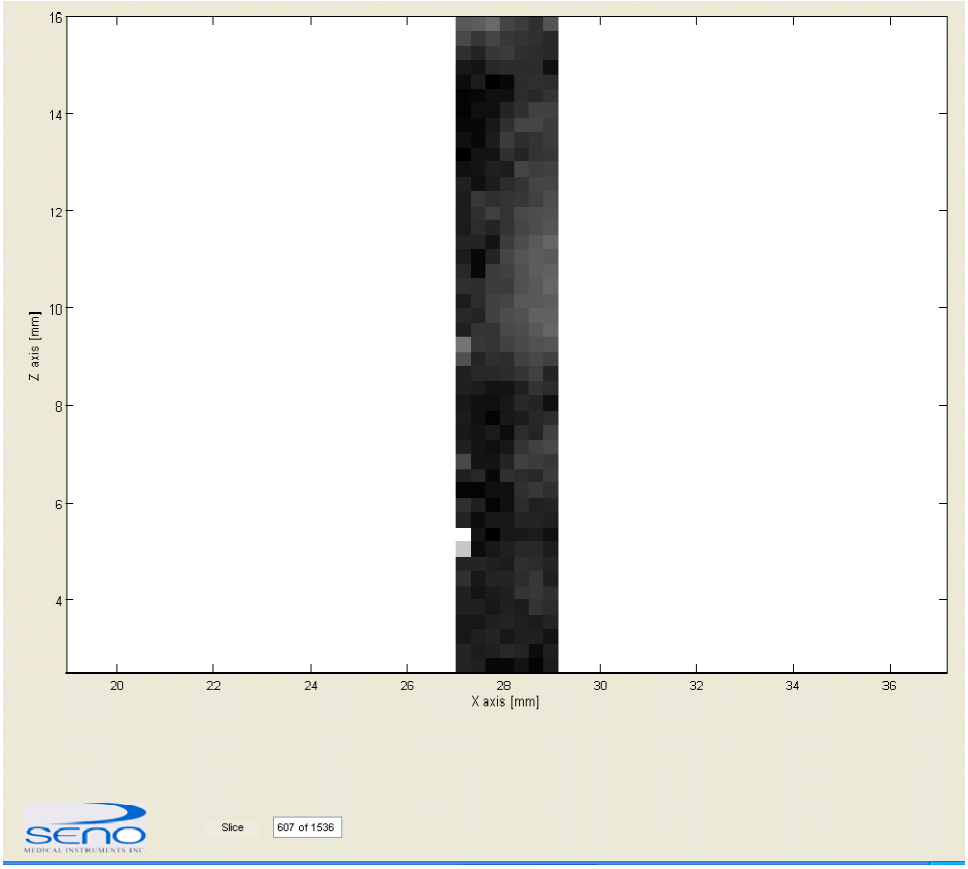

Figure 4.1 Image in the XZ plane before laser heating (2 × dilution phantom)

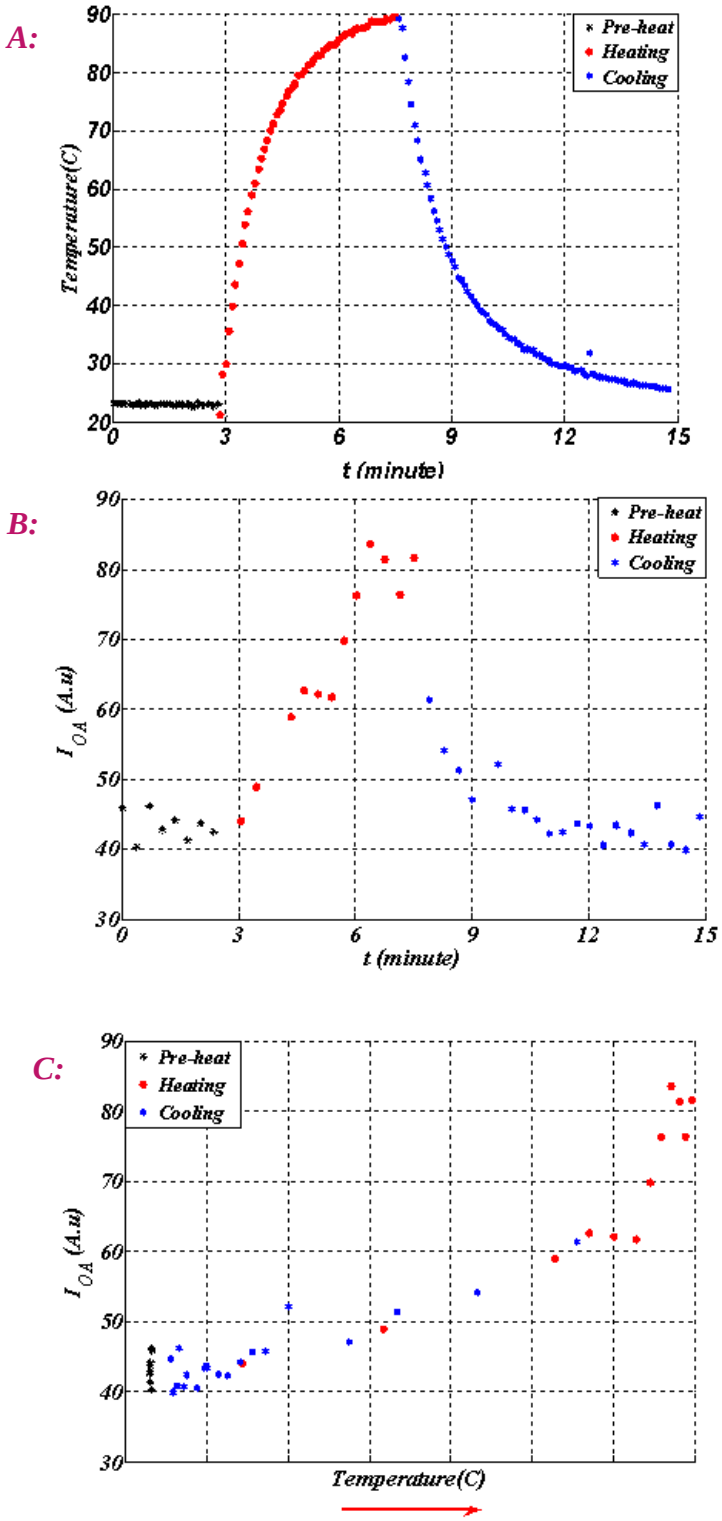

Figure 4.2 A)Changes of temperature with time, B) Variation of the OA signal with time at the locations specified in Chapter3 (Fig3.4), C) Variation of OA signal recorded as a function of temperature for the same experiment, for the5X-GNR phantom heated exposure.

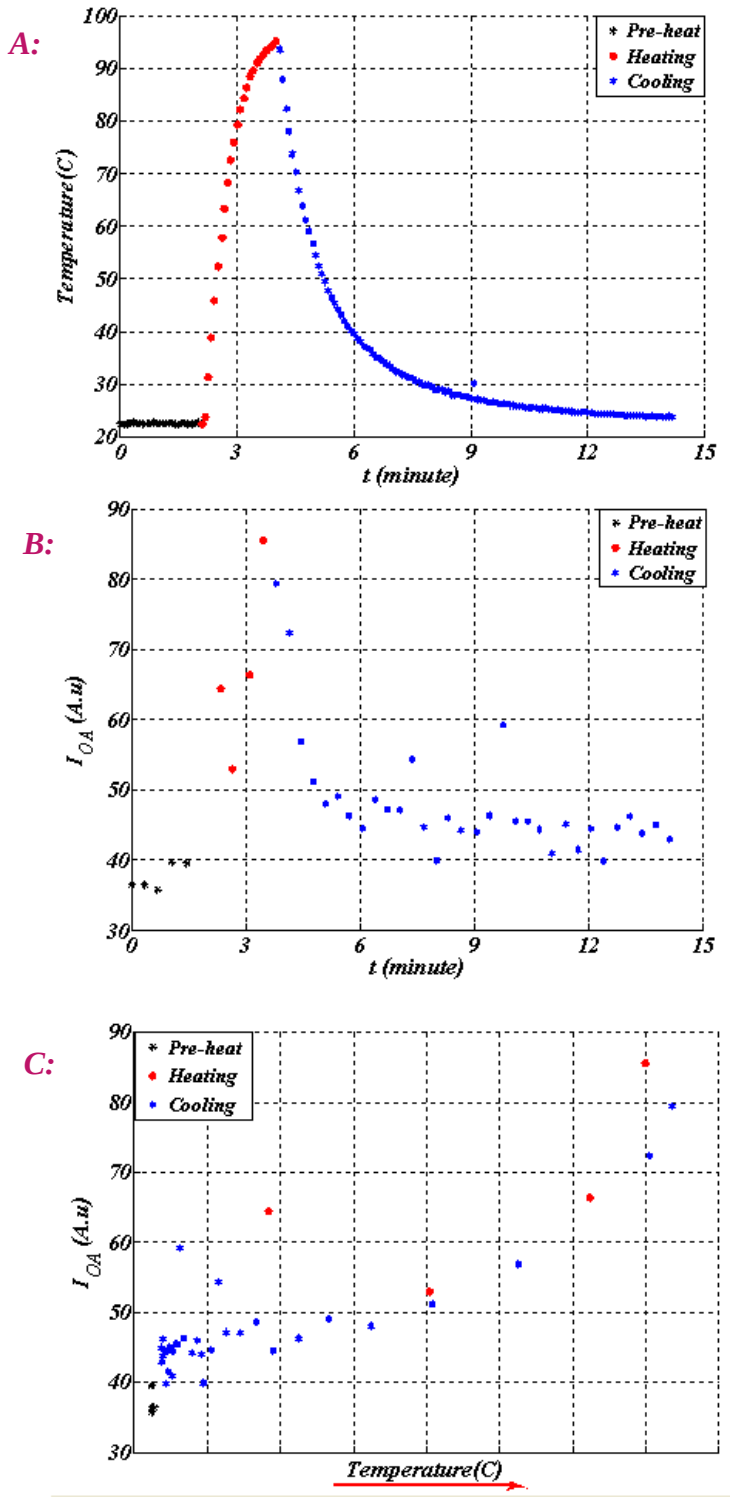

Figure 4.3 A)Changes of temperature with time, B) Variation of the OA signal with time at the locations specified in Chapter3 (Fig3.4), C) Variation of OA signal recorded as a function of temperature for the same experiment, for the 5X-GNR phantom heated with 12W laser exposure.

A:

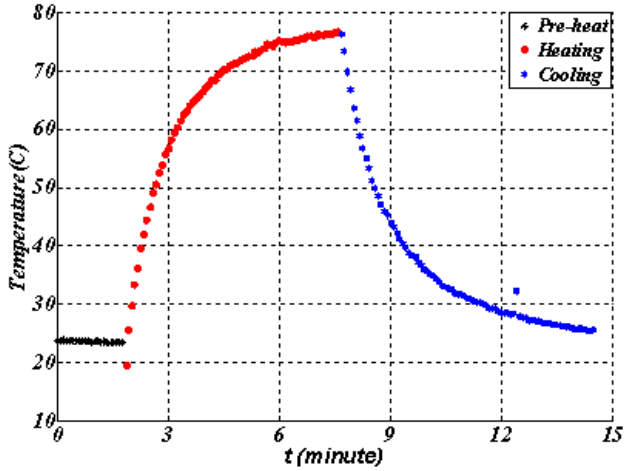

B:

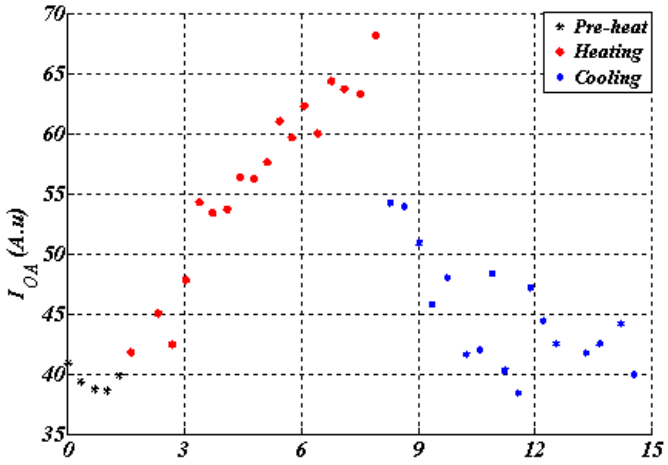

C:

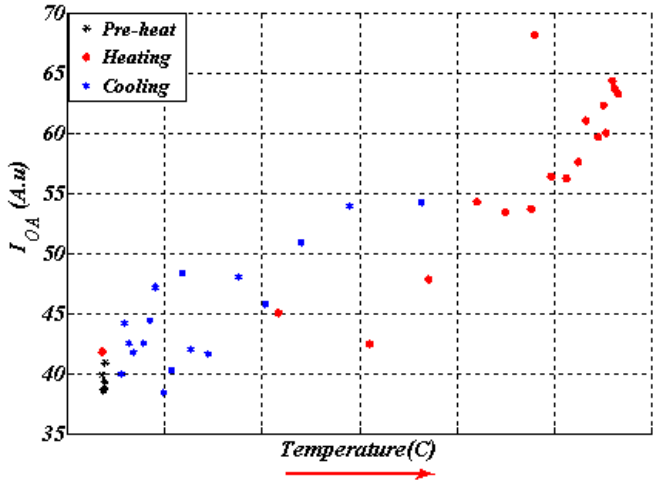

Figure 4.4 A)Changes of temperature with time, B) Variation of the OA signal with time at the locations specified in Chapter3 (Fig3.4), C) Variation of OA signal recorded as a function of temperature for the same experiment, for the 5X-GNR phantom heat phantom heated with a 8W laser exposure.

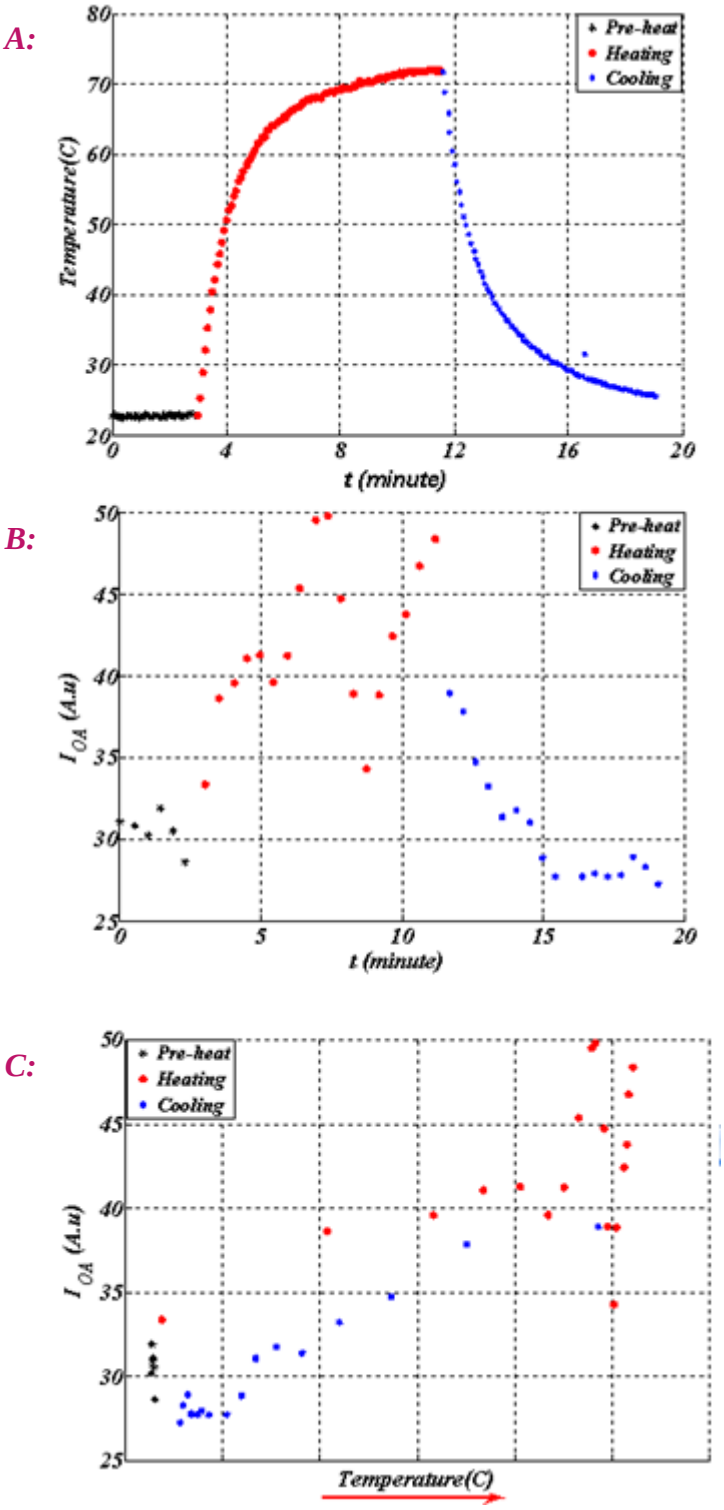

Figure 4.5 A)Changes of temperature with time, B) Variation of the OA signal with time at the locations specified in Chapter3 (Fig3.4), C) Variation of OA signal recorded as a function of temperature for the same experiment, for the 2X-GNR phantom heated with a 3W laser exposure.

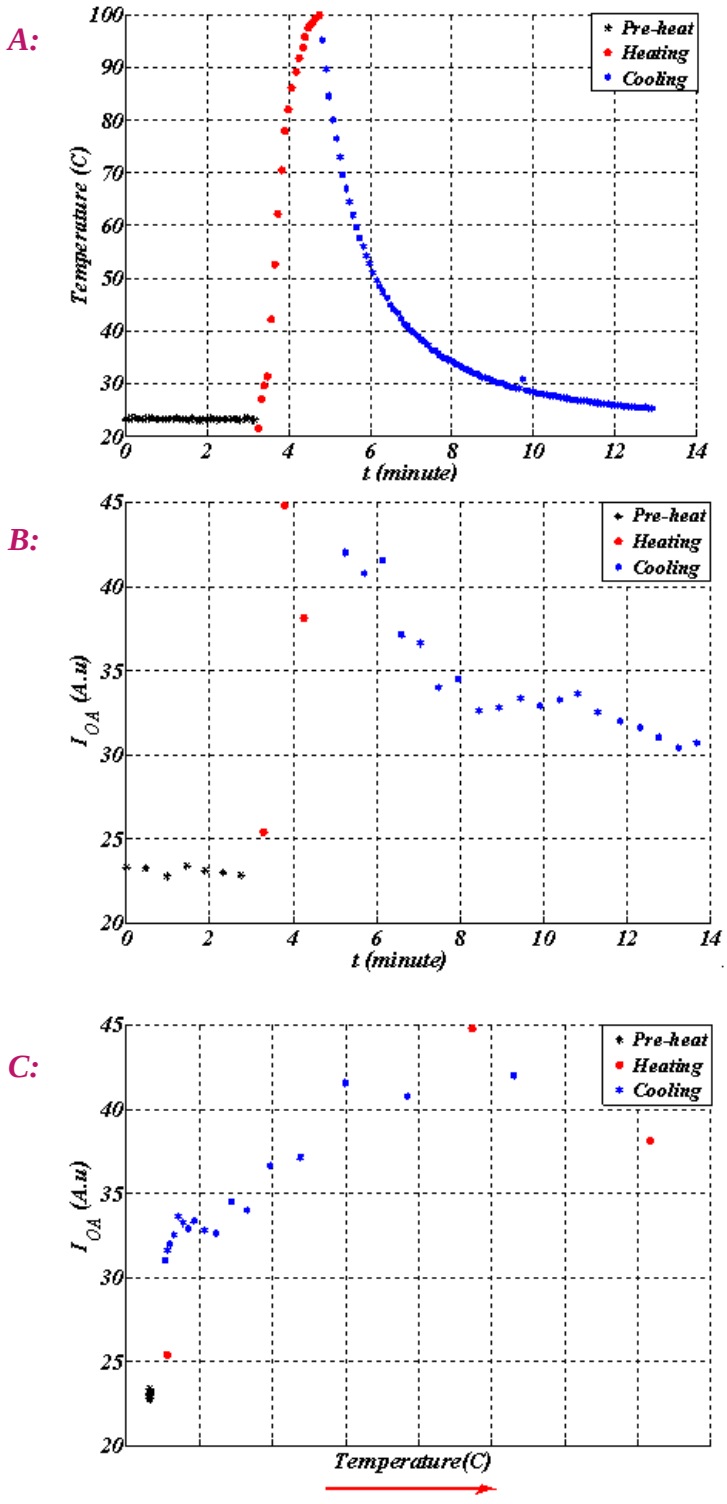

Figure 4.6 A)Changes of temperature with time, B) Variation of the OA signal with time at the locations specified in Chapter3 (Fig3.4), C) Variation of OA signal recorded as a function of temperature for the same experiment, for the 2X-GNR phantom heated with a 10W laser exposure.

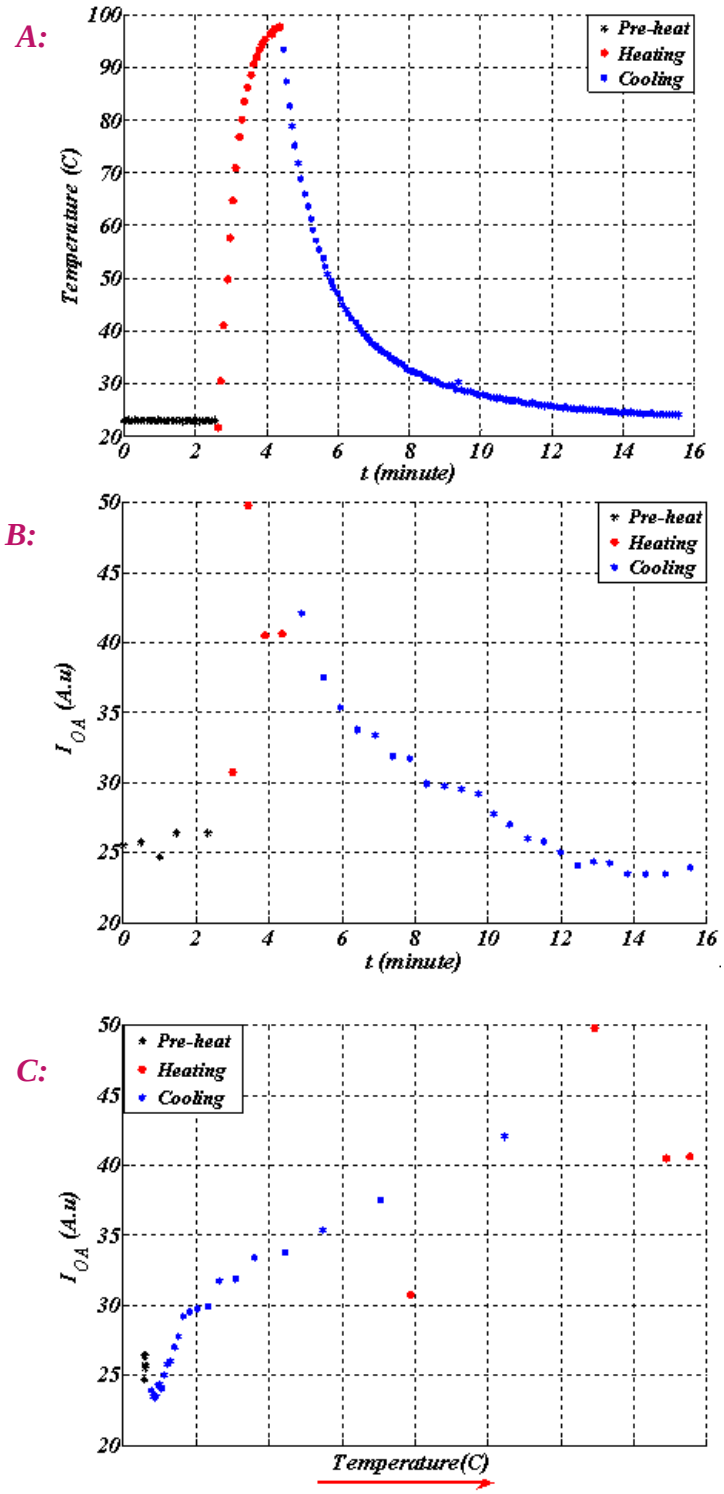

Figure 4.7 A)Changes of temperature with time, B) Variation of the OA signal with time at the locations specified in Chapter3 (Fig3.4), C) Variation of OA signal recorded as a function of temperature for the same experiment, for the 2X-GNR phantom heated with a 8W laser exposure.

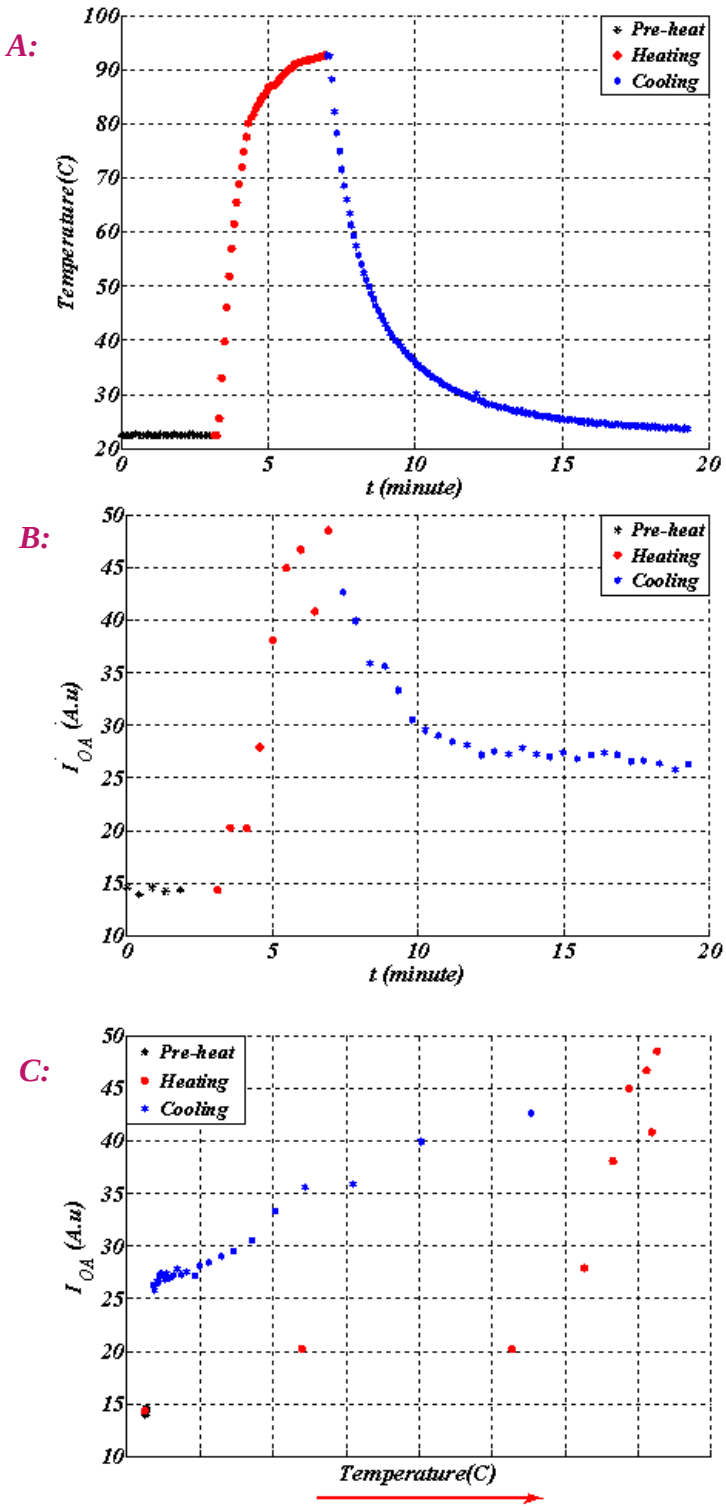

Figure 4.8 A)Changes of temperature with time, B) Variation of the OA signal with time at the locations specified in Chapter3 (Fig3.4), C) Variation of OA signal recorded as a function of temperature for the same experiment, for the 2X-GNR phantom heated with a 5W laser exposure.

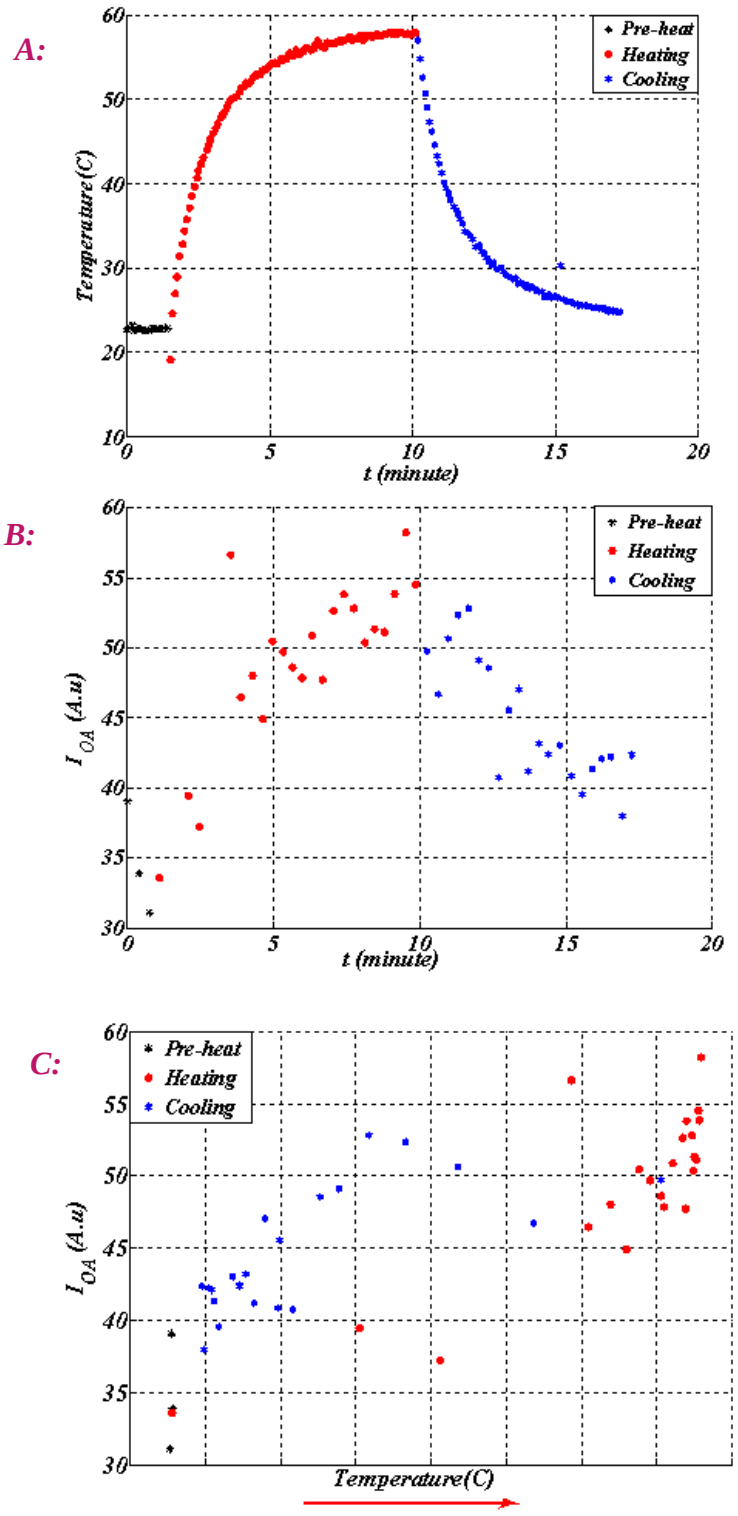

Figure 4.9 A)Changes of temperature with time, B) Variation of the OA signal with time at the locations specified in Chapter3 (Fig3.4), C) Variation of OA signal recorded as a function of temperature for the same experiment, for the 5X-GNR phantom heat heated with a 5W laser exposure.

A:

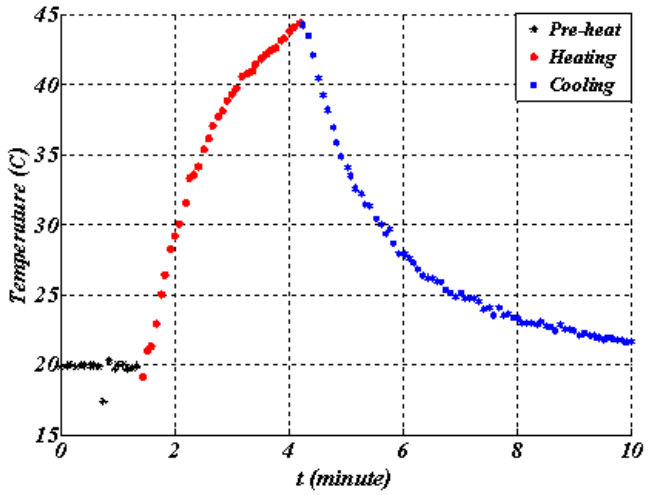

B:

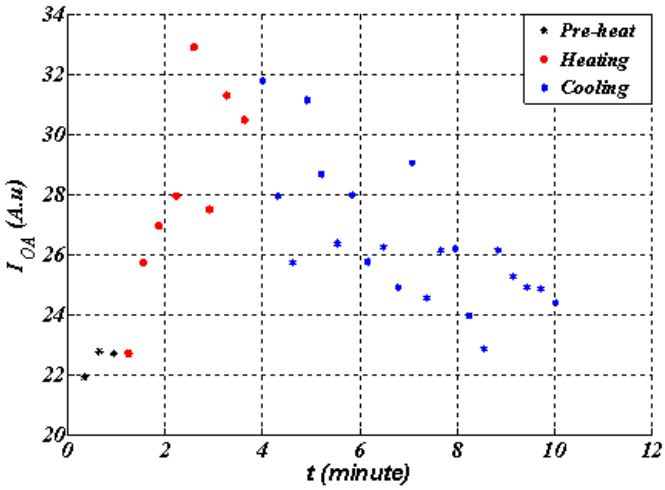

C:

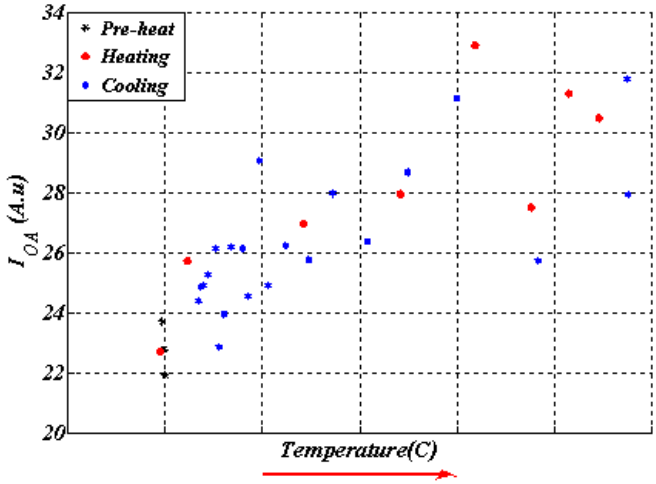

Figure 4.10 A)Changes of temperature with time, B) Variation of the OA signal with time at the locations specified in Chapter3 (Fig3.4), C) Variation of OA signal recorded as a function of temperature for the same experiment, for the 4X-GNR phantom heated with a 2.5W laser exposure.

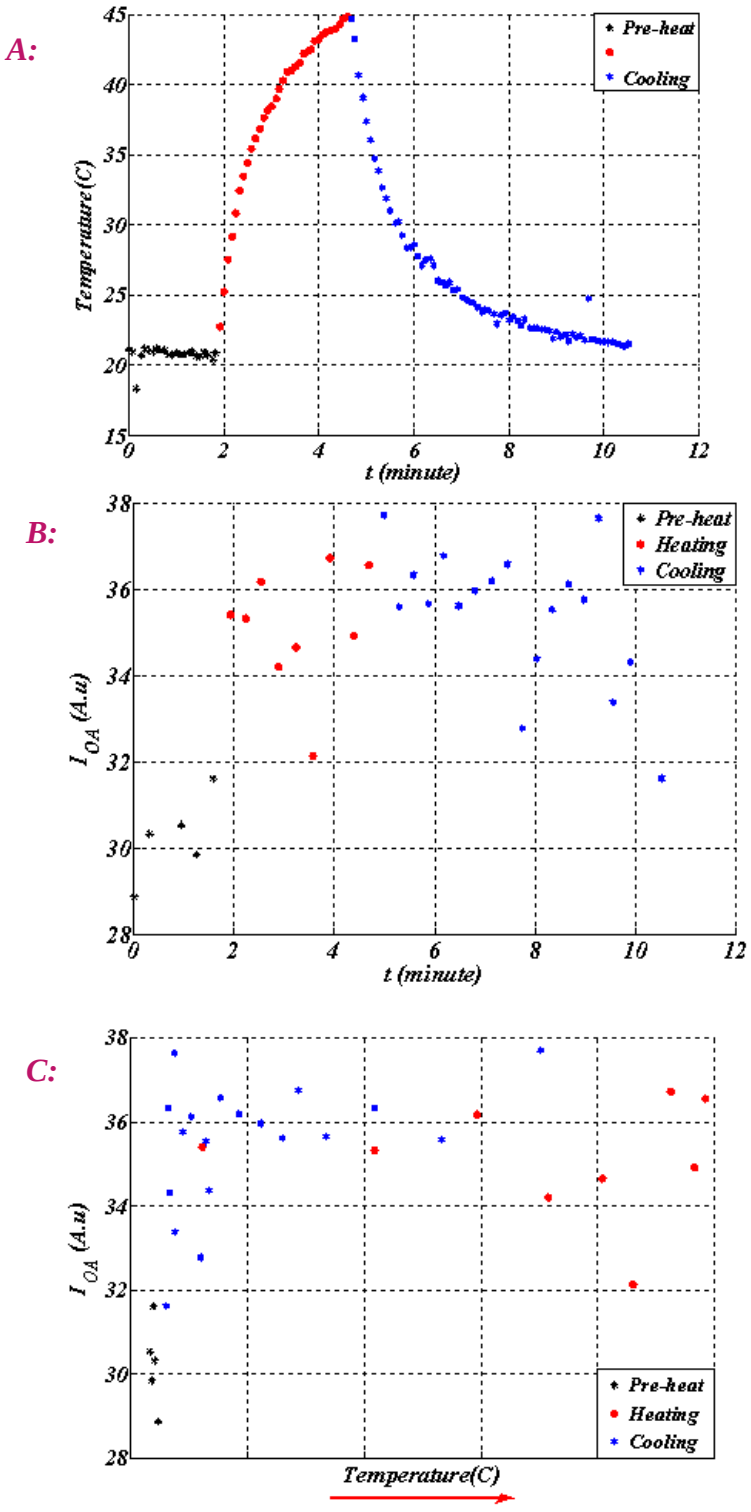

Figure 4.11 A)Changes of temperature with time, B) Variation of the OA signal with time at the locations specified in Chapter3 (Fig3.4), C) Variation of OA signal recorded as a function of temperature for the same experiment, for the 4X-GNR phantom heated with a 2W laser exposure.

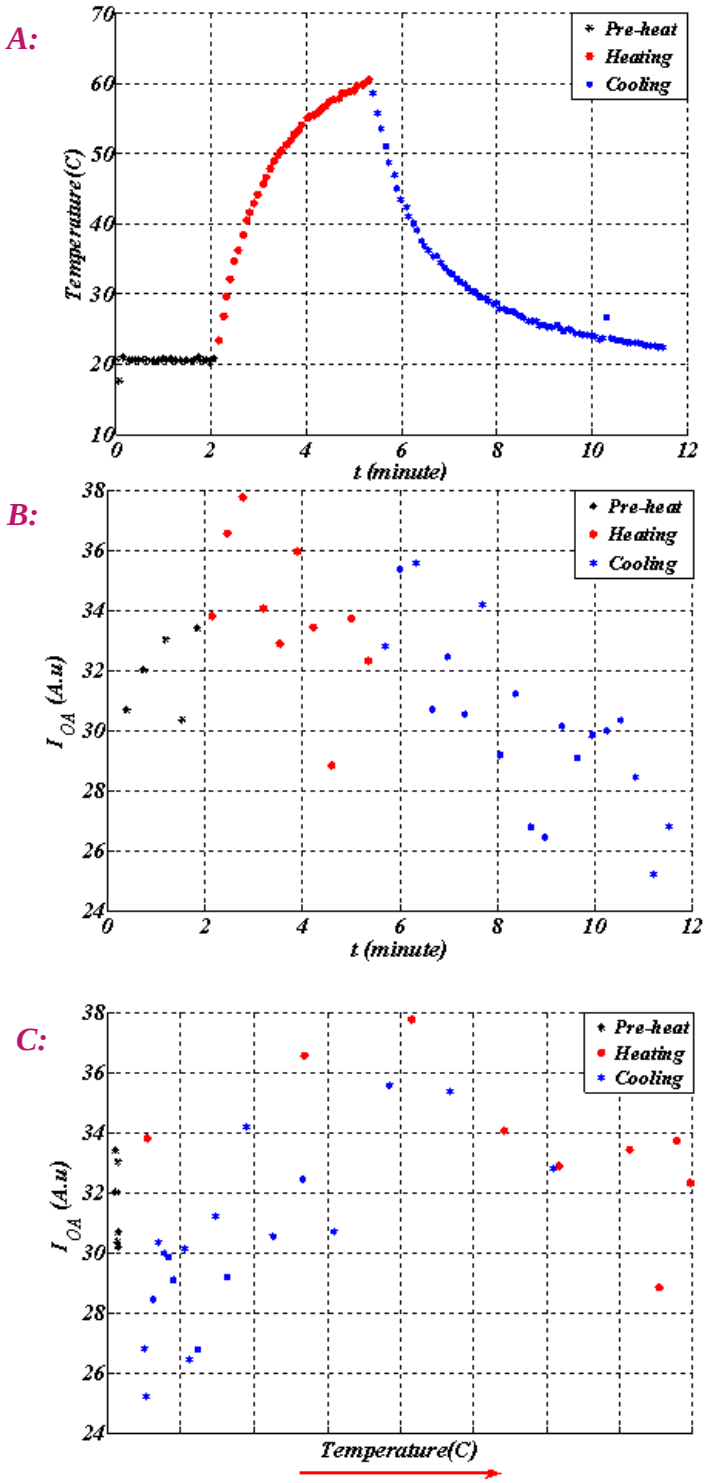

Figure 4.12 A)Changes of temperature with time, B) Variation of the OA signal with time at the locations specified in Chapter3 (Fig3.4), C) Variation of OA signal recorded as a function of temperature for the same experiment, for the 4X-GNR phantom heated with a 4W laser exposure.

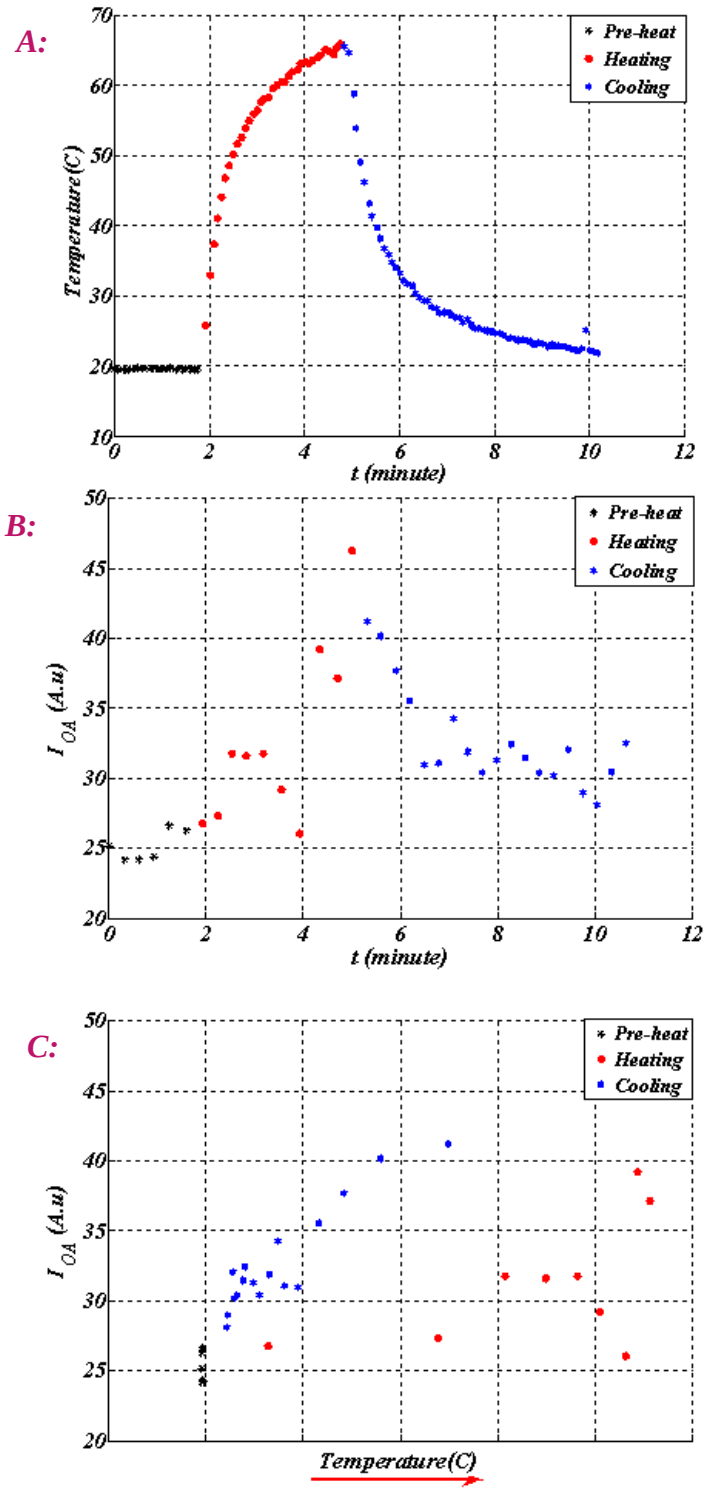

Figure 4.13 A)Changes of temperature with time, B) Variation of the OA signal with time at the locations specified in Chapter3 (Fig3.4), C) Variation of OA signal recorded as a function of temperature for the same experiment, for the 4X-GNR phantom heated with a 3.5W laser exposure.

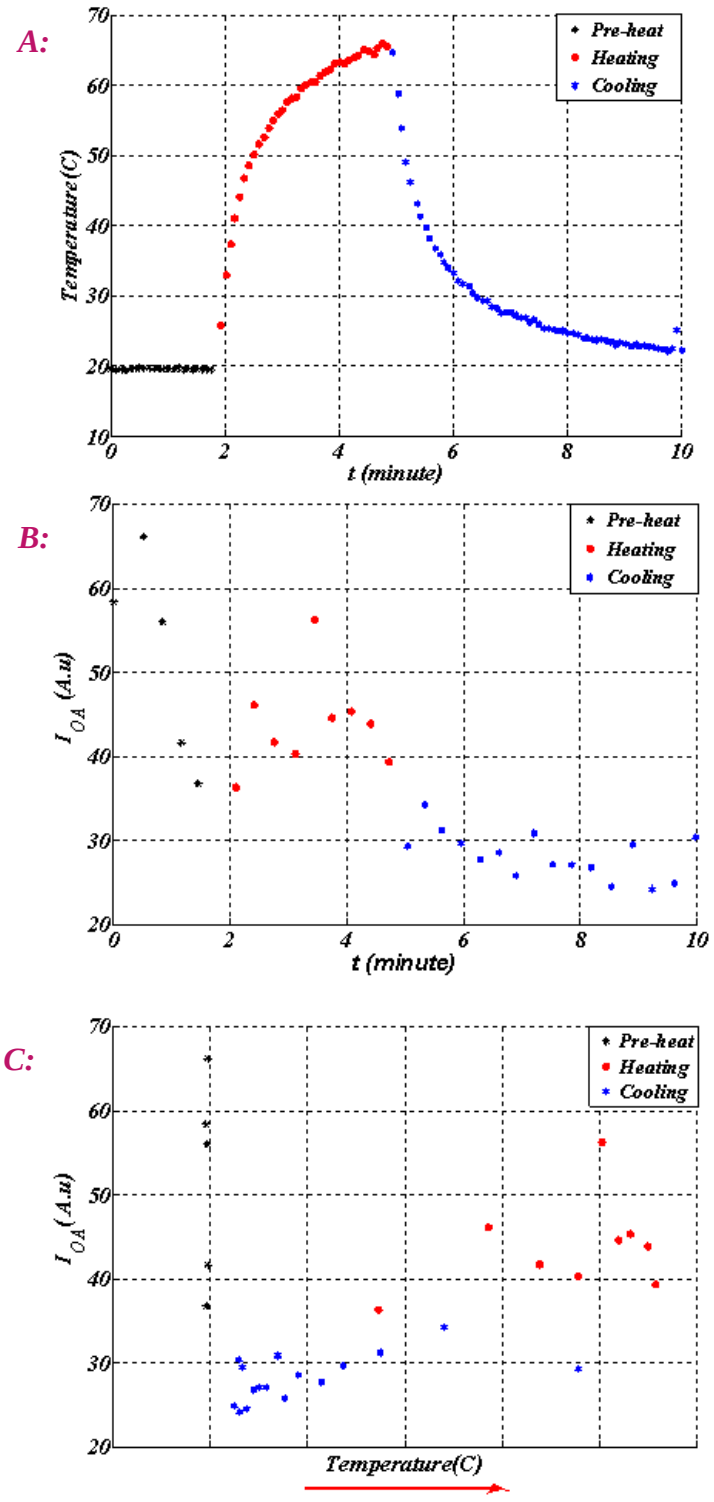

Figure 4.14 A)Changes of temperature with time, B) Variation of the OA signal with time at the locations specified in Chapter3 (Fig3.4), C) Variation of OA signal recorded as a function of temperature for the same experiment, for the 4X-GNR phantom heated with a 3W laser exposure.

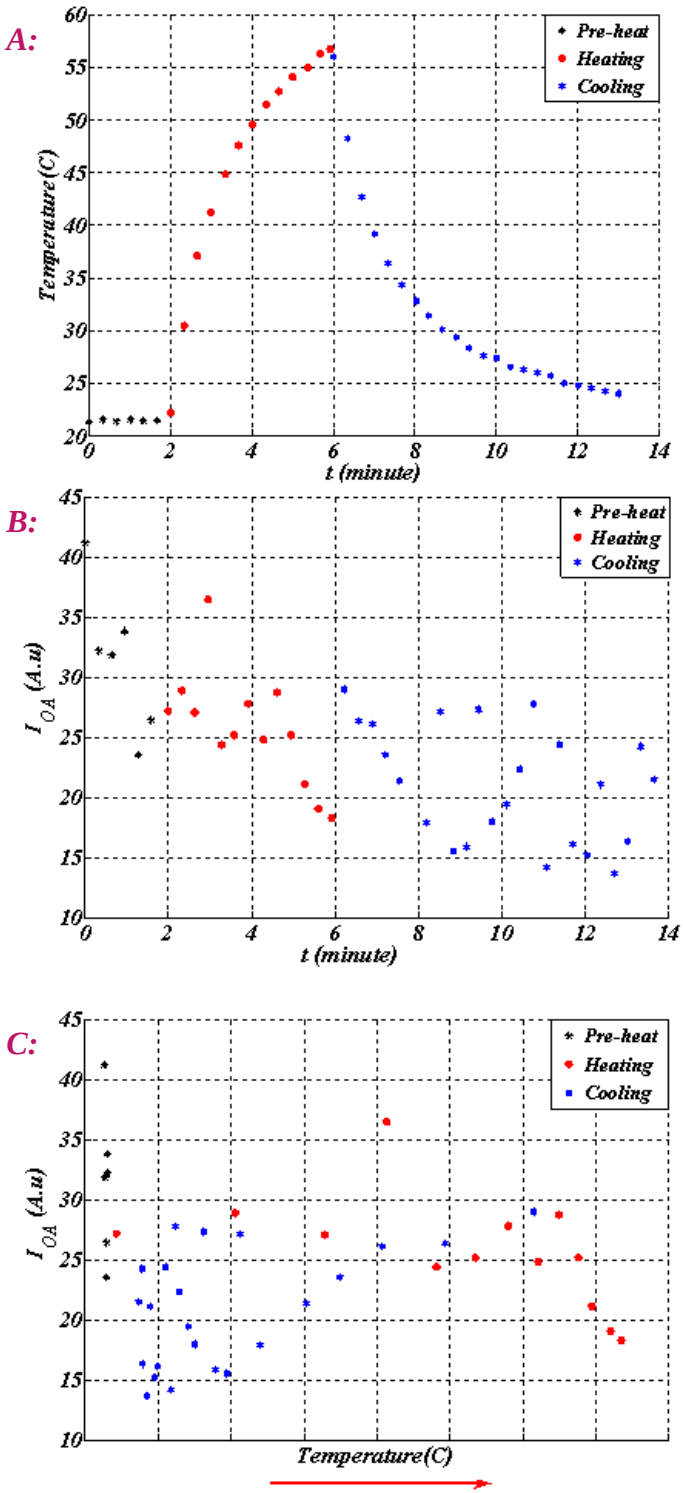

Figure 4.15 A)Changes of temperature with time, B) Variation of the OA signal with time at the locations specified in Chapter3 (Fig3.4), C) Variation of OA signal recorded as a function of temperature for the same experiment, for the 6X-GNR phantom heated with a 4W laser exposure.

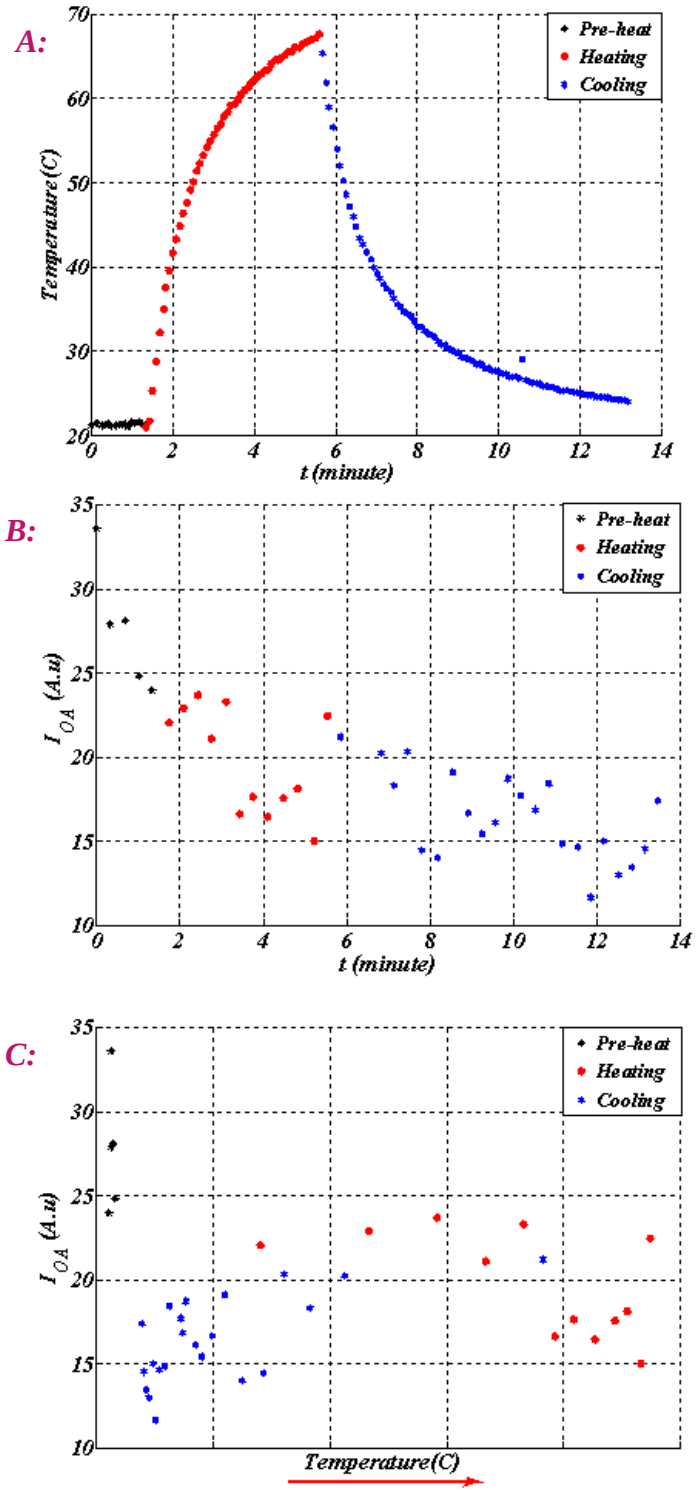

Figure 4.16 A)Changes of temperature with time, B) Variation of the OA signal with time at the locations specified in Chapter3 (Fig3.4), C) Variation of OA signal recorded as a function of temperature for the same experiment, for the 6X-GNR phantom heated with a 5W laser exposure.

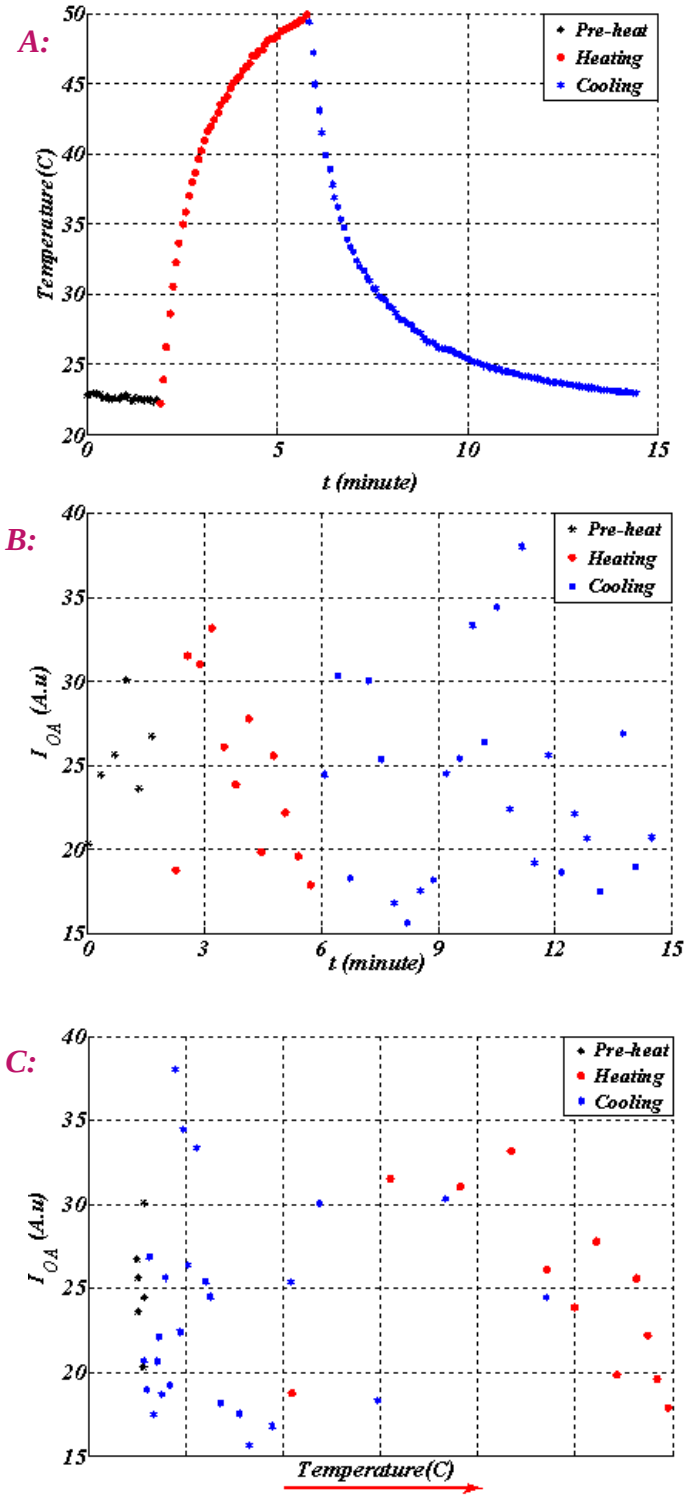

Figure 4.17 A)Changes of temperature with time, B) Variation of the OA signal with time at the locations specified in Chapter3 (Fig3.4), C) Variation of OA signal recorded as a function of temperature for the same experiment, for the 6X-GNR phantom heated with a 2.5W laser exposure.

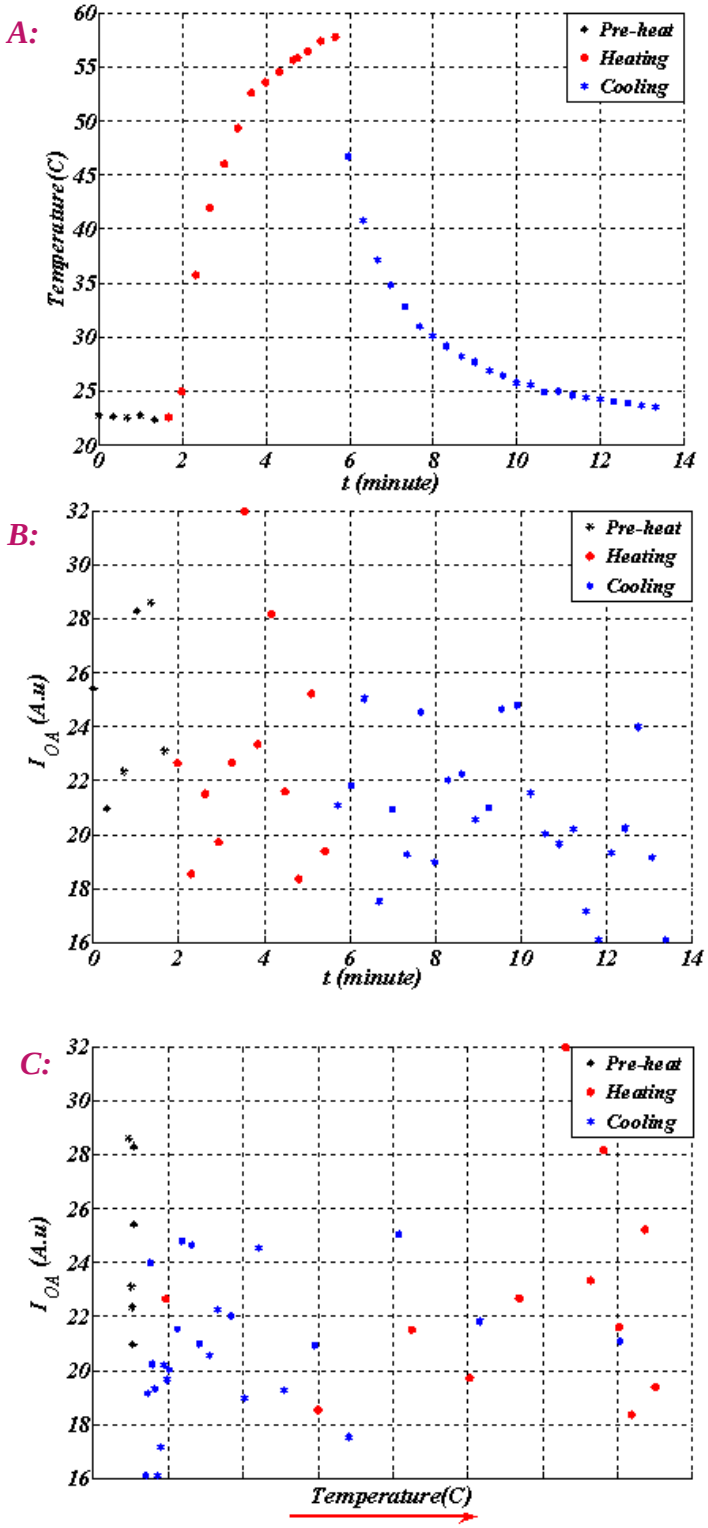

Figure 4.18 A)Changes of temperature with time, B) Variation of the OA signal with time at the locations specified in Chapter3 (Fig3.4), C) Variation of OA signal recorded as a function of temperature for the same experiment, for the 6X-GNR phantom heated with a 3.5W laser exposure.

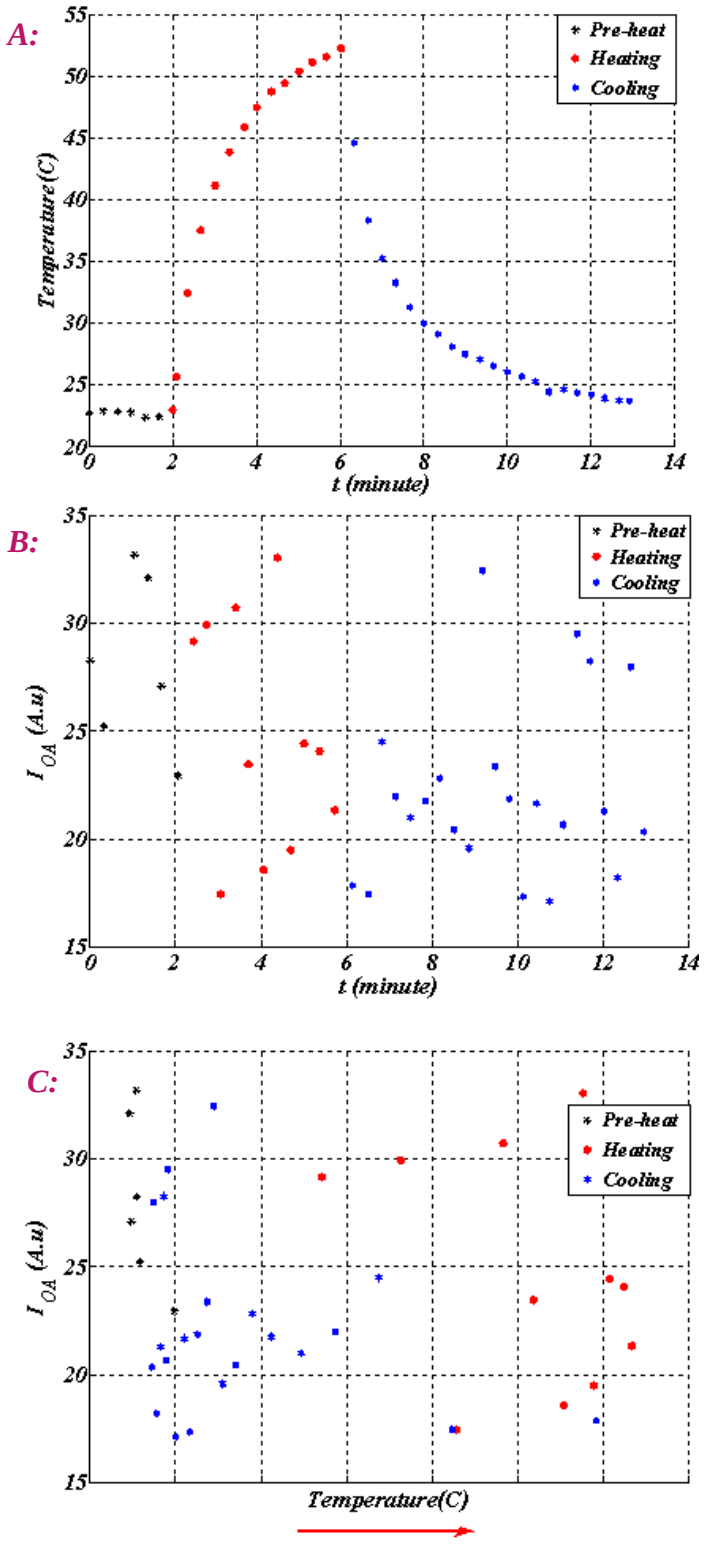

Figure 4.19 A)Changes of temperature with time, B) Variation of the OA signal with time at the locations specified in Chapter3 (Fig3.4), C) Variation of OA signal recorded as a function of temperature for the same experiment, for the 6X-GNR phantom heated with a 3W laser exposure.

Consistency Ranking of experiment data						
Ranking	Dilution	Power(W)	Max.Temp.(°C)	Ave.	Power/Dilution	Figures
1	5X	10	89.53	16	2	4-2
2	5X	12	95.21	16	2.4	4-3
3	5X	8	76.68	16	1.6	4-4
4	2X	3	72.13	64	1.5	4-5
5	2X	10	99.91	64	5	4-6
6	2X	8	97.73	64	4	4-7
7	2X	5	92.61	64	2.5	4-8
8	5X	5	58.01	16	1	4-9
9	4X	2.5	44.36	8	0.625	4-10
10	4X	2	44.84	8	0.5	4-11
11	4X	4	60.52	8	1	4-12
12	4X	3.5	64.03	8	0.875	4-13
13	4X	3	65.96	8	0.75	4-14
14	6X	4	56.77	8	0.667	4-15
15	6X	5	67.68	8	0.833	4-16
16	6X	2.5	49.95	8	0.4167	4-17
17	6X	3.5	59.24	8	0.583	4-18
18	6X	3	52.27	8	0.5	4-19

Table 4.1 Table of consistency ranking using the linearity of the diagrams of OA signal vs Temperature as a criterion

In summary of the first 6 of Table 4.1 graphs showing the variations of the I_{OA} as a function of increasing temperature are shown in (Fig.4.21).

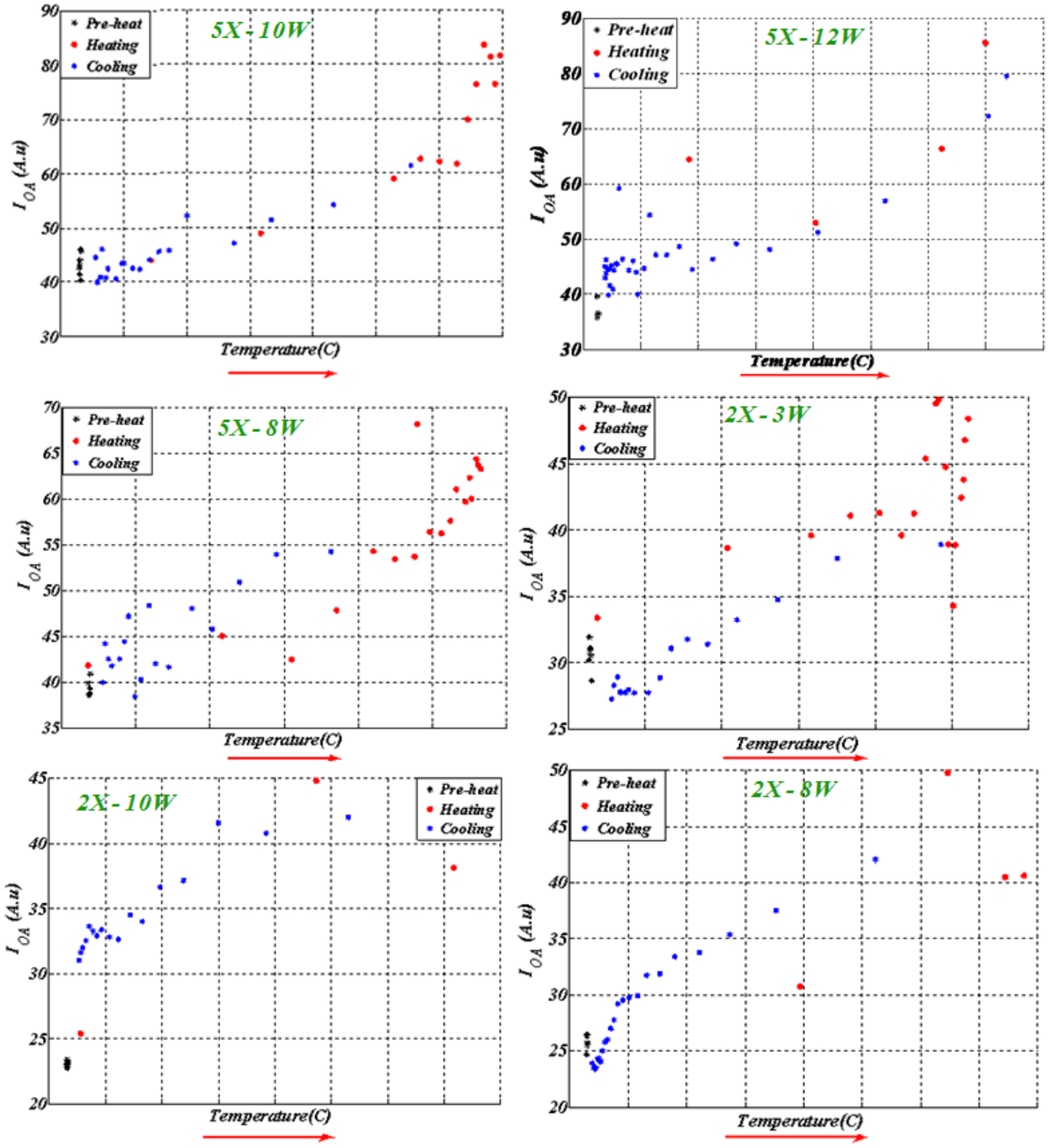

Figure 4.21 The first six (based on Table 4.1)plots of OA signal by temperature.

All of the raw RF data during heating and cooling are shown in appendix A

Chapter 5

Discussion

This thesis presents a method of using gold nanorods (GNRs) for photothermal therapy. GNRs are used to increase heating and as a contrast agent for imaging. Eighteen sets of experiments were carried out with four different types of GNR dilutions and various laser powers. In all of the eighteen sets the plots of temperature vs. time were recorded: before, during and after laser heating. The result shows that the use of GNR enhances both the contrast between phantom material with and without GNRs and also improves the photothermal therapy temperature efficiency and tracking.

The selected range for analyzing the optoacoustic data was in the region of the phantom closest to the OA laser. The optoacoustic signal should be maximized in this region due to the exponential nature of the OA laser fluence with depth. At greater depths the light intensity decreases in relation to the absorption coefficient of the phantom material [36].

The location of the RF measurement is the middle of X direction of the phantom and the fluoroptic thermometer is almost 2 mm further in the X direction. The last quarter of the phantom in the Y direction was approximately 30 to 35 mm from the transducer, while the location of the fluoroptic thermometer is estimated to be 27 mm from transducer (Fig.3.3) and (Fig.3.4). As the tip of the heating fiber was pointed to the center of the top surface of the phantom, then the temperature of the phantom at 23 mm from the transducer should have the same temperature at 27 mm. Therefore, it can be concluded by passing a hypothetical circle with

a 2 mm radius is drawn around the center point of the phantom which passes the points of 23mm and 27 mm distance from the transducer has the same temperature (Fig.3-4). Therefore it is assumed that the scanning point and the fluoroptic thermometer have the same temperature.

Heat transfer produces a temperature gradient from the source to the analyzed area. The temperature gradient can potentially vary strongly with distance [37, 38]. Also the phantom is surrounded with water that causes to cool down the phantom. Since the water cools the phantom near the boundaries, the temperature at the measurement location and at the boundary is probably not linearly related. If, on the other hand, the temperature at these locations are linearly related, then collinearity can be used as a criteria. Hence, all of the diagrams which present the variation I_{OA} vs. T do not indicate the temperature profile at the location that the OA signal was collected, but are likely representative of the general trends of temperature profiles all the locations that the OA signal was collected. For this reason, graphs of I_{OA} (T) were presented without numerical values for temperature.

Table 4.1 shows that lowest maximum temperature is 72°C among the first seven of data sets. As the temperature increases, the two types of the diagrams *T-t,* $I_{OA}(t)$, have a steeper slope. Signal averaging decreases the OA signal noise and therefore it is anticipated that it is related to increasing the SNR.

Table 4.1 illustrates that, GNRs phantoms with factors of two and five dilution, led to better results based on the linearity criteria. Increasing power also lead to better results based on the linearity criteria. However, range of factor four dilutions which have lower dilution of GNRs did not follow the same linearity criteria.

In table 4.1 it is apparent that the ratio of thermal laser power to the dilution of the GNRs solution was a major determinant in consistency of the results. When this ratio is greater than 1.5, experiments show good linearity between the OA signal and temperature. High power and less dilution of GNR have the most major role for obtaining these results.

Experimental uncertainties may explain some of the variability of the results in the thesis. Some of these uncertainties include:

1- Gel phantom heterogeneity. This could cause some locations receiving a higher concentration of GNRs, higher absorption and therefore generating higher temperatures and stronger signals.

2- Heating laser alignment to the phantom surface may produce light reflection and therefore variable heating; it depends on the angle of the laser fiber with the top surface plane of the gel phantom.

3- The gel phantom was made of porcine skin. The threshold temperature for porcine skin coagulation is between 92 and 104°C [43]. Among 18 experiments, 4 had maximum temperatures of greater than 90°C, with two of them nearly 100°C. Of those 4 experiments and (2X - 10W) in Fig.(4-6) and (2X - 5W) in Fig.(4-8) produced results that are consisted with gel coagulation, but (2X - 10W) in Fig.(4-6) produced results that were not conclusive and (2X - 5W) in Fig.(4-8) produced results not to indicative of coagulation. Therefore, the role of coagulation in the findings is unclear.

4- Table 4-1 indicates that the dilution factor of GNRs has a significant role on the maximum temperature obtained. GNRs with high concentration (or less dilution), produce higher maximum temperatures. There was a limitation on the maximum temperature in order to

prevent of damage the thermal laser fiber. The maximum temperature should not exceed 100°C.This limitation did not allow an investigation of the relation between maximum temperature and dilution factor of GNRs consistently for all sets of experiments. This limitation affected two experiments (2X – 8W) in Fig. (4-7) and (2X – 10W) in Fig. (4-6). In these experiments the heating duration was less than the others.

By considering the heating laser power of the rank numbers 7, 8 and 15, which is 5W for all dilution factors of 2, 5, 6, it can be concluded that the dilution factor related to the rank.

Also the intensity of heating laser is another factor which affects the results. By referring the table 4.1, it can be observed that higher power helps to obtain better ranking results.

On the other hand, the ratio of power over the dilution factor correlated with rank. Table 4.1 shows that the power/dilution is equal to or greater than 1.5, for the top seven ranked experiments. The combination of higher power and greater nanorod concentration leads to higher temperatures and therefore greater changes in the optoacoustic singal. If gel coagulation would occur, this would likely lead to irreversible changes in the optoacoustic signal which would likely impact the ranking.

One of the consequences of photothermal therapy is increasing the OA signal amplitude with the temperature and changes in acoustic properties such as speed of sound and density. The sharp increase in temperature, especially more than 55 to 70 °C could lead to change in the Grüneisen coefficient. An increase in the Grüneisen coefficient can increase the OA signal. By observing the RF lines (A-scan) during heating (Fig.5.1) and cooling (Fig.5.2), it can be seen that OA signal increased during heating and decreased during cooling.

By increasing both the thermal laser power and concentration of GNR it can help to decrease the heating duration since the target temperature can be attained in a shorter time. Also in most cases $I_{OA}(T)$ increased during heating. Graphs have a steeper slope when higher power is used for the thermal laser irradiation and when higher concentration of GNRs are used due to the increased power deposition.

There is a possibility that as gel phantom was made of porcine skin some of the ingredients include fat. In fat tissue, as temperature increases the speed of sound and thermal expansion coefficient decrease [12, 27].

Figures (Fig.5.1) and (Fig.5.2) also show that the OA signal shifted towards the left during heating and shifted towards the right during cooling. In other words the peak of the OA signal moved closer to the transducer during heating and shifted further from the transducer during cooling. This suggests that changes occureed in the speed of sound of the phantom during the temperature increases. Optoacoustic thermal monitoring is based on temperature induced changes in the speed of sound and the volume expansion coefficient. Both speed of sound and the volume expansion coefficient have a nearly linear relationship with temperature range (Fig.4.21) [27].

The data were analyzed, primarily based on variation of the Hilbert transform of the optoacoustic signal as a function of temperature. We expected the integrated Hilbert OA signal to be linearly proportional to temperature. It was based on the assumption that there is no denaturation in pure gel and mixed by GNR gel. As it was mentioned in chapter 2, variation of optoacoustic signals during photothermal therapy for the gel phantom or GNR gel phantom

should remain linear. Therefore, the optoacoustic signal variation with temperature during heating and cooling should the same.

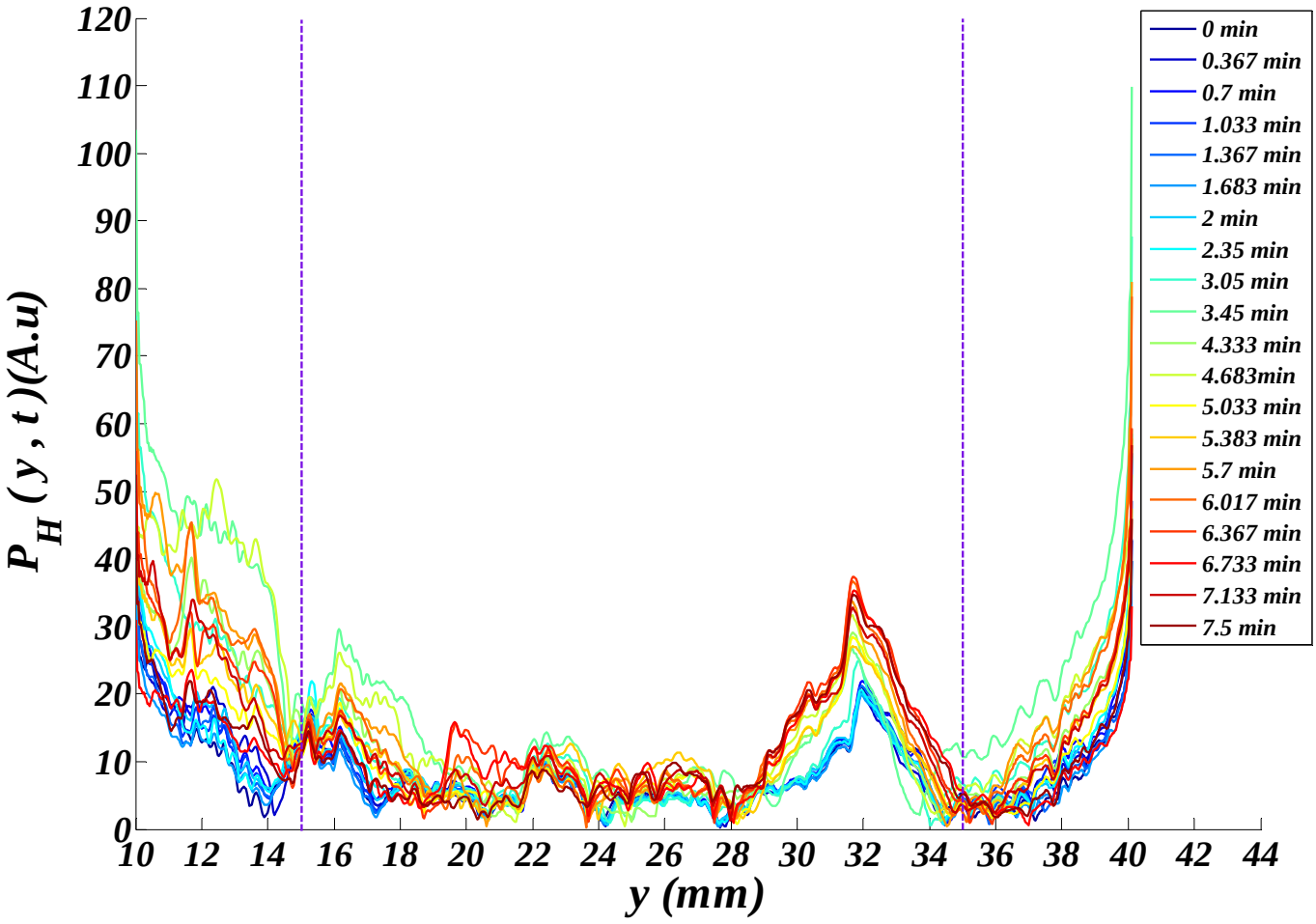

Figure 5.1 RF lines of 5X-GNR gel phantom during heating with 10W laser power. Legends show time after first RF data acquistion (before heating). The heating laser turned on at 2.317 minutes.

The legends of (Fig.5.1) show the time after first RF data acquisition (before heating). The laser turned on after 5 time data acquisition at 2.317 minutes. The turning off time of heating laser was the commencing point in cooling graph in (Fig 5.2).

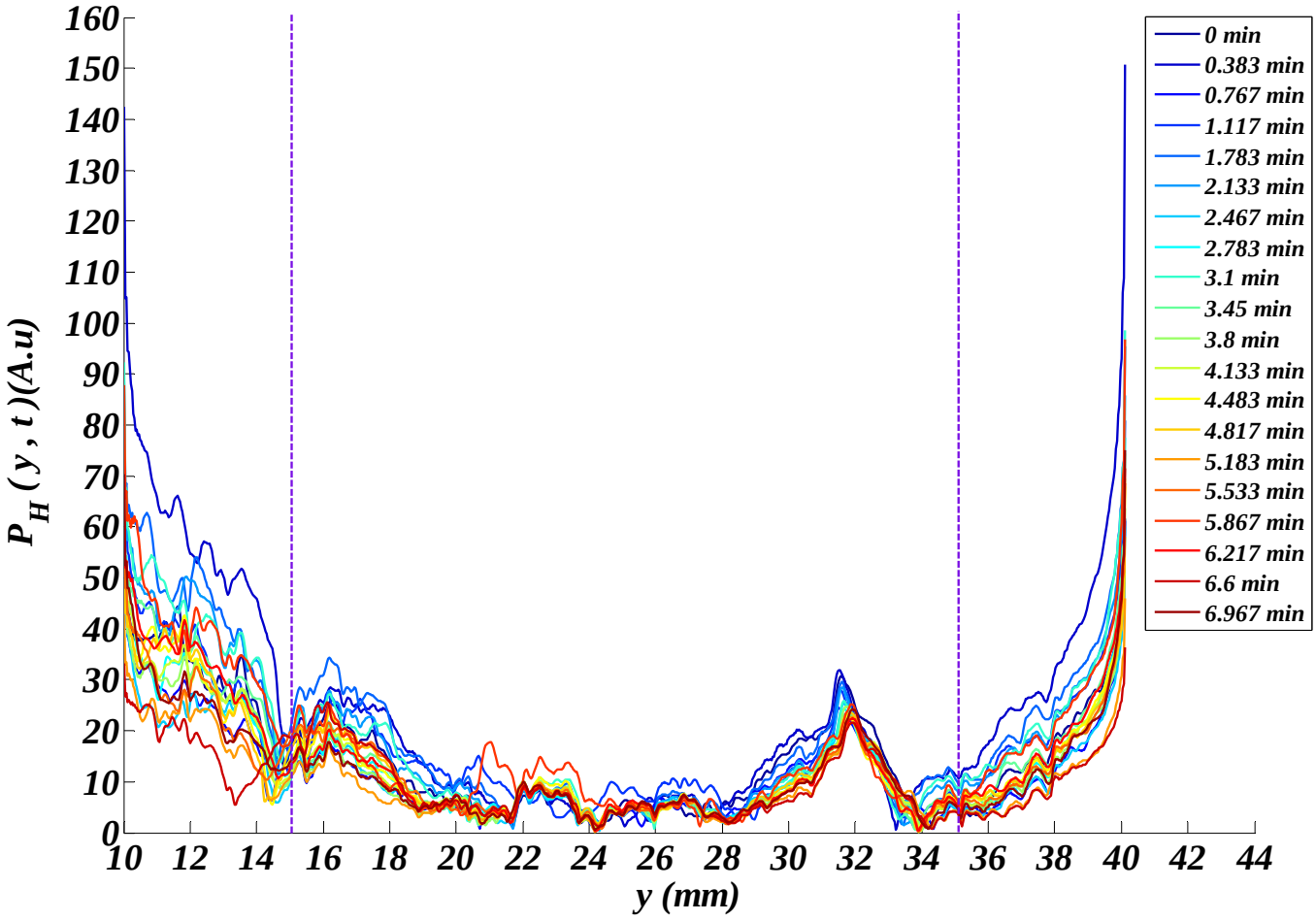

Figure 5.2 RF lines of 5X-GNR gel phantom during cooling with 10W laser power. Legends show the elasped time after turning off the heating laser.

It can be observed that in (Fig. 5.1) and (Fig. 5.2) in the region out-sided the phantom between (0 mm and 15mm) and (40 mm and 56.8 mm), the optoacoustic signal is proportional to temperature [44]. Water can produce an OA signal, and this is known to the temperature dependent. As heat transfers from the phantom to the surrounding area, heating the surrounding water, it may be the possible that these variations produced in the signal from the water ate related to this temperature increase.

Chapter 6

Conclusions and Future Work

6.1 Conclusions

In this thesis a real time and non- invasive technique for imaging and temperature monitoring during photothermal therapy is presented. In this work I examined how this technique can be used to monitor thermal therapy. The experiments were done on non-biological tissue, a tissue mimicking gel phantoms.

The optoacoustic signal amplitude increased linearly with temperature when the ratio of the heating laser power over due to dilution times of GNR is equal or more than 1.5.

$$\frac{Power}{Dilutiom} \geq 1.5$$

GNRs could not only be used to substantially increase the heating efficiency of photothermal therapy, but also to generate an optoacoustic signal. It was shown in this work that they are a suitable candidate for thermal therapy enhancement and optoacoustic imaging.

Laser power and GNR concentration are two principal factors that determine the effectiveness of this technique. The ability to generate optoacoustic images in the tissue equivalent phantom, as well as the ability to detect changes in the optoacoustic signals as a function of the temperature in a mimicked tissue gel phantom during photothermal therapy confirms that optoacoustic imaging has the potential to monitor temperature elevation during

photothermal therapy.

6.2 Future work

Experiments were performed on a GNR gel phantom which was a water based phantom. The variation of OA signal vs. temperature shows there is potentially a linear relationship between the temperature increase and the change in the optoacoustic signal. But in some sets of experiments, this linearity was not observed.

As it was mentioned in the discussion the possibility of fat in porcine skin gel phantom makes an idea for research. The effect of fat tissue on these types of measurements should be carefully examined in the future.

Photothermal therapy is based on heat transfer. Modeling the temperature changes during photothermal therapy (such as the effect of different GNR concentrations in the gel phantom on the temperature distribution and the optoacoustic signal) can be another research.

Determining the **(a)** and **(b)** parameters in $\Gamma(T)$ of the equation 21 in chapter 2 could be obtained by temperature measurement during photothermal therapy.

Generating $I_{OA}(T)$ images during photothermal therapy instead signals as a single location is one of the next steps in the project. Generating images takes more time which depends to step size of the raster scan, the imaging area and the RF averaging.

Appendix A - RF lines

In this chapter all of the raw data during heating and cooling according to table 3.1 are sorted. The rising of the amplitude during heating shows the I_{OA} (t) has a direct relation to the temperature. Also the falling the amplitude after turning off the heating laser shows this relation repeatedly. Legends indicate the time of firing of OA laser during the experiment for each RF line.

The two purple dashed show the boundaries of phantom edges and their distances due to OA transducer. The rising of the RF line in area of the heating laser, around 25 m from the transducer, especially for the first six set is observable too.

A:

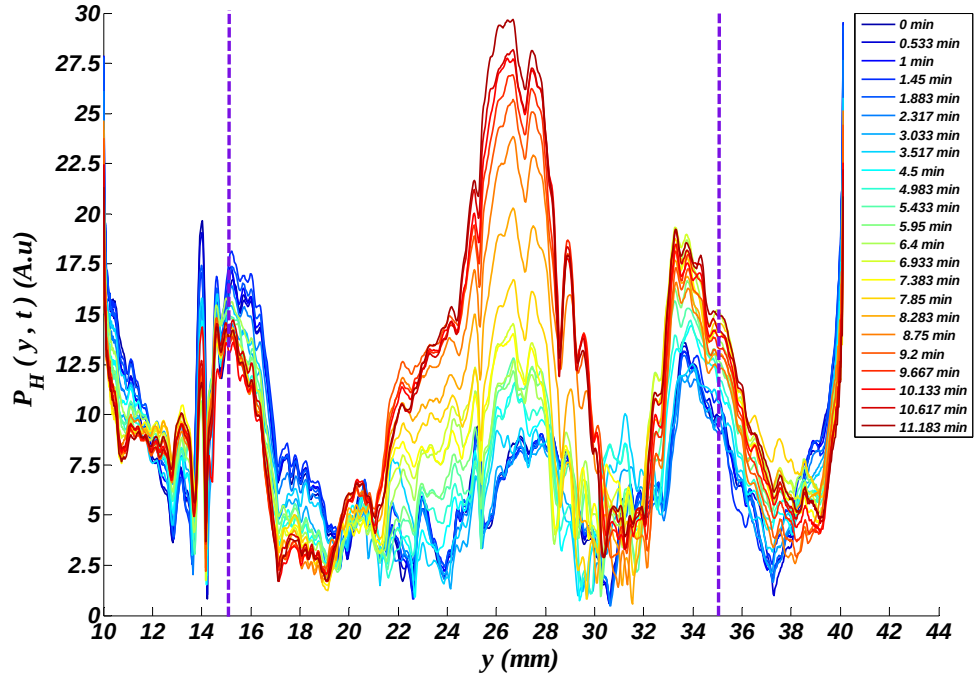

B:

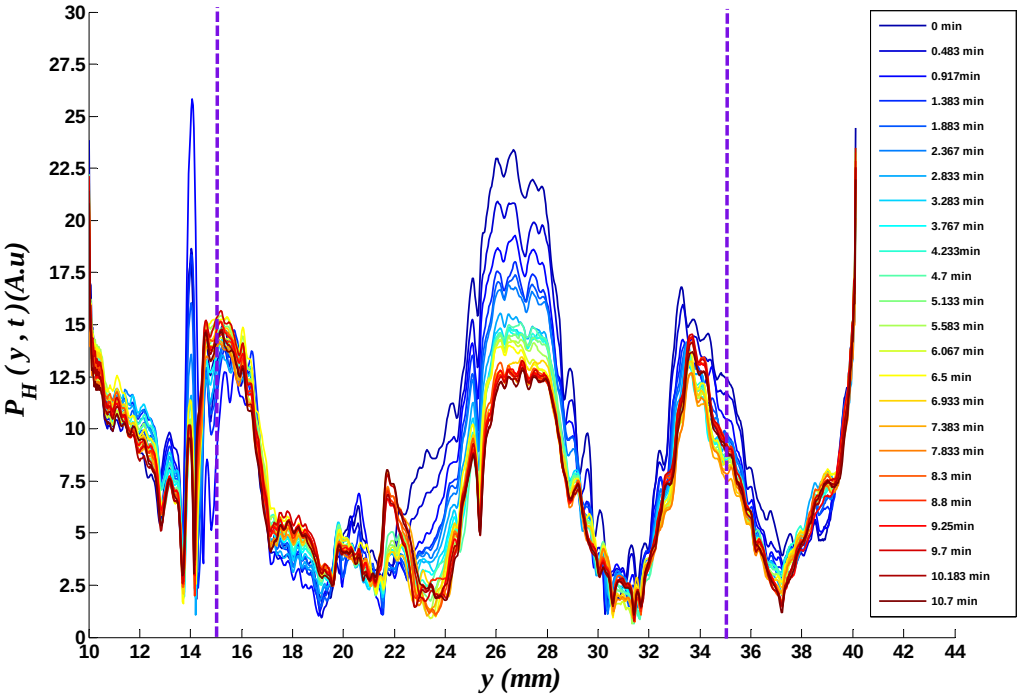

Figure A.1 Processed RF signals for a 2X- GNR diluted phantom with 3 W of laser power. A) preheat and heating phase. Legends show the time after first RF data acquistion time. B) cooling phase. Legends show the elapsed time after turning off the heating laser.

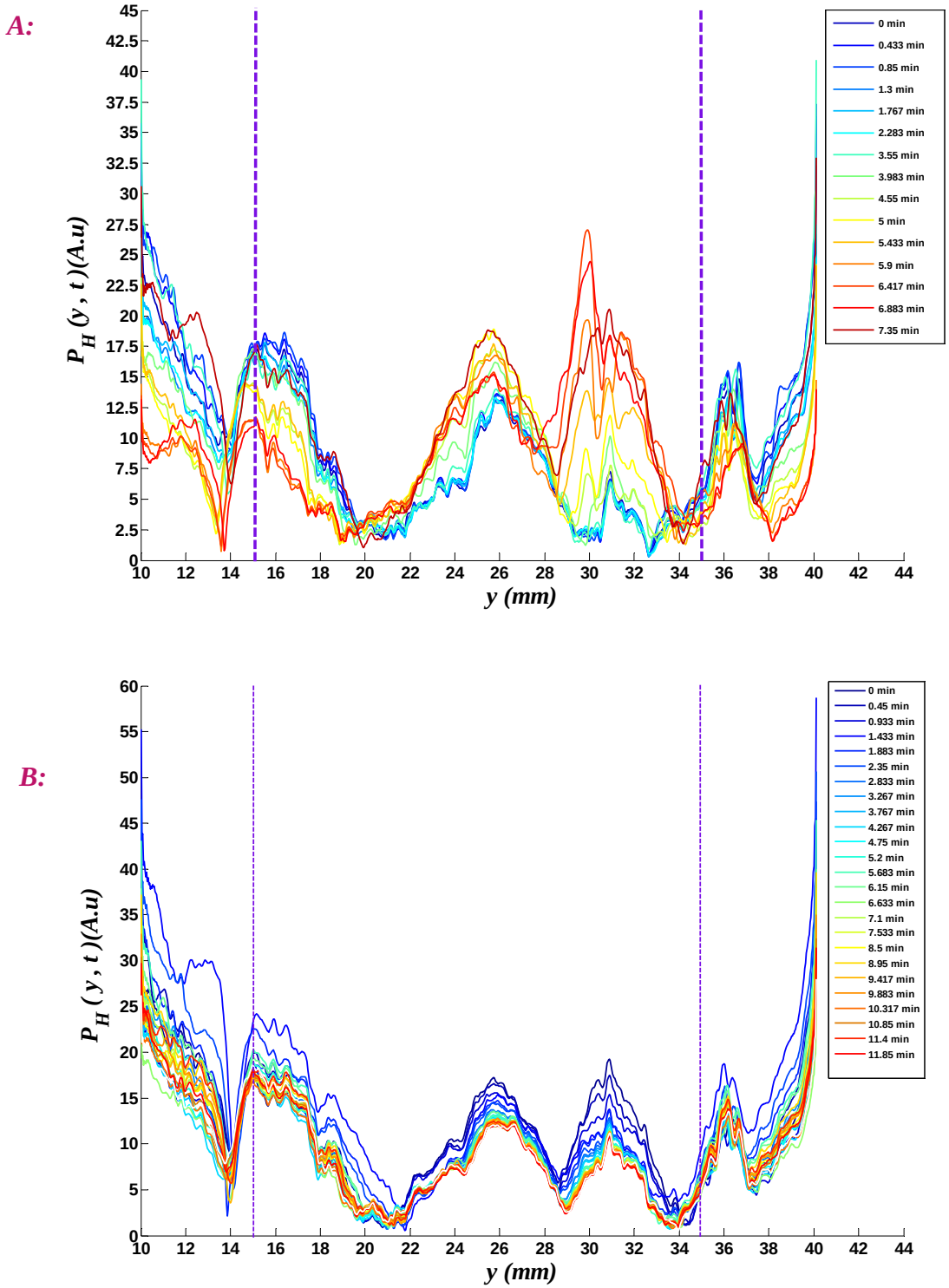

Figure A.2 Processed RF signals for a 2X- GNR diluted phantom with 5W of laser power. A) preheat and heating phase. Legends show the time after first RF data acquistion time. B) cooling phase. Legends show the elapsed time after turning off the heating laser.

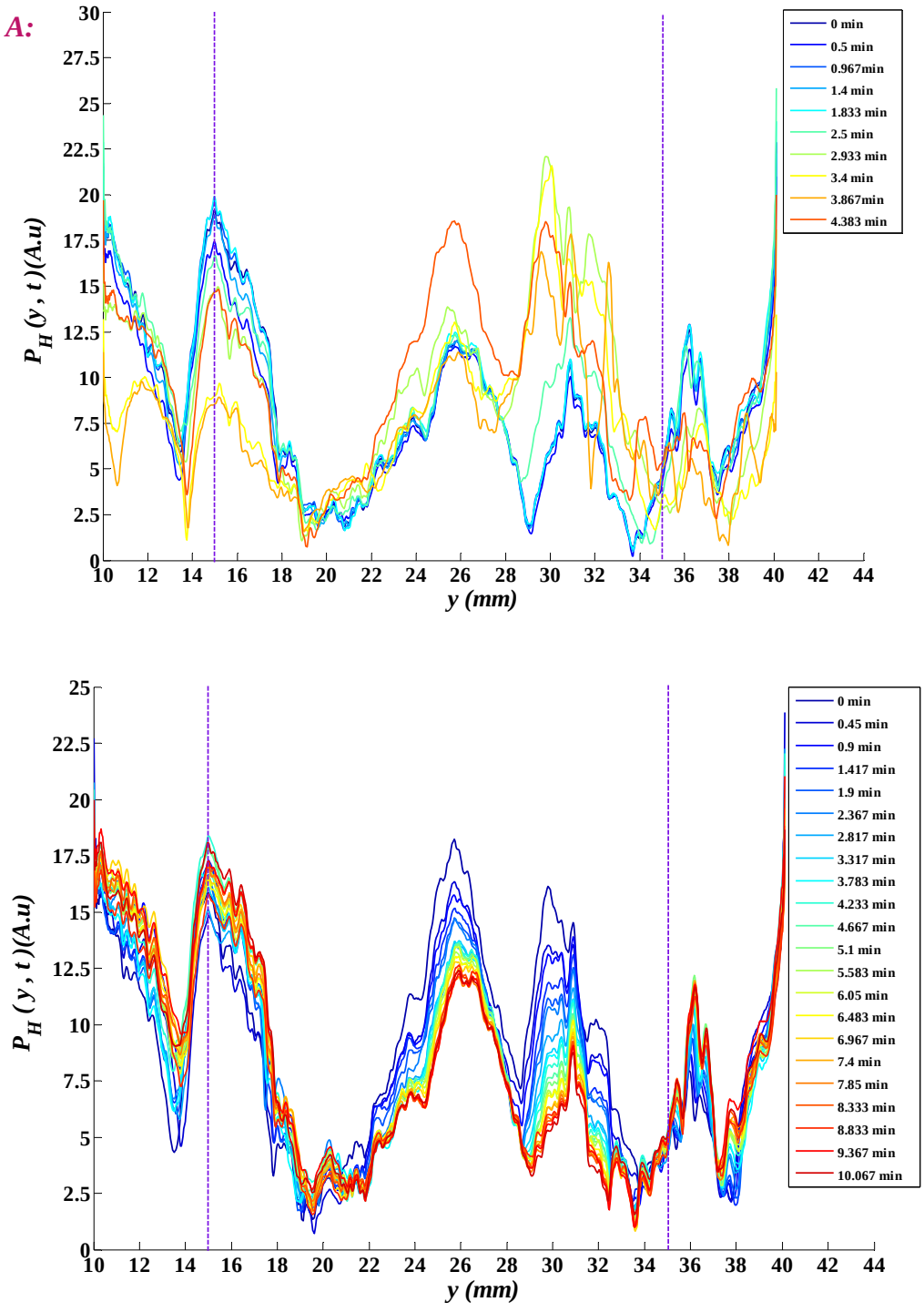

Figure A.3 Processed RF signals for a 2X-GNR diluted phantom with 8W of laser power. A) preheat and heating phase. Legends show the time after first RF data acquistion time. B) cooling phase. Legends show the elapsed time after turning off the heating laser.

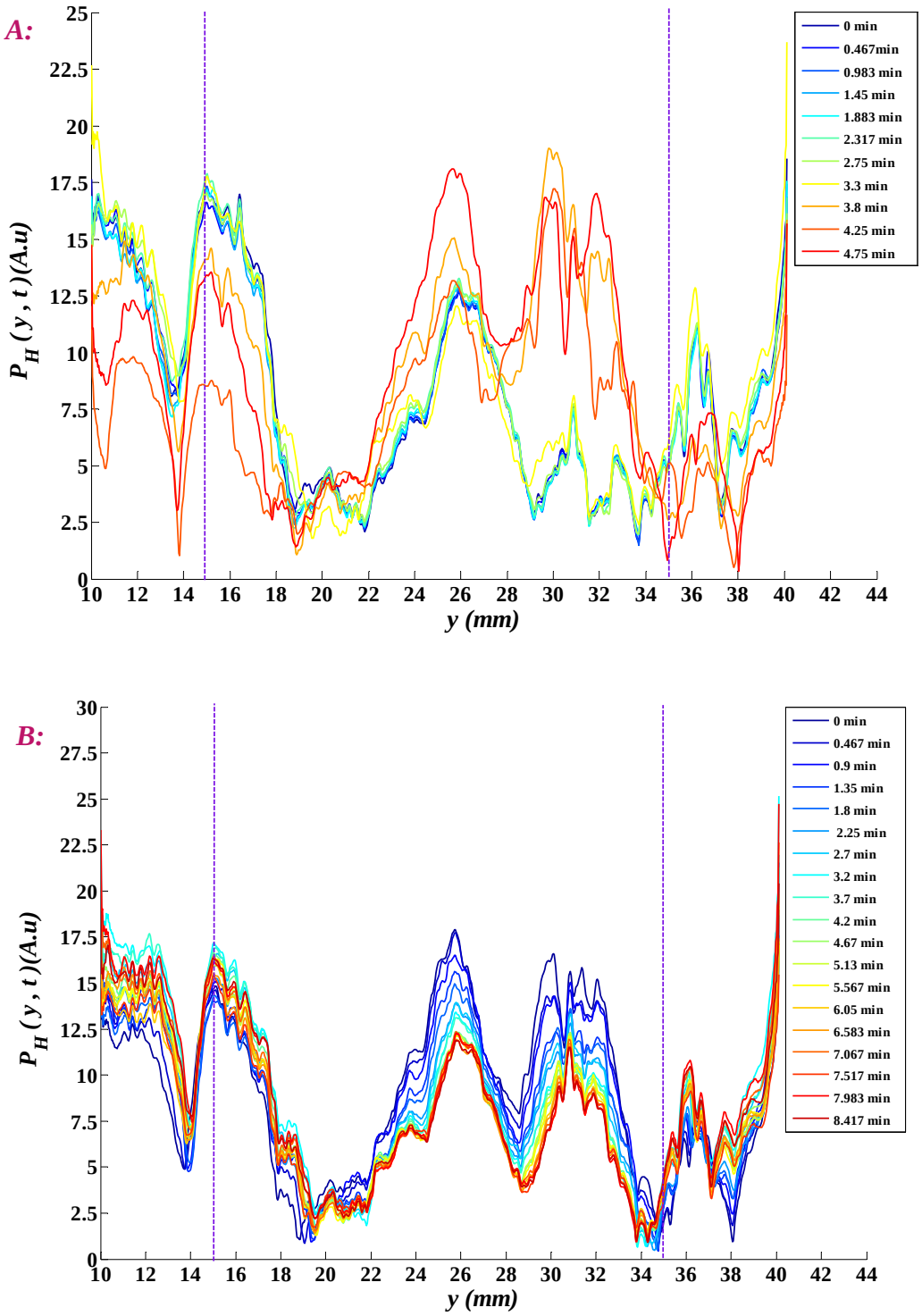

Figure A.4 Processed RF signals for a 2X- GNR diluted phantom with 10W of laser power. A) preheat and heating phase. Legends show the time after first RF data acquistion time. B) cooling phase. Legends show the elapsed time after turning off the heating laser.

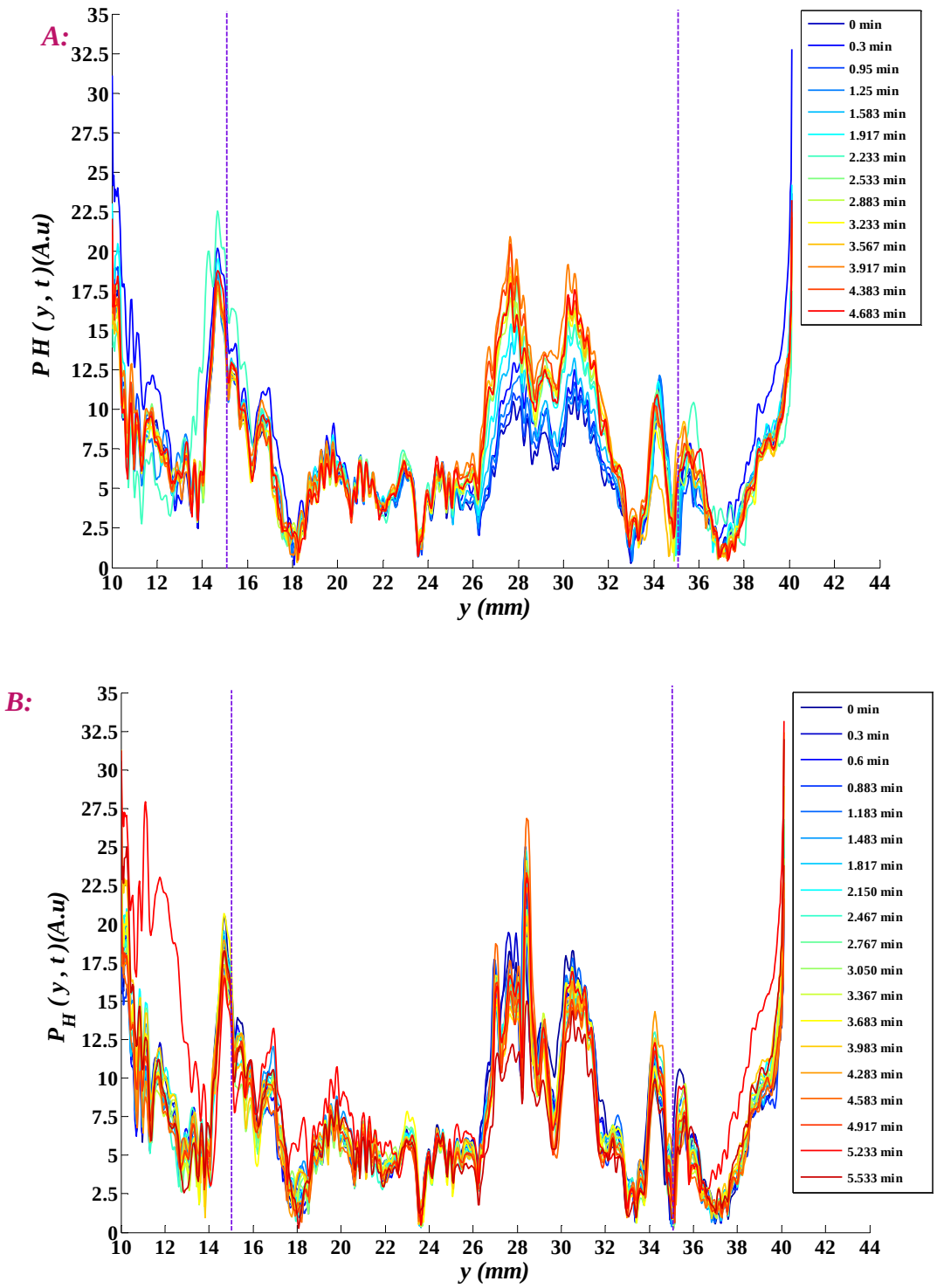

Figure A.5 Processed RF signals for a 4X- GNR diluted phantom with 2W of laser power. A) preheat and heating phase. Legends show the time after first RF data acquistion time. B) cooling phase. Legends show the elapsed time after turning off the heating laser.

A:

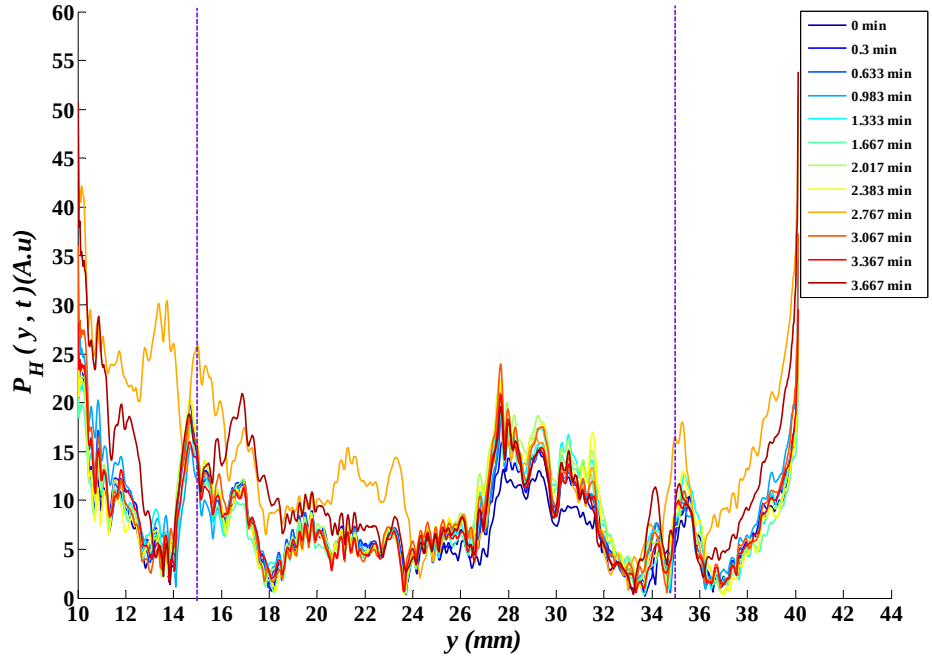

B:

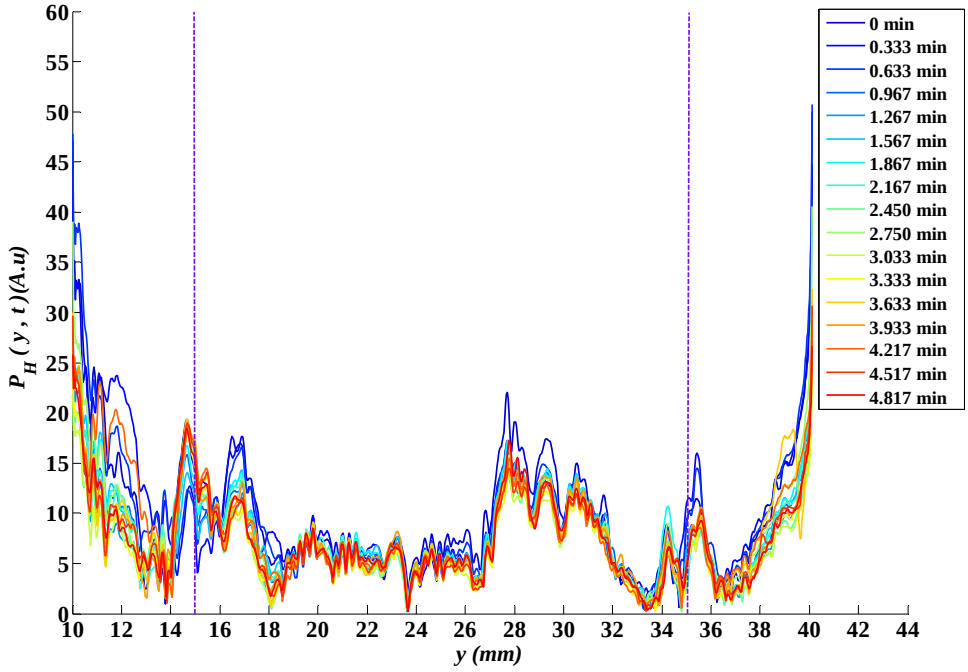

Figure A.6 Processed RF signals for a 4X- GNR diluted phantom with 2.5W of laser power. A) preheat and heating phase. Legends show the time after first RF data acquistion time. B) cooling phase. Legends show the elapsed time after turning off the heating laser.

A:

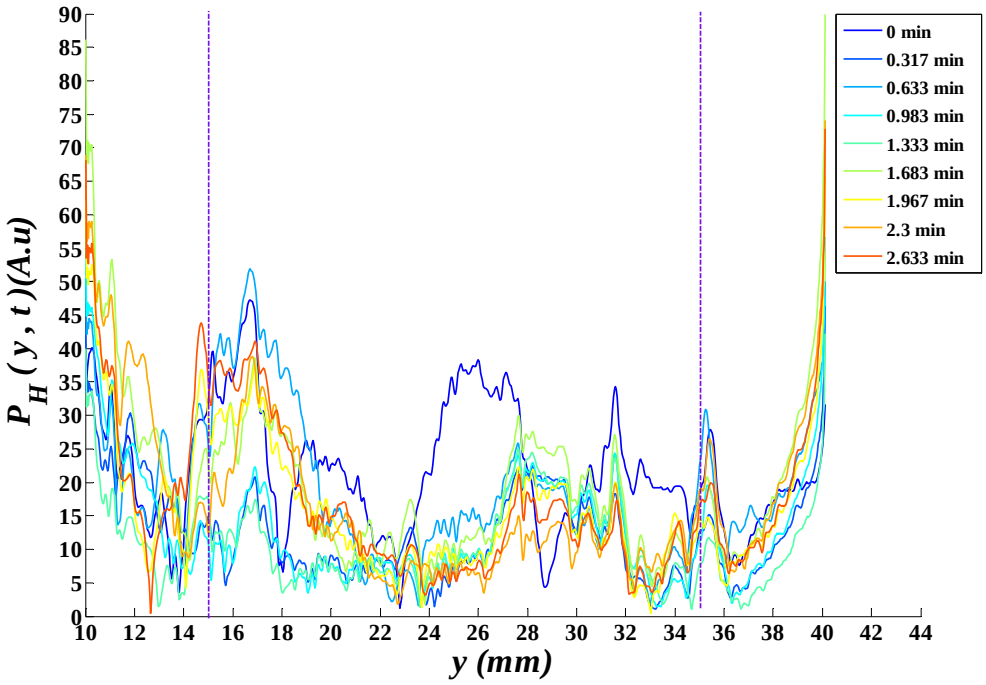

B:

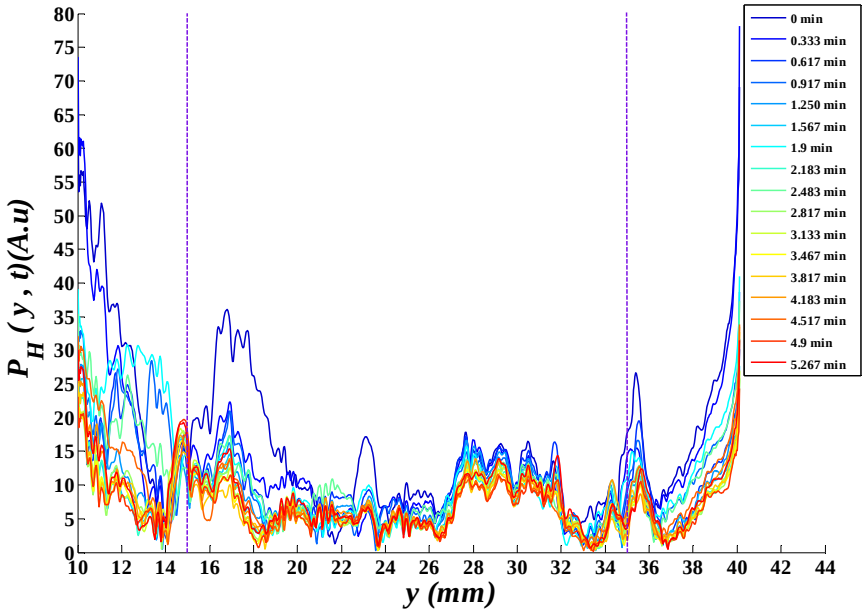

Figure A.7 Processed RF signals for a 4X- GNR diluted phantom with 3W of laser power. A) preheat and heating phase. Legends show the time after first RF data acquistion time. B) cooling phase. Legends show the elapsed time after turning off the heating laser.

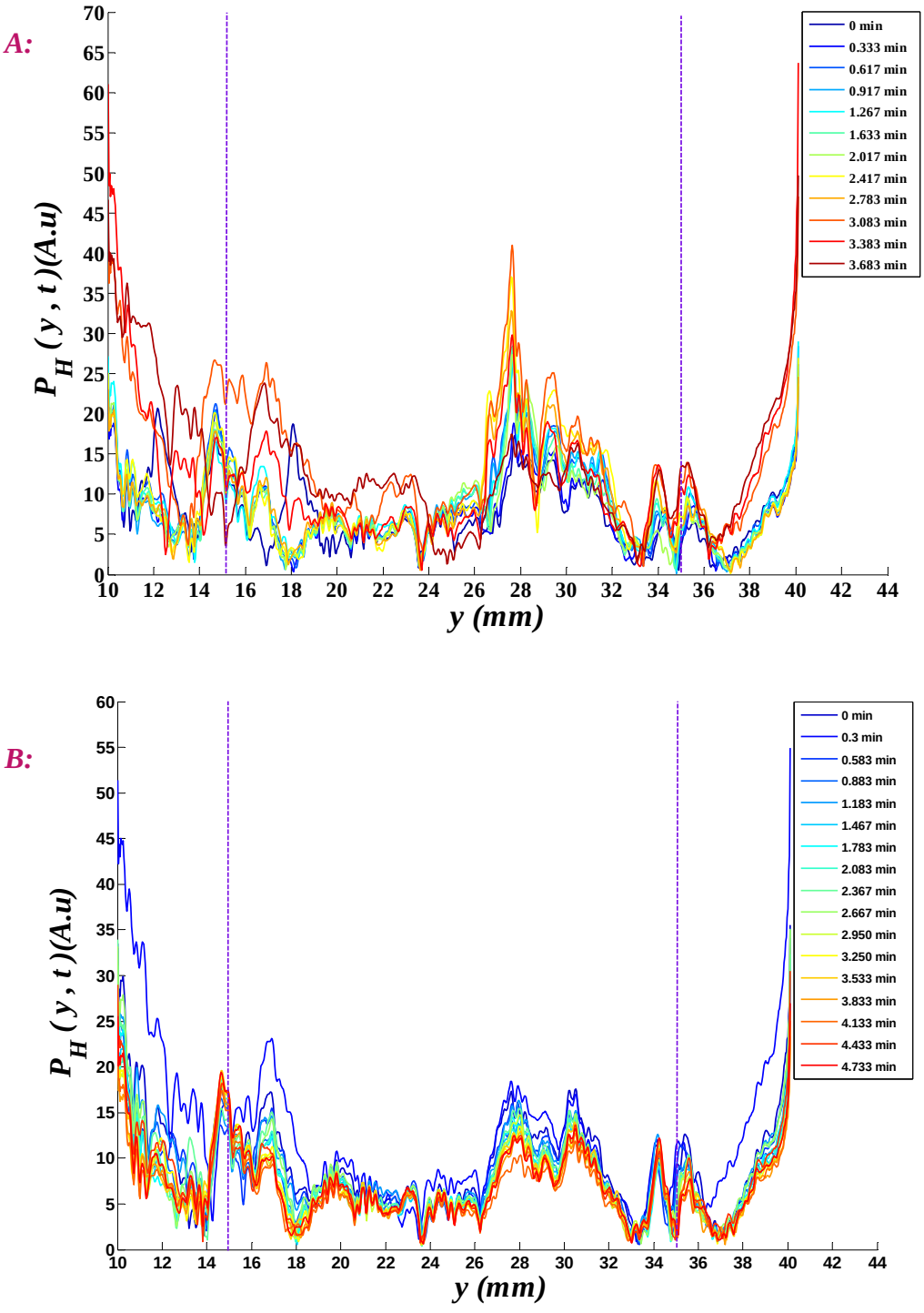

Figure A.8 Processed RF signals for a 4X- GNR diluted phantom with 3.5W of laser power. A) preheat and heating phase. Legneds show the time after first RF data acquistion time. B) cooling phase. Legneds show the elapsed time after turning off the heating laser.

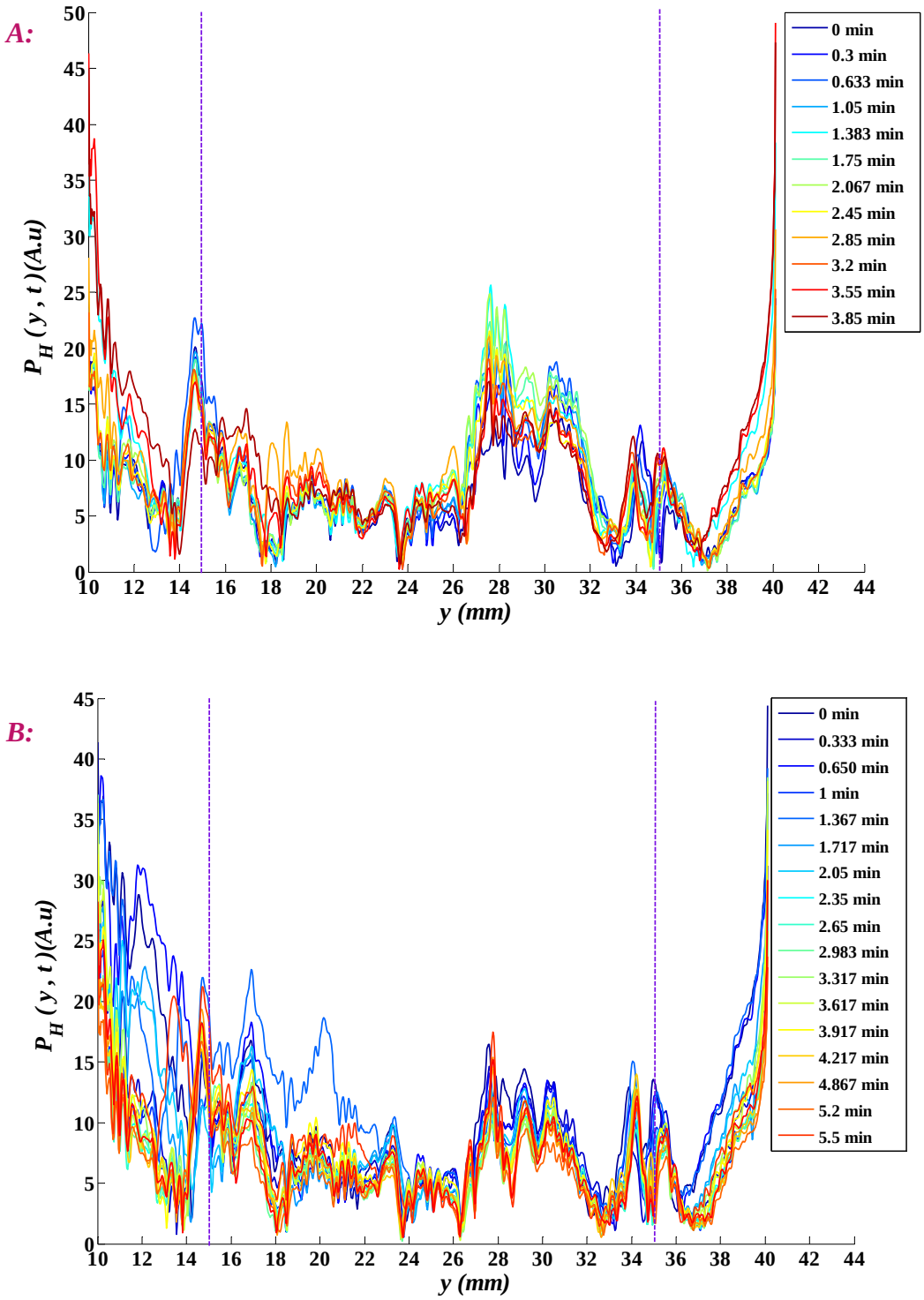

Figure A.9 Processed RF signals for a 4X- GNR diluted phantom with 4W of laser power. A) preheat and heating phase. Legends show the time after first RF data acquistion time. B) cooling phase. Legends show the elapsed time after turning off the heating laser.

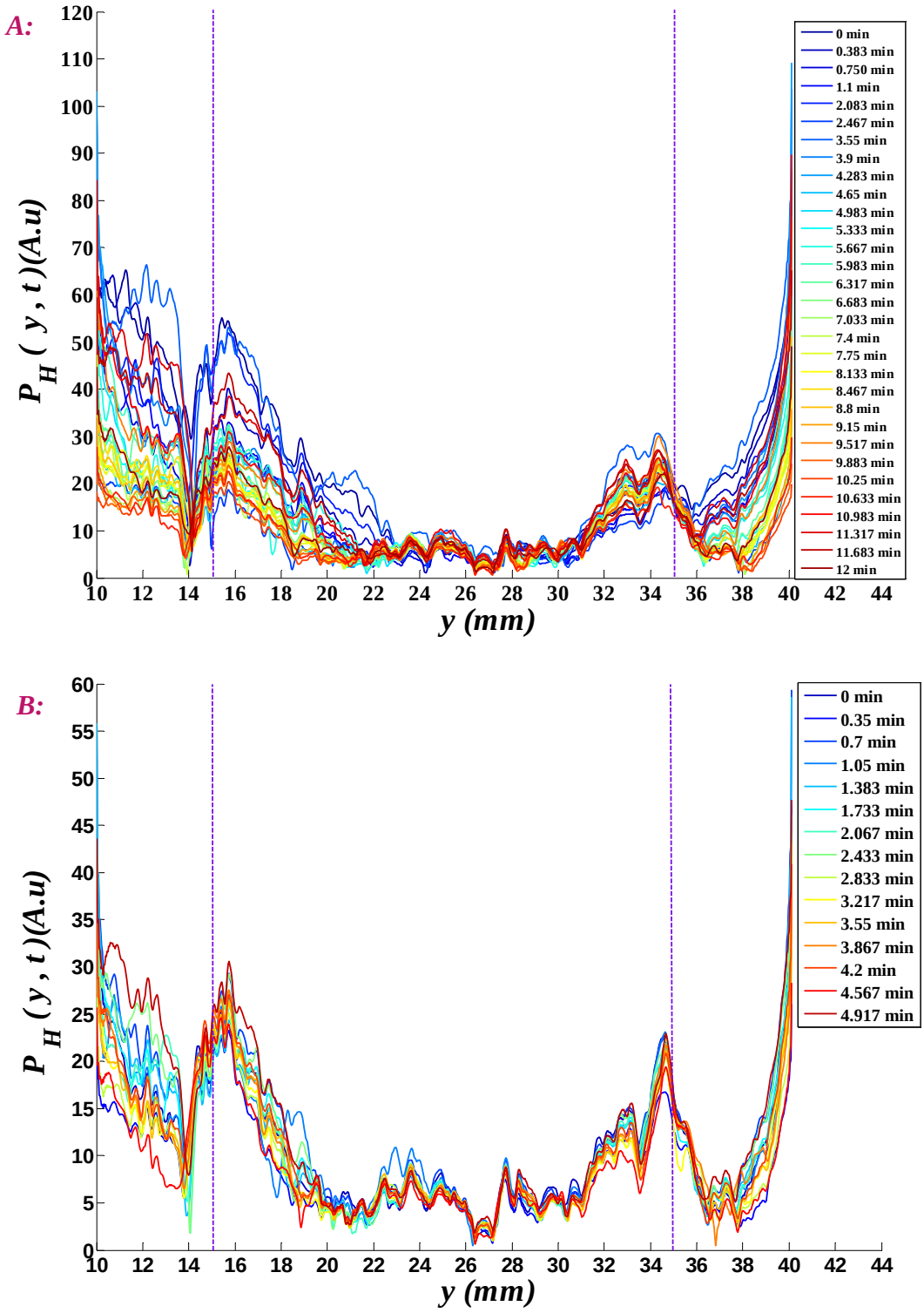

Figure A.10 Processed RF signals for a 5X- GNR diluted phantom with 5W of laser power. A) preheat and heating phase. Legends show the time after first RF data acquistion time. B) cooling phase. Legends show the elapsed time after turning off the heating laser.

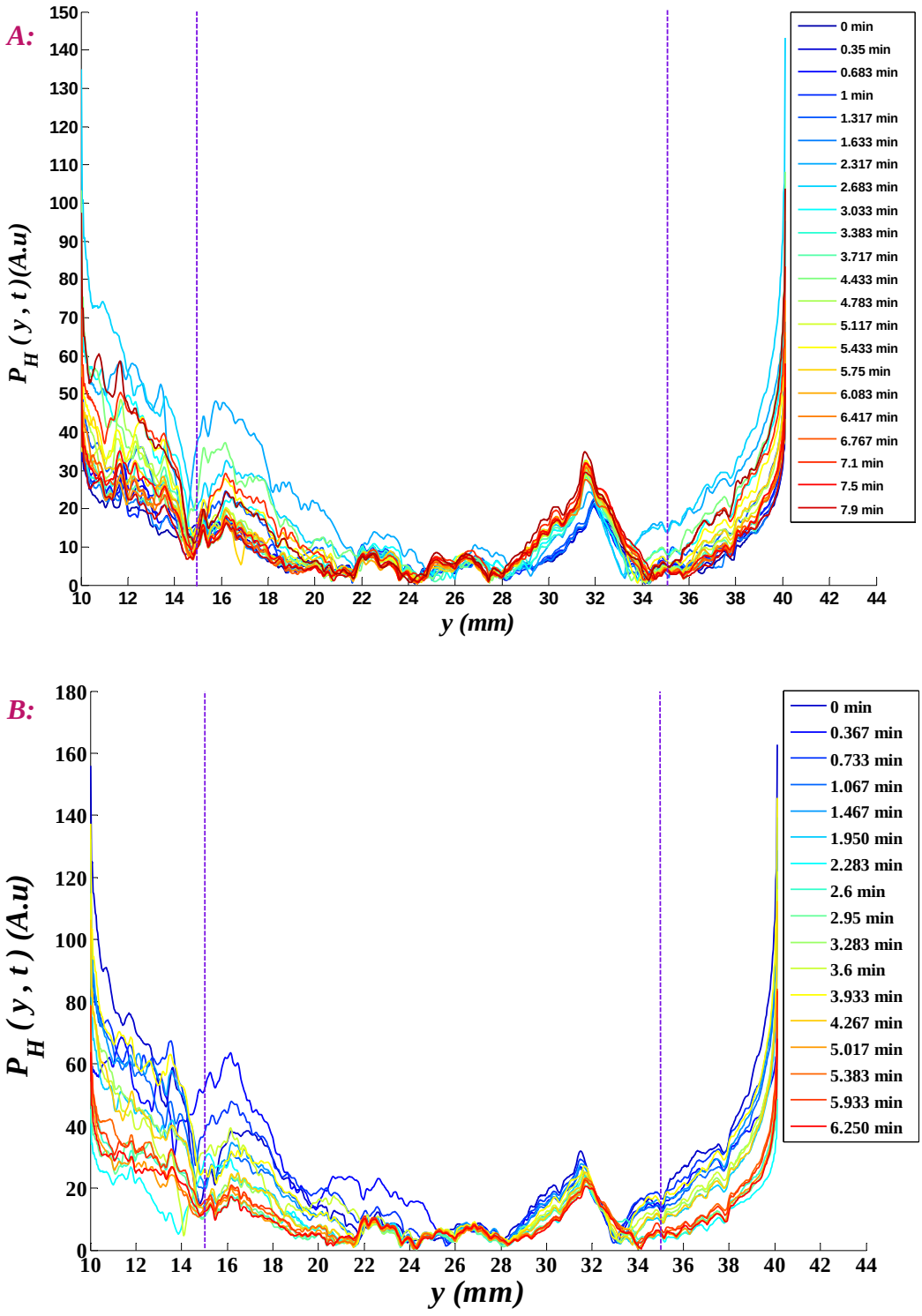

Figure A.11 Processed RF signals for a 5X- GNR diluted phantom with 8W of laser power. A) preheat and heating phase. Legends show the time after first RF data acquistion time. B) cooling phase. Legends show the elapsed time after turning off the heating laser.

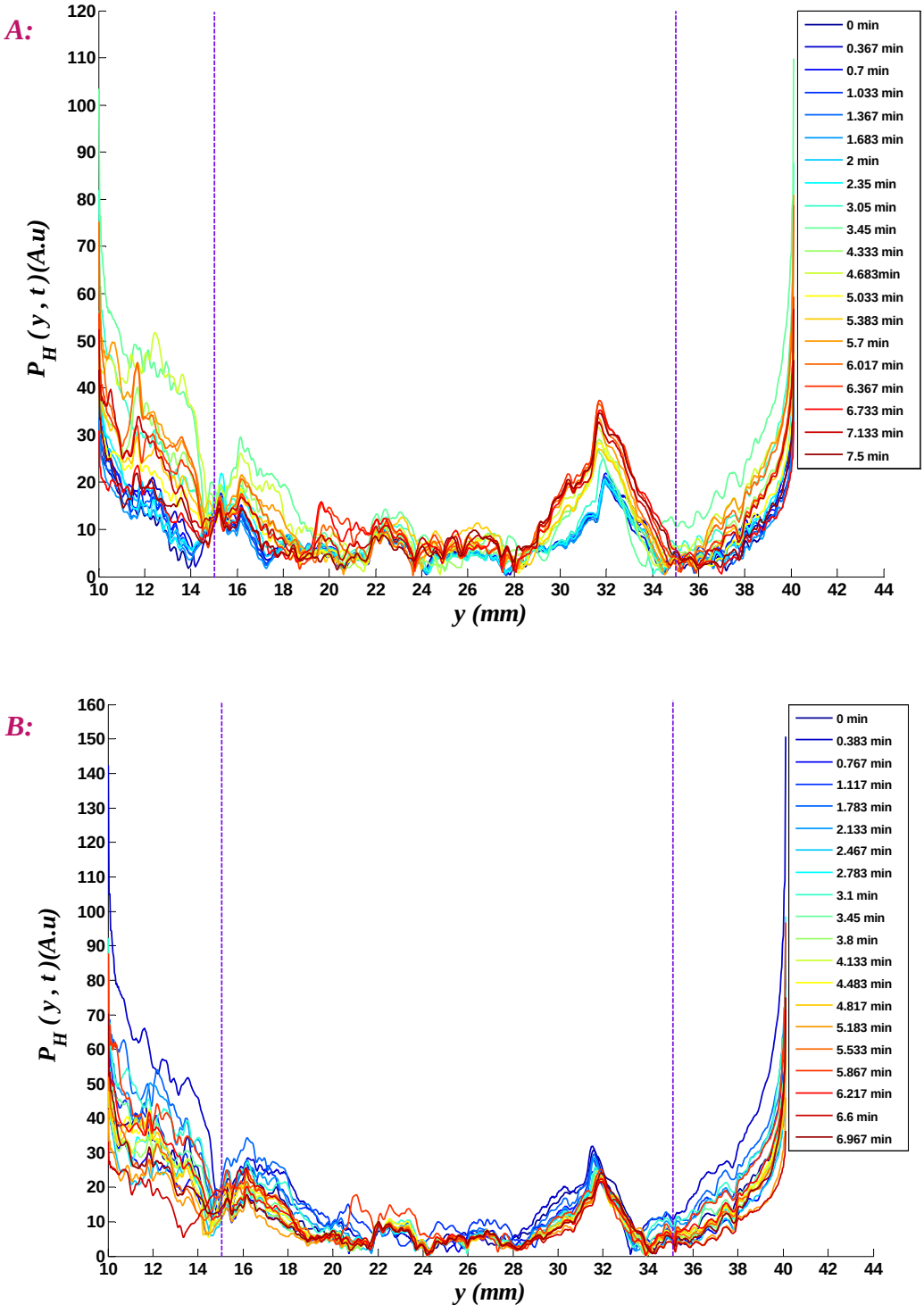

Figure A.12 Processed RF signals for a 5X- GNR diluted phantom with 10W of laser power. A) preheat and heating phase. Legends show the time after first RF data acquistion time. B) cooling phase. Legends show the elapsed time after turning off the heating laser.

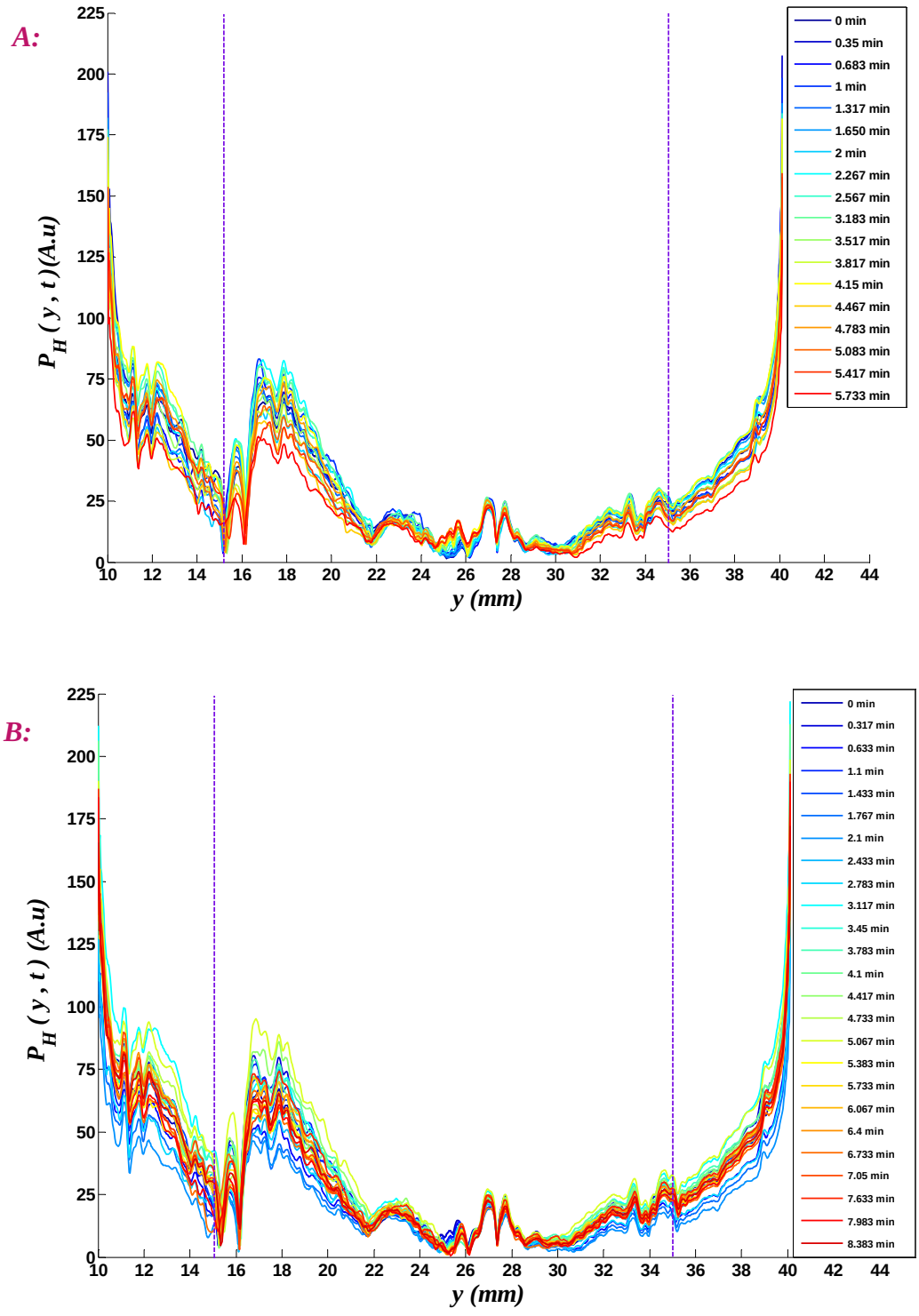

Figure A.13 Processed RF signals for a 6X -GNR diluted phantom with 2.5W of laser power. A) preheat and heating phase. Legends show the time after first RF data acquistion time. B) cooling phase. Legends show the elapsed time after turning off the heating laser.

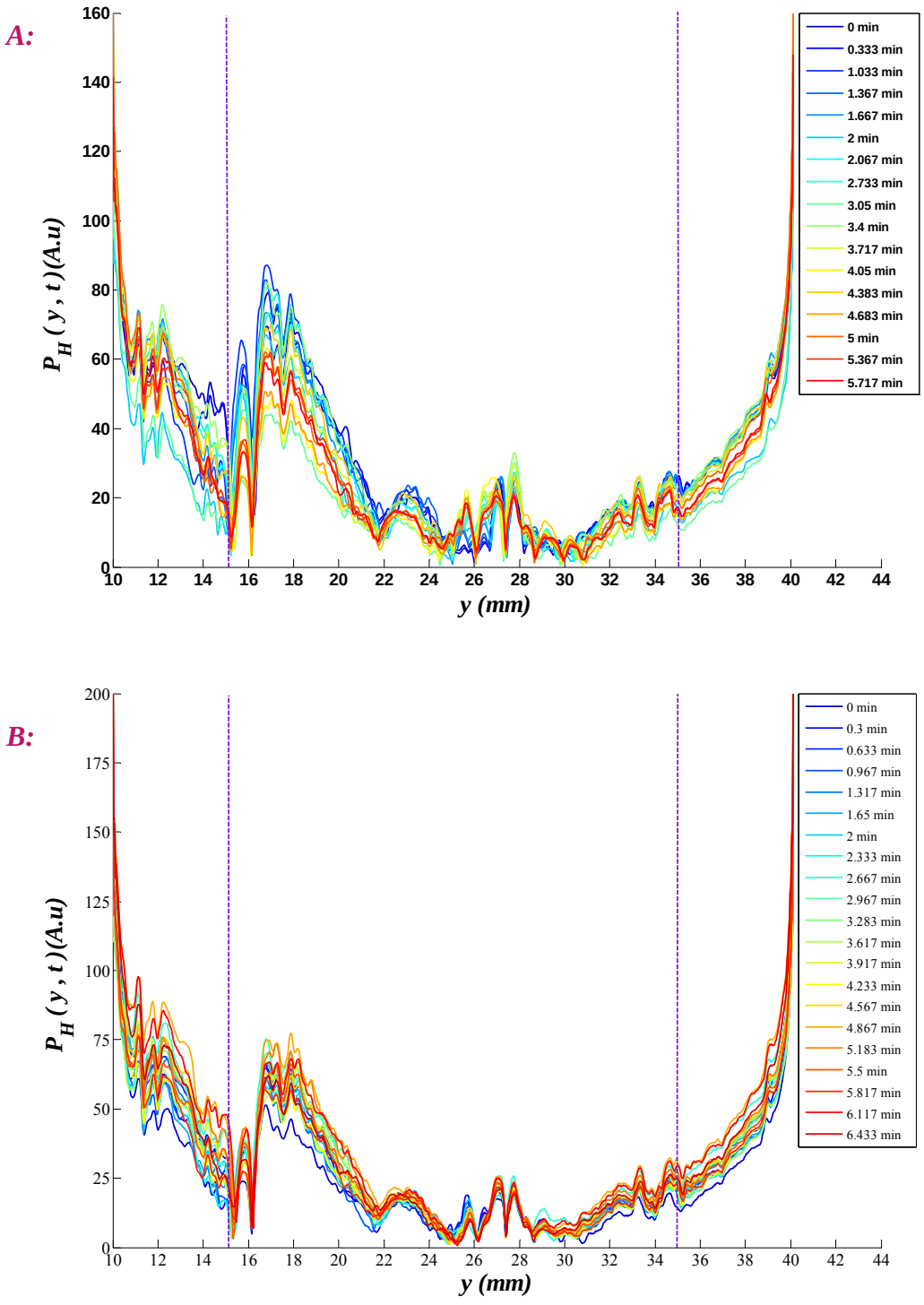

Figure A.14 Processed RF signals for a 6X- GNR diluted phantom with 3W of power. A) preheat and heating phase. Legends show the time after first RF data acquistion time. B) cooling phase. Legends show the elapsed time after turning off the heating laser.

A:

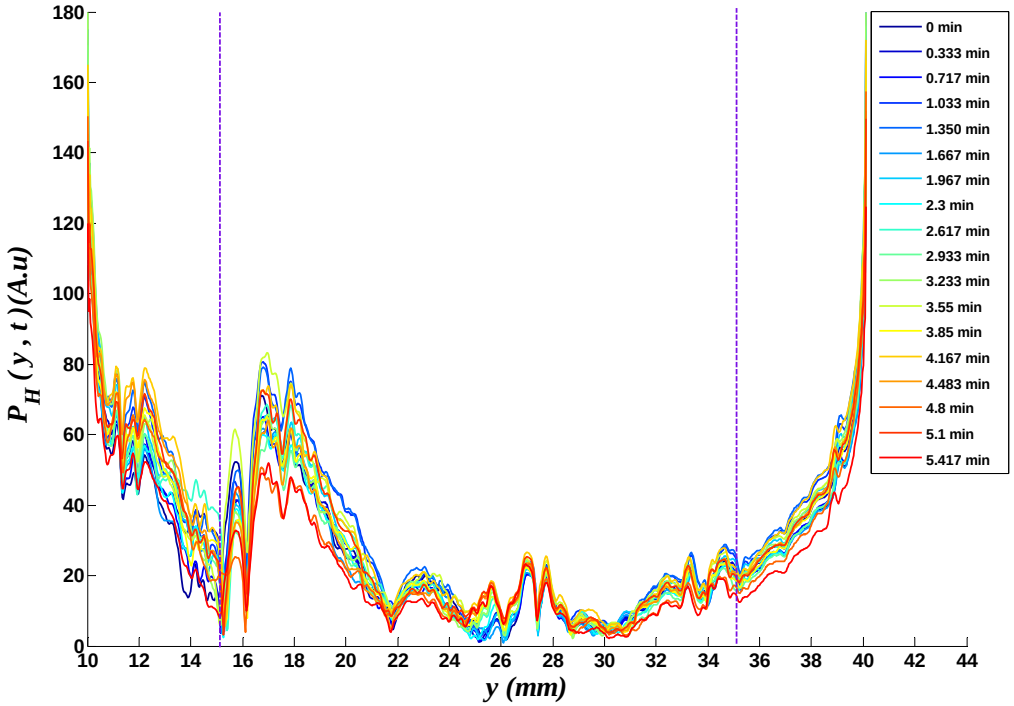

B:

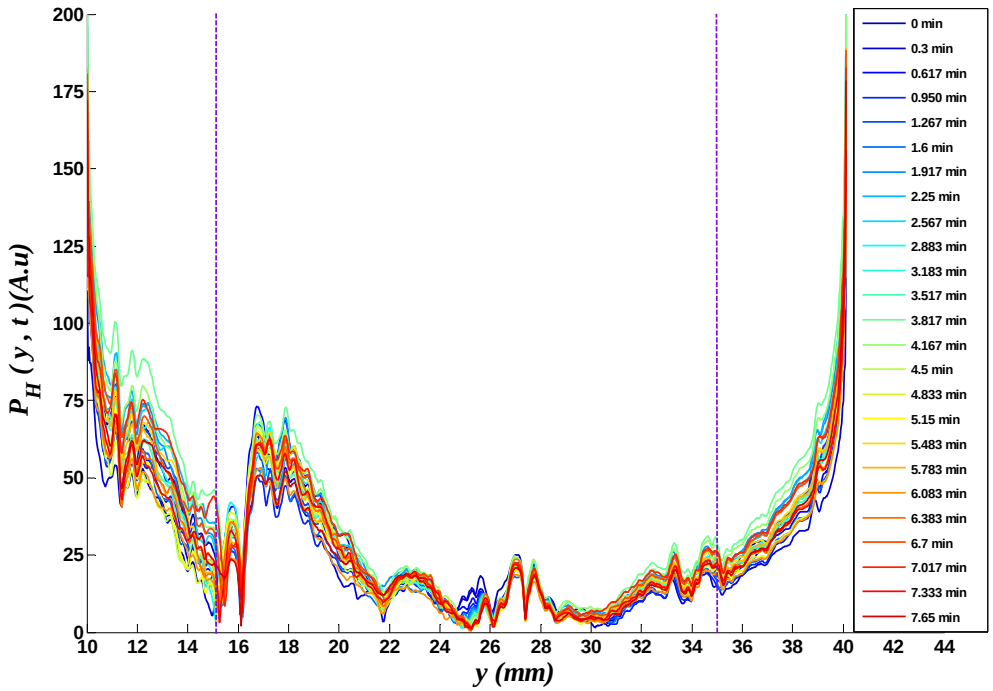

Figure A.15 Processed RF signals for a 6X -GNR diluted phantom with 3.5W of laser power. A) preheat and heating phase. Legends show the time after first RF data acquistion time. B) cooling phase. Legends show the elapsed time after turning off the heating laser.

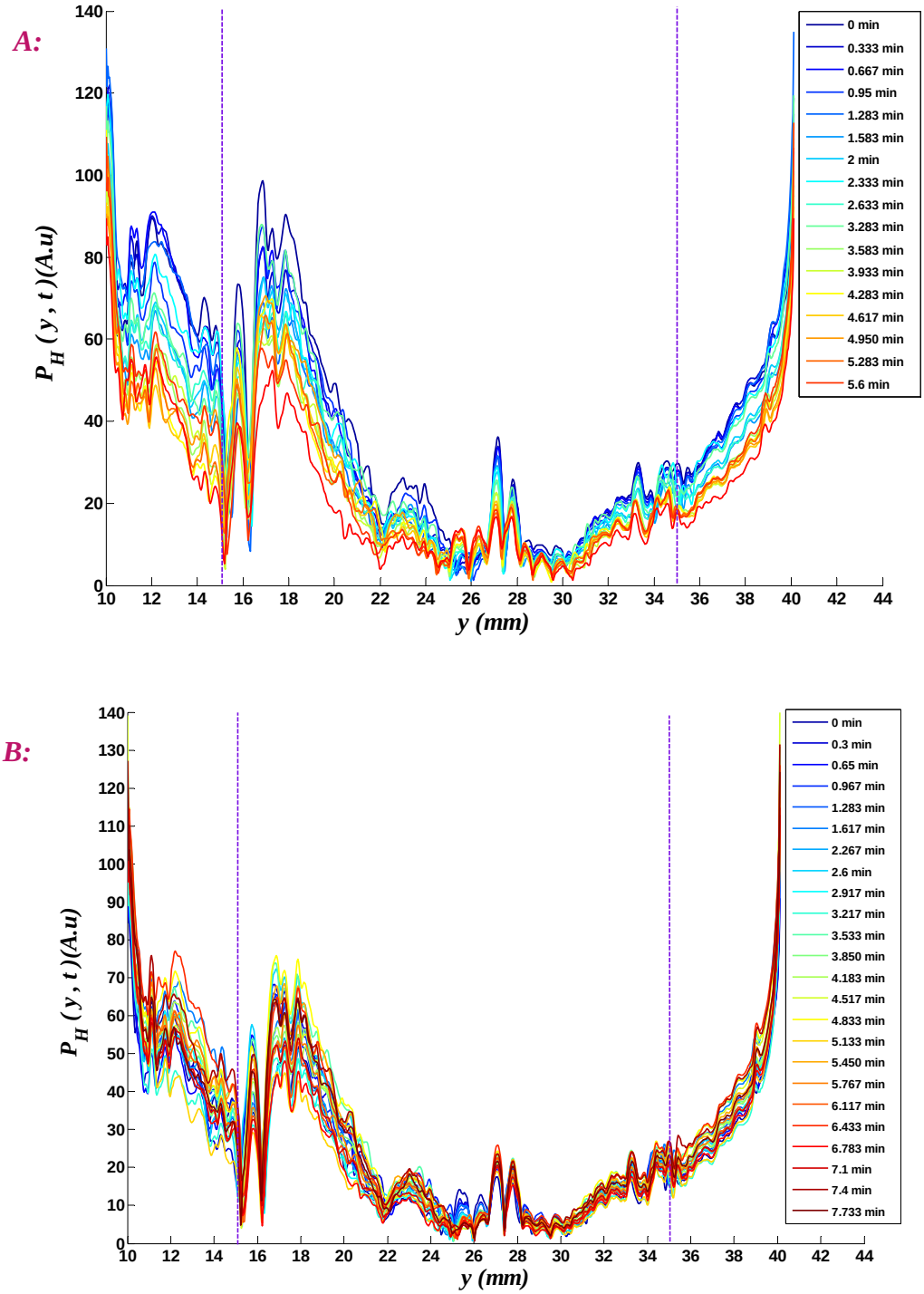

Figure A.16 Processed RF signals for a 6X -GNR diluted phantom with 4W of laser power. A) preheat and heating phase. Legends show the time after first RF data acquistion time. B) cooling phase. Legends show the elapsed time after turning off the heating laser.

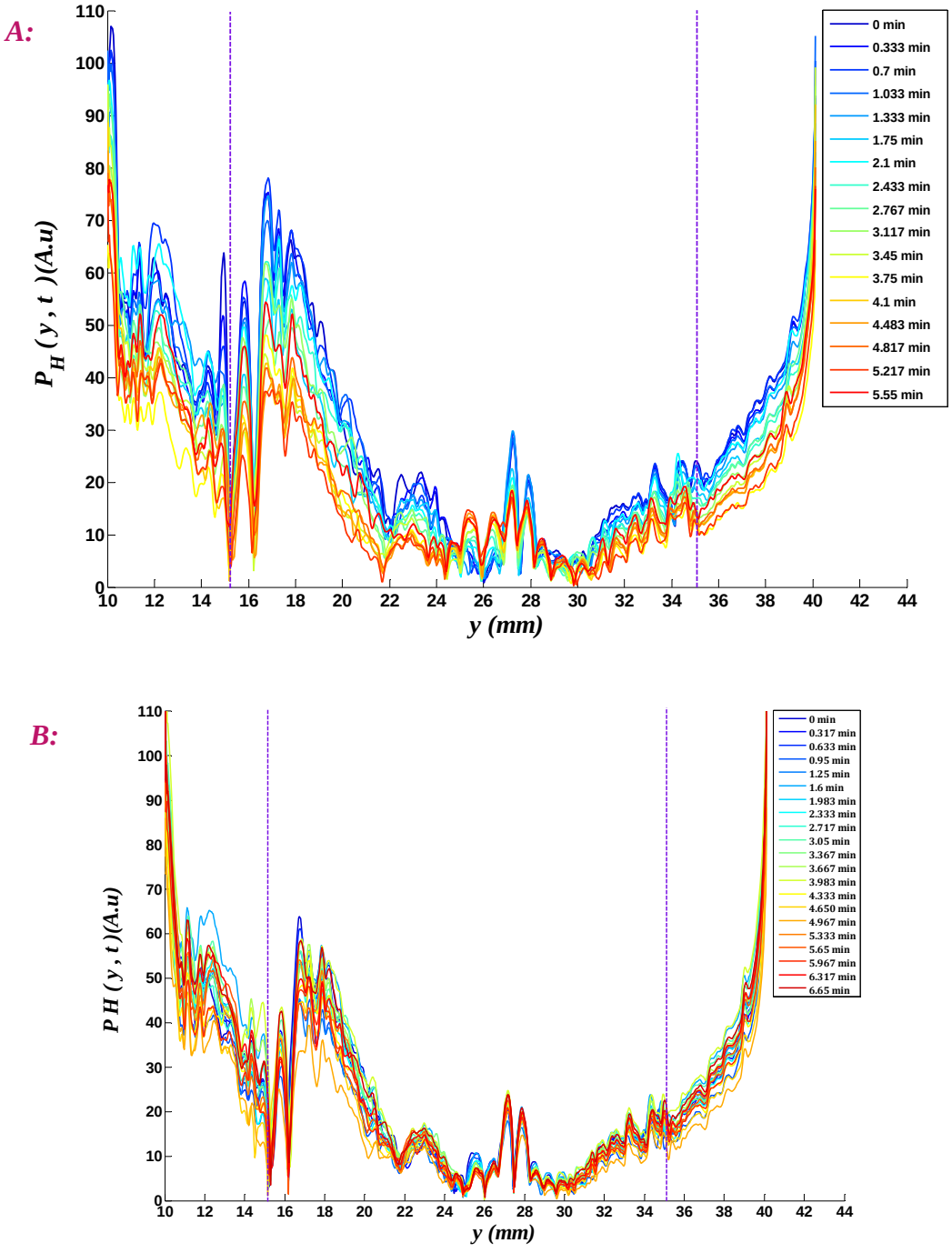

Figure A.17 Processed RF signals for a 6X -GNR diluted phantom with 5W of laser power. A) preheat and heating phase. Legends show the time after first RF data acquistion time. B) cooling phase. Legends show the elapsed time after turning off the heating laser.

Appendix B - MATLAB Codes

The MATLAB codes were used for creating of the three graphs are in following pages.

First code generates the RF lines.

The second code generates the three graphs of Figures 4.3- 4.21, and the third code is the function of second code.

```
close all


clear all
clc
d = dir ('scanning_4X_2-5w*');
n=size(d,1);
for j=1:n
    cd (d(j).name);
%    if regexp(d(j).name,'scanning-2x-3W')==1 && d(j).isdir
%     [rf(j)]=rf(j,'scanning-2x-3W_X0001Y0001Z0001');
%     function [rf] = rf(j,d,f_name)
load 'scanning_4X_2-5w_X0001Y0001Z0001'
captured_data = acquired_data';

b = zeros(815,1);

a = 0;% all lengths are in mm

h1=sqrt(25^2-(2.55)^2);
h2=sqrt(25^2-(4.67)^2);
h3=sqrt(25^2-(6.25)^2);
h4=sqrt(25^2-(7.57)^2);

L1=sqrt((h1+a)^2+(2.55)^2);
L2=sqrt((h2+a)^2+(4.67)^2);
L3=sqrt((h3+a)^2+(6.25)^2);
L4=sqrt((h4+a)^2+(7.57)^2);

%The outer ring is the refernce (L4: length from the element number four
%and the object). In order to find the phase shift for the inner rings,
%one has to substract the length between each element and the object (L1,
L2, L3), Therefore:

d1=(L1-L4);
d2=(L2-L4);
d3=(L3-L4);
d4=(L4-L4);

%Calculation of the time difference

Cw=1.48; % mm/mu_s

t1=d1/Cw; % in micro second (mu_s)
t2=d2/Cw;
t3=d3/Cw;
t4=d4/Cw; % By diffult this value always is zero, since the outer ring
(number four) in the refernce

% Calculation of the shift in the arrays
```

```
Ts=0.025; %Sampling time(mu_s)=1/sampling_frequency, sampling_fequency=40
MHz

sh1=t1/Ts;
sh2=t2/Ts;
sh3=t3/Ts;
sh4=t4/Ts;
% Important: There is a problem here. sh1, sh2, sh3 should be integer
% if we want to shift the arrays of the matrix. However, these values
% are not integer in most of the cases. In order to have integer number
% di=Li-L4=0.037k, where i=1,2,3,4 and k=0,1,2,...; Therefore,
% ti=(.037k)/Cw=0.025k and finally shi=k

% IMPORTANT: BASED ON THE ABOVE DISCUSSION :
%I have to use round function in order to round shi to the nearest
% integer greater than number



%Set F/#=2

R = 25;
z = a+R;

%if (z<=15)

%element_number=1;
%

% element_number=1,2,3,4

b =[zeros(round(sh1),1); captured_data(271:(1085-round(sh1)),4)]+...
    [zeros(round(sh2),1); captured_data(271:(1085-round(sh2)),3)]+...
    [zeros(round(sh3),1); captured_data(271:(1085-round(sh3)),2)]+...
    [zeros(round(sh4),1); captured_data(271:(1085-round(sh4)),1)];
b= abs(hilbert(b));
% b=(b);

%Averaging between the amount of the signals
% B=0;
% n=42;
% for i=1:n
%     B= B+b(i);
% end
% mx=B/n;
% mx=abs(hilbert(mx));



rf=b*100;
rf=abs(hilbert(rf));
%   y= hilbert(b);
%   y=abs(y);
ts = input_params.time_at_start_of_acquisition;
```

```
tf = input_params.last_acquisition_time;
T1 = ts(4)*3600+ts(5)*60+ts(6);
T2 = tf(4)*3600+tf(5)*60+tf(6);
at= (T1 + T2)/2


hold on
cmap = jet(n);
plot ((((271:1085)/1536)*56.8),abs(rf),'color',cmap(j,:),'Linewidth',2);
% plot ((((381:1536)/1536)*56.8),abs(rf));
% plot (AT,abs(rf),'*');
xlabel ('Distance from the transducer(mm)', 'FontSize' ,14);
ylabel ('abs hilbert signal(mv) ', 'FontSize' ,14);
legend('0 min','0.333 min ','0.633 min','0.967 min ','1.267 min','1.567
min','1.867 min','2.167 min ','2.450 min','2.750 min','3.033 min','3.333
min','3.633 min','3.933 min','4.217 min','4.517 min','4.817 min')
title('abs hilbert signal 4X-GNR during cooling between 10.02-40.12 mm from
the transducer in 2.5 W ','FontSize',15)
 cd('..');
end
```

```
close all
clear all
clc
d = dir ('scanning_4X_4w*');
n=size(d,1);
for j=1:n
    cd (d(j).name);
   if regexp(d(j).name,'scanning_4X_4w')==1 && d(j).isdir
    [ar(j),at(j)]=arat(j,d,'scanning_4X_4w_X0001Y0001Z0001');
   end
   cd('..');
end
AT=((at-at(1))/60);
% AT=(at)/60;
hold on
% % plot (AT,abs(mx));
plot (AT,abs(ar),'-p');
xlabel ('Time(minute)', 'FontSize' ,14);
ylabel ('integration abs hilbert OA signal(mv)', 'FontSize' ,14);
title('integration abs hilbert OA signal of 4X-GNR area in 4W between
26.86-30.782mm from the transducer ','FontSize',15)
% [yi]= interp1 (AT,mx,'9xheating');
 cd('..');

 L=load ('scanning-4wn-N1.txt');
% L= import ('HEATING1.txt');
ar=abs(ar);
I=abs((L(:,1)));
I=I/60;
 J=abs((L(:,2)));
yi=interp1(AT,ar,I);% I=(term1(:,2));interpolation according to pressure
yi=abs(yi);
zi=interp1(I,J,AT);% I=(term1(:,2));interpolation according to Temperature
zi=abs(zi);

%  figure
%  hold on
% plot (I,yi,'*')
% % plot (I,yi)
% xlabel ('Time(minute)', 'FontSize' ,14);
% ylabel ('abs hilbert pressure after int', 'FontSize' ,14);
% title(' abs hilbert pressure after int 4x-high concentration'
,'FontSize',15)

% Temperature and Signal
figure
hold on
Grid on
plot (J,yi,'-*')
plot (J,yi)
xlabel ('Temperature(C)', 'FontSize' ,14);
ylabel ('integration abs hilbert OA signal(mv)', 'FontSize' ,14);
```

```
title('variation integration abs hilbert OA signalof 4X-GNR in 4W between
26.86-30.782 mm by-P','FontSize',15)

figure
hold on
Grid on
plot (zi,ar,'-*')
plot (zi,ar)
xlabel ('Temperature(C)', 'FontSize' ,14);
ylabel ('integration abs hilbert OA signal(mv)', 'FontSize' ,14);
title('variation integration abs hilbert OA signal of 4X-GNR in 4W between
26.86-30.782 mm by T','FontSize',15)
%Temperature & time
figure
hold on
plot (I,J,'-*')
plot (I,J)
xlabel ('Time(minute)', 'FontSize' ,14);
ylabel ('Temperature(C)', 'FontSize' ,14);
title('Changes of Temperature 4X-GNR in 4W by time','FontSize',15)
```

```
function [ar,at] = arat(j,d, f_name)
load(f_name);
captured_data = acquired_data';

b = zeros(1536,1);

a = 0;% all lengths are in mm

h1=sqrt(25^2-(2.55)^2);
h2=sqrt(25^2-(4.67)^2);
h3=sqrt(25^2-(6.25)^2);
h4=sqrt(25^2-(7.57)^2);

L1=sqrt((h1+a)^2+(2.55)^2);
L2=sqrt((h2+a)^2+(4.67)^2);
L3=sqrt((h3+a)^2+(6.25)^2);
L4=sqrt((h4+a)^2+(7.57)^2);

%The outer ring is the refernce (L4: length from the element number four
%and the object). In order to find the phase shift for the inner rings,
%one has to substract the length between each element and the object (L1,
L2, L3), Therefore:

d1=(L1-L4);
d2=(L2-L4);
d3=(L3-L4);
d4=(L4-L4);

%Calculation of the time difference

Cw=1.48; % mm/mu_s

t1=d1/Cw; % in micro second (mu_s)
t2=d2/Cw;
t3=d3/Cw;
t4=d4/Cw; % By diffult this value always is zero, since the outer ring
(number four) in the refernce

% Calculation of the shift in the arrays

Ts=0.025;%Sampling time(mu_s)=1/sampling_frequency, sampling_fequency=40
MHz

sh1=t1/Ts;
sh2=t2/Ts;
sh3=t3/Ts;
sh4=t4/Ts;
% Important: There is a problem here. sh1, sh2, sh3 should be integer
% if we want to shift the arrays of the matrix. However, these values
% are not integer in most of the cases. In order to have integer number
```

```
% di=Li-L4=0.037k, where i=1,2,3,4 and k=0,1,2,...; Therefore,
% ti=(.037k)/Cw=0.025k and finally shi=k

% IMPORTANT: BASED ON THE ABOVE DISCUSSION :
%I have to use round function in order to round shi to the nearest
% integer greater than number



%Set F/#=2

R = 25;
z = a+R;

%if (z<=15)

%element_number=1;
%

% element_number=1,2,3,4

b =[zeros(round(sh1),1); captured_data(1:(1536-round(sh1)),4)]+...
    [zeros(round(sh2),1); captured_data(1:(1536-round(sh2)),3)]+...
    [zeros(round(sh3),1); captured_data(1:(1536-round(sh3)),2)]+...
    [zeros(round(sh4),1); captured_data(1:(1536-round(sh4)),1)];

b= abs(hilbert(b));
b=(b*100);



%%% OLD METHOD
% delta_x = 0.037 ;%sampling disatnce in mm
% area = b(649:811)'; %24mm to 30mm
% area = sum(area)*(delta_x);%area under the curve (amplitude vs. distance)
% ar = area;

%%% USING MATLAB METHOD
% x = (25:0.037:27.997);
% %
% area = trapz(x,b(676:757)');
% area = 0.037*trapz(b(676:757)');
% %
% ar = area;

%% Cumulative Integral Method
x = (26.86:0.037:30.782);
%
cumulative_area = cumtrapz(x, b(726:832)');
cumulative_area= 0.037*cumtrapz(b(726:832)');
%
ar = cumulative_area(107);
```

```
%
% mx=max(b);
% mx=abs(hilbert(mx));
%   y= hilbert(b);
%   y=abs(y);
ts = input_params.time_at_start_of_acquisition;
tf = input_params.last_acquisition_time;
T1 = ts(4)*3600+ts(5)*60+ts(6);
T2 = tf(4)*3600+tf(5)*60+tf(6);
at= (T1 + T2)/2;
% at=ts;
End
```

References

[1] US National Institutes of Health (National Cancer Institute), Cancer topics. What is cancer? 2010, Available: http://www.cancer.gov/cancertopics/cancerlibrary/what-is-cancer, Nov.09/2010.

[2] Robert M. Nakamura, Wayne W. Grody, James T. Wu, Cancer Diagnostics: Current and Future Trends . *Clinical Chemistry*, vol.51, pp.1757-1758, 2005.

[3] S. Link and M. A. El-Sayed, Size and temperature dependence of the plasmon absorption of colloidal gold nanoparticles. *J Phys Chem B 103(21),* pp. 4212-4217, 1999.

[4] R. W. Y. Habash, R. Bansal, D. Krewski and H. T. Alhafid, Thermal therapy, part III: Ablation techniques. *Crit. Rev. Biomed. Eng. 35(1-2),* pp. 37-121, 2007.

[5] Breasted, J.H, The Edwin Smith Surgical Papyrus, Chicago press: University of Chicago, 2 vols. (1: pp. xvi, 6, 480-485, 487-489, 446-448, 451-454, 466; 2: pi. XVII, XVIIA) , 1980.

[6] X. Huang, P. K. Jain, I. H. El-Sayed and M. A. El-Sayed, Plasmonic photothermal therapy (PPTT) using gold nanoparticles. *Lasers Med Sci 23(3),* pp. 217-228, 2008.

[7] S. Thomsen, Pathologic analysis of photothermal and photomechanical effects of laser-tissue interactions. *Photochem. Photobiol. 53(6),* pp. 825-835, 1991.

[8] A. C. Steger, W. R. Lees, K. Walmsley and S. G. Bown, Interstitial laser hyperthermia: A new approach to local destruction of tumours. *British Medical Journal- BMJ Publishing Group 299, No. 6695*pp. 362-365, 1989.

[9] L. R. Hirsch, R. J. Stafford, J. A. Bankson, S. R. Sershen, B. Rivera, R. E. Price, J. D. Hazle, N. J. Halas and J. L. West, " Nanoshell-mediated near-infrared thermal therapy of tumors under magnetic resonance guidance," *PNAS(Proceeding of the National Academy of Science of the United States of America),* vol. 100-23, pp. 13549-13554, 2003.

[10] Riadh W. Y. Habash, Rajeev Bansal, Daniel Krewski, Hafid T. Alhafid*,* vol. 35, pp. 1, 37,121, 2007.

[11] C. Chen, L. Kuo, C. Chang, Y. Hwu, C. Huang, S. Lee, K. Chen, S. Lin, J. Huang and Y. Chen, "In situ real-time investigation of cancer cell photothermolysis mediated by excited gold nanorod surface plasmons," *Biomaterials,* vol. 31, pp. 4104-4112, 2010.

[12] J. Shah, S. Park, S. Aglyamov, T. Larson, L. Ma, K. Sokolov, K. Johnston, T. Milner and S. Y. Emelianov, Photoacoustic imaging and temperature measurement for photothermal cancer therapy. *J. Biomed. Opt. 13(3),* pg. 034024, 2008.

[13] D. E. J. G. J. Dolmans, D. Fukumura and R. K. Jain, Photodynamic therapy for cancer. *Nat. Rev. Cancer 3(5),* pp. 380-387, 2003.

[14] P.K. Jain, K.S. Lee. I.H. El-Sayed, M.A. El-Sayed, Calculated absorption and scattering properties of gold nanoparticles of different size, shape, and composition: Applications in biological imaging and biomedicine *Journal Physics Chemistry B 110(14),* pp. 7238-7248, 2003.

[15] X. Huang, I. H. El-Sayed, W. Qian and M. A. El-Sayed, Cancer cell imaging and photothermal therapy in the near-infrared region by using gold nanorods. *J. Am. Chem. Soc. 128(6),* pp. 2115-2120, 2006.

[16] M. A. El-Sayed, Some interesting properties of metals confined in time and nanometer space of different shapes. *Account of Chemical Research, 34(4),* pp. 257-264, 2001.

[17] J. Shah, S. R. Aglyamov, K. Sokolov, T. E. Milner and S. Y. Emelianov, Ultrasound imaging to monitor photothermal therapy - feasibility study. *Opt. Express 16(6),* pp. 3776-3785, 2008.

[18] M. Pramanik, T. N. Erpelding, L. Jankovic and L. V. Wang,Tissue temperature monitoring using thermoacoustic and photoacoustic techniques, *The International Society for Optical Engineering.* SPIE, vol. 7564, 75641Y, 2010. Presented at Photons Plus Ultrasound: Imaging and Sensing 2010.

[19] R. A. Sultan, Tumour ablation by laser in general surgery. *Lasers Med Sci. 5(2),* pp. 185-193, 1990.

[20] Amira A. El-Adly, Waled M. El-Senousy, Farag A. Samhan 'Mona B. Mohamed, "Photothermal Efficieny of Gold Nanorods in Controlling Microorganisms in Water," Journal of Applied Sciences Research, 4(12),pp. 1811-1816, 2008.

[21] T. B. Huff, L. Tong, Y. Zhao, M. N. Hansen, J. Cheng and A. Wei, 2007, Hyperthermic effects of gold nanorods on tumor cells. *Nanomedicine 2(1),* pp. 125-132, 2008.

[22] Eghtedari Mohammad, Engineering functionalized gold nanoparticles and a molecular-specific contrast agent enhance optoacoustic detection of breast cancer cells, PHD Dissertation, The University of Texas Medical Branch, 2008.

[23] K. V. Larin, I. V. Larina and R. O. Esenaliev, Monitoring of tissue coagulation during thermotherapy using optoacoustic technique. *J. Phys. D 38(15),* pp. 2645-2653, 2005.

[24] R. O. Esenaliev, A. A. Karabutov and A. A. Oraevsky, Sensitivity of laser opto-acoustic imaging in detection of small deeply embedded tumors. *IEEE J Sel Top Quantum Electron 5(4),* pp. 981-988, 1999.

[25] A. A. Karabutov, E. V. Savateeva and A. A. Oraevsky, Optoacoustic tomography: New modality of laser diagnostic systems. *Laser Phys. 13(5),* pp. 711-723, 2003.

[26] L. V. Wang, Prospects of photoacoustic tomography. *Med. Phys. 35(12),* pp. 5758-5767, 2008.

[27] Jignesh Mukesh Shah, Ultrasound and photoacoustic imaging to guide and monitor photothermal therapy, PhD Dissertation, The University of Texas, Austin, 2008.

[28] Robert Joun Talbert, "Photoacoustic discrimination of vialbe and thermally coagulated Blood for burn injury imaging", MSc. Dissertation, The University of Missouri, Columbia, 2007.

[29] Ingle, J.D.J , Crouch,S.R., "Spectrochmical Analysis", Prentice Hall, New Jersey, 1988.

[30] J. T. Houghton, The Physics of Atmospheres. United Kingdom, Cambridge University Press. 3rd edition, 2002.

[31] Course Chemistry Social Relevance Projects, stage 2, The Univeristy of Adelaide, Australia, Beer Lambert Law, March 12, 2003. Available:http://www.chemistry.adelaide.edu.au/external/soc-rel/content/beerslaw.htm, Nov.09/2010

[32] Shiou-Han Wang, Chen-Wei Wei, Shiou-Hwa Jee and Pai-Chi Li,"Photoacoustic temperature measurements for monitoring of thermal therapy",*The International Society for Optical Engineering.* SPIE, vol. 7177, 2009.

[33] Jignesh Shah, Suhyun Park, Salavat Aglyamov, Timothy Larson, and Li Ma, Photoacoustic and Ultrasound imaging to guide photothermal therapy: ex vivo study, *The International Society for Optical Engineering.* SPIE, vol.6856, 2008.

[34] Jim Joy, *OperationS Manual IMAGIO Research Device - ALPHA.* San Antonio , TX: Seno Medical Instrument Inc., 2007.

[35] R. S. C. Cobbold, Foundations of Biomedical Ultrasound. Oxford; New York: Oxford University Press, first edition, 2007.

[36] G. Ku and L. V. Wang, Scanning microwave-induced thermoacoustic tomography: Signal, resolution, and contrast. *Med. Phys. 28(1),* pp. 4-10, 2001.

[37] M. C. Kolios, A. E. Worthington, D. W. Holdsworth, M. D. Sherar and J. W. Hunt, An investigation of the flow dependence of temperature gradients near large vessels during steady state and transient tissue heating. *Phys. Med. Biol. 44(6),* pp. 1479-1497, 1999.

[38] M. C. Kolios, A. E. Worthington, M. D. Sherar and J. W. Hunt, Experimental evaluation of two simple thermal models using transient temperature analysis *Phys. Med. Biol. 43(11),* pp. 3325-3340, 1998.

[39] K. V. Larin, I. V. Larina and R. O. Esenaliev, Real-time optoacoustic monitoring of temperature in tissues. *J. Phys. D: Appl. Phys 38(15),* pp. 2633-2639, 2005.

[40] M. A. Hayat, *Cancer Imaging.* Amsterdam; Boston: Elsevier, Academic Press, 2008.

[41] C. M. Niemeyer, Nanoparticles, proteins, and nucleic acids: Biotechnology meets materials science. Angewandte Chemie - International Edition *40(22),* pp. 4129-4158, 2001.

[42] J. L. West and N. J. Halas, Engineered nanomaterials for biophotonics applications: Improving sensing, imaging, and therapeutics, Annual Review of Biomedical Engineering, vol. 5 pp. 285-292, 2003.

[43] X. Li, L. Chen, F. S. Wan, L. L. Li, B. Jiang, Analysis of collagenous structures for cartilage tissue engineered scaffolds, *Journal of Clinical Rehabilitative Tissue Engineering Research* 14(3), pp. 385-388, 2010.

[44] D.M.Murphy, The Effect of Water Evaporation on Photoacoustic Signals in Transition and Molecular Flow, *Aerosol Science and Technology*, 43, pp. 356–363, 2009.